

TECHNICAL REPORT 94-18

Grimsel Test Site

Modelling Radionuclide Migration Field Experiments

September 1996

W. Heer
J. Hadermann

PSI, Würenlingen and Villigen

TECHNICAL REPORT 94-18

Grimsel Test Site

Modelling Radionuclide Migration Field Experiments

September 1996

W. Heer
J. Hadermann

PSI, Würenlingen and Villigen

This report was prepared on behalf of Nagra. The viewpoints presented and conclusions reached are those of the author(s) and do not necessarily represent those of Nagra.

"Copyright © 1996 by Nagra, Wettingen (Switzerland) / All rights reserved.

All parts of this work are protected by copyright. Any utilisation outwith the remit of the copyright law is unlawful and liable to prosecution. This applies in particular to translations, storage and processing in electronic systems and programs, microfilms, reproductions, etc. "

Grimsel Test Site - Modelling Radionuclide Migration Field Experiments

W. Heer and J. Hadermann

Paul Scherrer Institute, CH-5232 Villigen/PSI, Switzerland

September 1994

Short Summary: The Grimsel radionuclide migration experiment is a multidisciplinary study aimed at investigating solute transport in fractured media. Extensive field work is complemented by a substantial programme of hydrodynamic, chemical and transport modelling, along with supporting laboratory studies. In the present report the basis and application of the transport model developed at the Paul Scherrer Institute are described. It was possible to calibrate the relatively simple, homogeneous dual-porosity advection/diffusion model from non-sorbing anion tracer breakthrough curves. The model-derived parameters are physically reasonable. Consistent modelling of a set of tests under identical flow conditions and with different cation-exchange tracers (^{22}Na , ^{85}Sr) was possible. Fitted sorption coefficients were close to the ones measured in the laboratory for coarse fracture material. The applicability of the model was further demonstrated by rather accurately predicting various tracer experiments in different flow fields.

Key Words: Grimsel Test Site, Underground Laboratory, Groundwater Transport, Fracture Flow, Tracer Experiments, Dipole Flow Fields, Advection/Diffusion Model, Matrix Diffusion, Sorption, Cation Exchange, Predictive Modeling, Model Validation.

Inhaltsangabe: Der Migrationsversuch im Felslabor Grimsel ist ein multidisziplinäres Vorhaben zur Untersuchung des Stofftransportes im Grundwasser eines geklüftetem Gesteins. Die vielen Feldexperimente werden durch Modellierarbeiten (hydrodynamisch, chemisch, Transport) ergänzt und durch ein Laborprogramm unterstützt. Im vorliegenden Bericht werden Grundlagen und Anwendung eines Transportmodells, das am Paul Scherrer Institut entwickelt wurde, vorgestellt. Es war möglich, das relativ einfache, homogene Advektion-Diffusionsmodell (doppelt-poröses Medium) aufgrund von Durchbruchkurven nicht-sorbierender Anionen zu kalibrieren. Die abgeleiteten Parameter sind physikalisch sinnvoll. Experimente in gleichen Fließfeldern, aber mit sorbierenden Kationen (^{22}Na , ^{85}Sr) waren mit dem Modell konsistent; die abgeleiteten Sorptionskoeffizienten waren vergleichbar mit Werten, die im Labor für grobe Fraktionen von Kluftmaterial bestimmt wurden. Die Gültigkeit des Modells wurde zusätzlich bestätigt durch relativ genaue Voraussagen ähnlicher Experimente in verschiedenen Strömungsfeldern.

Stichworte: Felslabor Grimsel, Grundwassertransport, geklüftetes Gestein, Tracerversuche, Dipol-Fließfelder, Advektion-Diffusions Modell, Matrixdiffusion, Sorption, Kationenaustausch, Modellprognosen, Validierung.

Récapitulation: L'expérience de migration de radionucléides au Grimsel est une recherche multidisciplinaire destinée à l'étude du transport de matière par écoulement souterrain en milieu fracturé. Un important programme de terrain a été complété par des travaux de modélisation hydrodynamique, chimique et du transport, et par des essais en laboratoire. Le présent rapport décrit les bases et les applications du modèle de transport développé à l'Institut Paul Scherrer. On a pu calibrer le modèle relativement simple de convection/diffusion pour un système à double porosité à partir des courbes de restitution de traceurs anioniques non adsorbants. Les valeurs des paramètres dérivés du modèle sont considérés comme physiquement raisonnables. La modélisation des essais effectués sous des conditions d'écoulement identiques, mais avec des cations adsorbants (^{22}Na , ^{85}Sr) donne des résultats cohérents. Les coefficients d'adsorption ajustés sont proches de ceux mesurés en laboratoire sur des échantillons à grains grossiers du remplissage de fissure. L'adéquation du modèle a de plus été démontrée par la prédiction assez précise des résultats d'essais de traçage sous des conditions d'écoulement variées.

Mots-clé: Laboratoire du Grimsel, transport, écoulement souterrain, milieu fracturé, traceurs, dipôle, modèle de convection/diffusion, diffusion matricielle, adsorption, échange cationique, prévision, validation.

FOREWORD

Concepts for the disposal of radioactive waste in geological formations place a significant emphasis on acquiring extensive knowledge of the proposed host rock and the surrounding strata. For this reason, Nagra has, since May 1984, been operating the Grimsel Test Site (GTS) which is located at a depth of 450 m in the crystalline rock of the Aare Massif of the Central Swiss Alps. The general objectives of the research being carried out in this underground laboratory include

- the build-up of know-how in planning, performing and interpreting field experiments in various scientific and technical disciplines and
- the acquisition of practical experience in the development of investigation methodologies, measuring techniques and test equipment that will be of use during actual repository site explorations.

On the basis of a collaborative agreement various experimental activities started 1984 by Nagra and two German partners, the Federal Institute for Geoscience and Natural Resources (BGR) and the Research Center for Environmental Sciences (GSF). During the successive phases of the research and development programme other organisations and countries have joined the Grimsel projects. International cooperation was continuously extended with ANDRA (France), ENRESA (Spain), US-DOE (United States), SKB (Sweden) and PNC (Japan).

The Radionuclide Migration Experiment (MI) is currently Nagra's most significant contribution to the Grimsel program. MI is a multidisciplinary study aimed at investigating solute transport in fractured media. Extensive field work is complemented by a substantial program of hydrodynamic, chemical and transport modeling, along with supporting laboratory studies. This project, initiated in 1985 and currently planned to be terminated in 1996, was initially conceived as a collaborative project between Nagra and the Paul Scherrer Institute (PSI). Since 1987, expertise and equipment for on-site radiotracer analyses have been provided by the Institute of Hydrology of the GSF Munich-Neuherberg. In 1989 a bilateral collaboration agreement was signed with the Japanese Power Reactor and Nuclear Fuel Development Corporation (PNC) and the support provided via this cooperation resulted in a substantial extension of the project.

An overview of the investigations within the Radionuclide Migration Experiment from 1985 to 1990 is documented in the Nagra Technical Report NTB 91-04. In the present report the basis and application of the transport model developed at the PSI are described, while experimental details of the relevant tracer tests are provided in Nagra Technical Report NTB 94-17 (also PSI Report 94-11).

The Waste Management Laboratory at the Paul Scherrer Institute (PSI) is performing work to develop and test models as well as to acquire specific data relevant to performance assessments of Swiss nuclear waste repositories. These investigations are undertaken in close co-operation with, and with the partial financial support of, the national Cooperative for the Disposal of Radioactive Waste (Nagra). The present report, issued simultaneously as a Nagra Technical Report and PSI Report 94-13, was produced within the framework of the cooperation agreements mentioned above. The authors have presented their own opinions and conclusions which do not necessarily coincide with those of Nagra or its participating partners.

VORWORT

Bei Konzepten, welche die Endlagerung radioaktiver Abfälle in geologischen Formationen vorsehen, ist die Kenntnis des Wirtgesteins und der angrenzenden Gesteinsschichten von grundlegender Bedeutung. Die Nagra betreibt deshalb seit Mai 1984 das Felslabor Grimsel (FLG) in 450 m Tiefe im Kristallin des Aarmassivs. Die generelle Zielsetzung für die Arbeiten in diesem System von Versuchsstollen umfasst

- den Aufbau von Know-how in der Planung, Ausführung und Interpretation von Untergrundversuchen in verschiedenen wissenschaftlichen und technischen Fachgebieten, und
- den Erwerb praktischer Erfahrung in der Entwicklung und der Anwendung von Untersuchungsmethoden, Messverfahren und Messgeräten, die für die Erkundung von potentiellen Endlagerstandorten in Frage kommen.

Auf der Basis eines deutsch-schweizerischen Zusammenarbeitsvertrages begannen 1984 verschiedene Versuche der Nagra und der beiden deutschen Partnern, Bundesanstalt für Geowissenschaften und Rohstoffe, Hannover (BGR) und Forschungszentrum für Umwelt und Gesundheit GmbH, München (GSF). Die internationale Zusammenarbeit wurde im Verlauf der Jahre ausgeweitet mit den folgenden Partnerorganisationen ANDRA (Frankreich), ENRESA (Spanien), US-DOE (Vereinigte Staaten), SKB (Schweden) and PNC (Japan).

Der Migrationsversuch (MI) ist ein sehr wesentlicher Beitrag zum Grimsel Programm. MI ist ein multidisziplinäres Experiment zur Untersuchung des Transportverhaltens von Radionukliden im Grundwasser eines geklüftetem Gesteins. Die ausgedehnten Feldversuche werden unterstützt durch ein umfangreiches Programm zur hydrodynamischen und chemischen Charakterisierung des MI-Bereichs und zur Modellierung der Transportprozesse sowie durch ergänzende Laboruntersuchungen. Das 1985 begonnene und, gemäss jetziger Planung, bis 1996 dauernde Versuch MI war ursprünglich als gemeinsames Vorhaben der Nagra und des Paul Scherrer Instituts (PSI) konzipiert worden. Seit 1987 stellt das Institut für Hydrologie der GSF, München-Neuherberg für die Radiotracer-Analysen bei Feldversuchen ihr Fachwissen und eine geeignete Ausrüstung zur Verfügung. Im Jahre 1989 unterzeichnete dann Nagra mit der japanischen Power Reactor and Nuclear Fuel Corporation (PNC) einen Vertrag zur Beteiligung der PNC am Migrationsversuch, wodurch eine wesentliche Erweiterung des Untersuchungsprogrammes ermöglicht wurde.

Ein Überblick über die Untersuchungen von 1985 bis 1990 im Rahmen des Migrationsversuchs ist im Nagra Technischen Bericht NTB 91-04 dokumentiert. Der vorliegende Bericht beschreibt umfassend die Transportmodellierung des PSI; die spezifischen experimentellen Aspekte der dazugehörigen Tracerversuche sind in NTB 94-17 oder PSI Bericht 94-11 beschrieben.

Das Labor für Entsorgung am Paul Scherrer Institut (PSI) führt Arbeiten zu Sicherheitsanalysen für schweizerische nukleare Endlager durch. Sie umfassen sowohl die Entwicklung und das Testen von Modellen als auch das Gewinnen spezifischer Daten. Diese Untersuchungen werden in enger Zusammenarbeit und mit teilweiser finanzieller Unterstützung der Nationalen Genossenschaft für die Lagerung radioaktiver Abfälle (Nagra) vorgenommen. Der vorliegende Bericht erscheint gleichzeitig als Nagra NTB und als PSI Bericht Nr. 94-13 und wurde im Rahmen der erwähnten Zusammenarbeitsverträge erstellt. Die Autoren haben ihre eigenen Ansichten und Schlussfolgerungen dargelegt. Diese müssen nicht unbedingt mit denjenigen der Nagra oder der beteiligten Partner übereinstimmen.

AVANT - PROPOS

Lors d'études de concepts de stockage de déchets radioactifs dans des formations géologiques, on attache une grande importance à l'acquisition d'informations étendues sur la roche d'accueil et les formations rocheuses environnantes. C'est pour cette raison que la Cédra exploite depuis mai 1984 son laboratoire souterrain du Grimsel (LSG) situé à 450 m de profondeur dans le cristallin du massif de l'Aar, au coeur des Alpes centrales. Les principaux objectifs des recherches effectuées dans ce réseau de galeries comprennent:

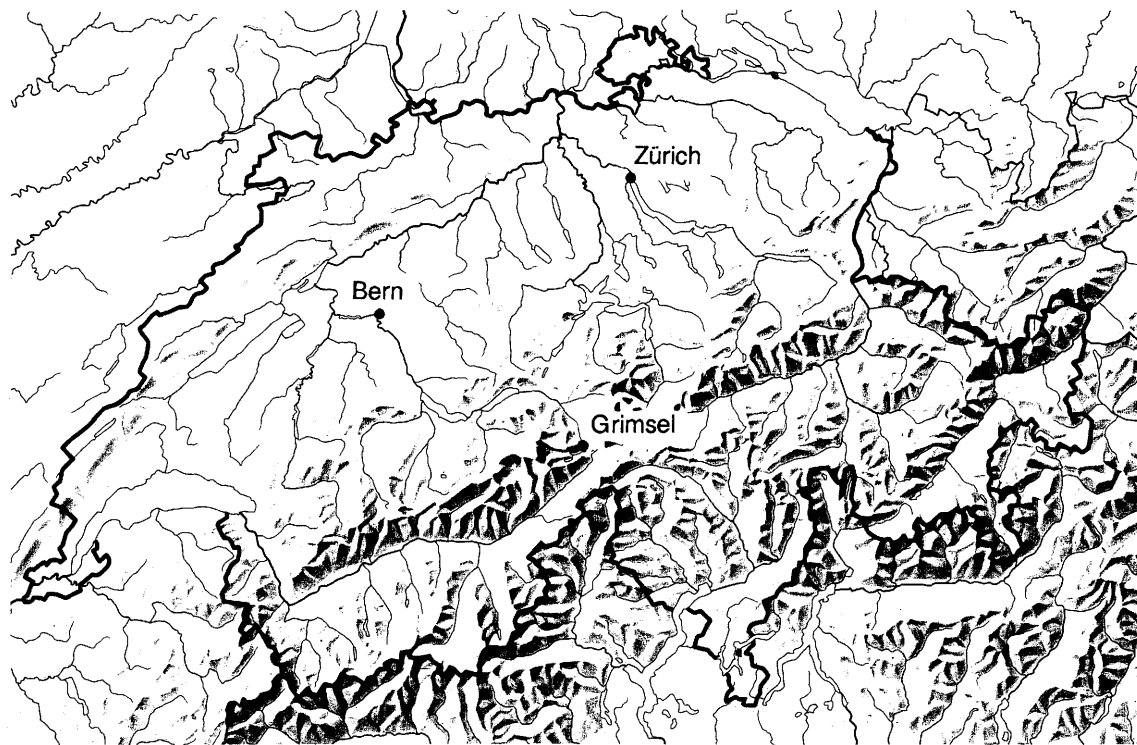
- l'acquisition de savoir-faire dans diverses disciplines techniques et scientifiques en ce qui concerne la conception, la réalisation et l'interprétation d'expériences in situ, ainsi que
- l'accumulation d'expériences pratiques dans la mise au point et l'application de méthodes d'investigation, de techniques et d'appareillages de mesure, qui pourraient être utilisés lors de l'exploration de sites potentiels de dépôts finals.

Le LSG est exploité par la Cédra et diverses expériences y sont réalisées à partir de 1984 par celle-ci et deux institutions allemandes, la "Bundesanstalt für Geowissenschaften und Rohstoffe, Hanovre" (BGR) et le "Forschungszentrum für Umwelt und Gesundheit GmbH, Munich" (GSF), dans le cadre d'un traité de collaboration germano-suisse. La coopération internationale s'est accrue au fil des années, avec des partenaires de l'Espagne (ENRESA), des USA (DOE), du Japon (PNC), de la Suède (SKB) et de la France (Andra)..

L'expérience de migration de radionucléides (MI) représente la contribution essentielle de la Cédra au programme du Grimsel. MI est une étude multidisciplinaire ayant pour objectif l'étude du transport en solution en milieu fissuré. Les travaux de terrain intensifs sont complétés par un programme de modélisation hydrodynamique, chimique et de transport, ainsi que par des essais en laboratoire. Ce projet, qui a débuté en 1985 et devrait se terminer en 1996, fut initialement conçu comme une collaboration entre la Cédra et l'Institut Paul Scherrer (IPS). Depuis 1987, des essais de terrain avec des traceurs radioactifs ont été réalisés par l'institut d'hydrologie de la GSF de Munich-Neuherberg. En 1989, un accord bilatéral de collaboration a été signé avec la "Power Reactor and Nuclear Fuel Development Corporation" (PNC) du Japon; il a conduit à une extension substantielle du programme d'investigation.

Un aperçu des recherches effectuées de 1985 à 1990 dans le cadre des essais de migration a été présenté dans le rapport technique Cédra NTB 91-04. Dans le présent rapport, on présente en détail le modèle de transport développé à l'IPS, tandis que les aspects expérimentaux des essais de traçage sont présentés dans le rapport technique NTB 94-17 (également rapport IPS 94-11).

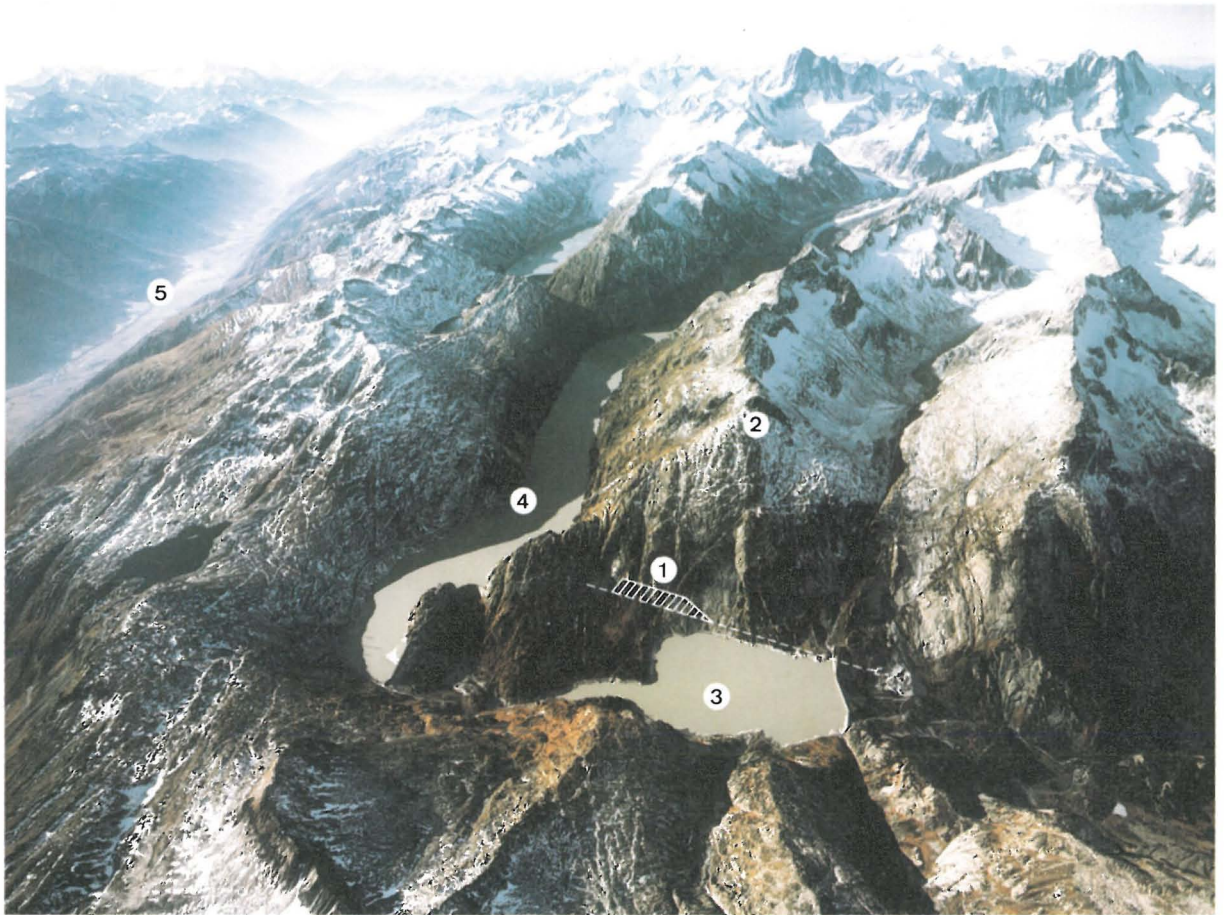
Le laboratoire de l'Institut Paul Scherrer (IPS) se consacre au développement et au test de modèles ainsi qu'à l'acquisition de données pour les analyses de sûreté des dépôts de déchets radioactifs en Suisse. Ces activités sont entreprises en étroite collaboration avec la Société coopérative nationale pour l'entreposage de déchets radioactifs (Cédra), et avec sa participation financière. Le présent rapport, publié simultanément en tant que rapport technique de la Cédra (NTB) et rapport IPS No 94-13, a été élaboré dans le cadre des accords de collaboration mentionnés. Les auteurs ont présenté leurs vues et conclusions personnelles. Celles-ci ne correspondent pas forcément à celles de la Cédra ou à celles de ses partenaires.



Reproduziert mit Bewilligung des Bundesamtes für Landestopographie vom 19.6.1991

Location of Nagra's underground test facility at the Grimsel Pass in the Central Alps (Bernese Alps) of Switzerland (approximate scale 1 cm = 25 km).

Geographische Lage des Nagra Felslabors am Grimselpass (Berner Oberland) in den schweizerischen Zentralalpen (Massstab: 1 cm = ca. 25 km)



GRIMSEL-GEBIET

Blick nach Westen

- 1 Felslabor
- 2 Juchlistock
- 3 Räterichsbodensee
- 4 Grimselsee
- 5 Rhonetal

GRIMSEL AREA

View looking West

- 1 Test Site
- 2 Juchlistock
- 3 Lake Raeterichsboden
- 4 Lake Grimsel
- 5 Rhone Valley

FLG FELSLABOR GRIMSEL
GTS GRIMSEL TEST SITE

Situation



- Zugangsstollen/ Access tunnel
- Fräsvortrieb/ by tunnel boring machine
- Sprengvortrieb/ excavated by blasting
- Zentraler Aaregranit ZAGR
Central Aaregranite CAGR
- Biotitreicher ZAGR
CAGR with high content of biotite
- Grimsel-Granodiorit
Grimsel-Granodiorite
- Scherzone/ Shear zone
- Lamprophyr/ Lamprophyre
- Wasserzutritt/ Water inflow
- Sondierbohrung/ Exploratory borehole
- US Bohrung/ US borehole
- ZB Zentraler Bereich/ Central facilities
- AU Auflockerung/ Excavation effects
- BK Bohrlochkranz/ Fracture system flow
- EM El.magn. HF-Messungen/ -measurements
- FRI Klutzzone/ Fracture zone investigation
- GS Gebirgsspannungen/ Rock stresses
- HPA Hydr. Parameter/ Hydr. parameters
- MI Migration/ Migration
- MOD Hydrodyn. Modellierung/ H. modeling
- NM Neigungsmesser/ Tiltmeters
- UR Untertageradar/ Underground radar
- US Seismik/ Underground seismic testing
- VE Ventilationstest/ Ventilation test
- WT Wärmeversuch/ Heat test

A — A Schnitt/ Section

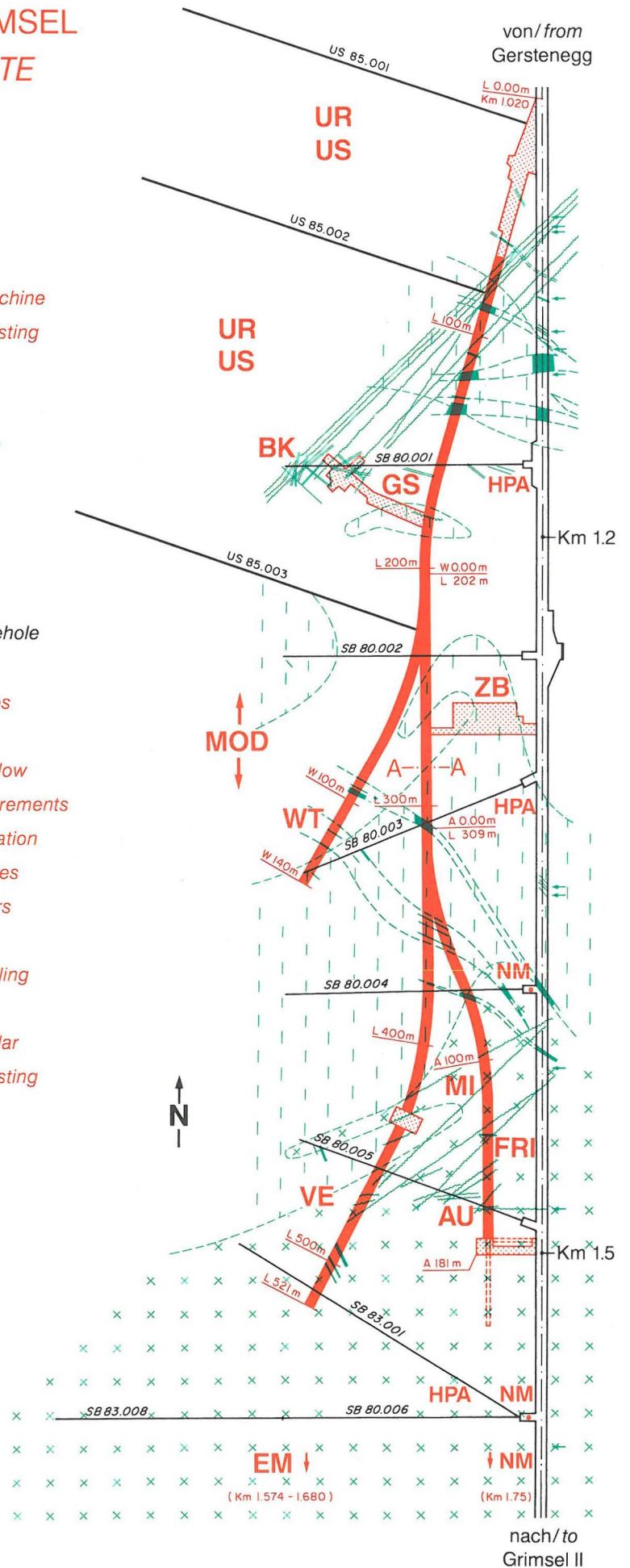
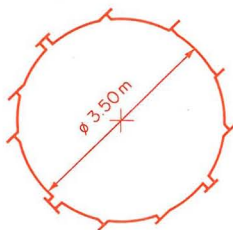


Table of Contents

Short Abstract and Key Words.....	i
Foreword.....	iii
Vorwort.....	iv
Avant-Propos.....	v
Abstract.....	ix
Zusammenfassung.....	x
Résumé.....	xi
1 INTRODUCTION.....	13
2 MAIN FEATURES OF THE EXPERIMENTS.....	14
3 THEORETICAL MODEL.....	16
3.1 Hydrology.....	16
3.1.1 Tracer Nuclide Transport.....	34
3.1.2 Basic Procedure.....	34
3.1.3 Transport Equations.....	38
3.1.4 Effective Surface Sorption Approximation.....	47
3.1.5 Infill of the water Conducting Zone.....	48
3.1.6 Influence of Matrix Diffusion.....	49
4 ANALYSIS OF EXPERIMENTAL BREAKTHROUGH CURVES.....	58
4.1 Experimental Conditions and Fixed Parameters.....	58
4.2 Calibration with the Conservative Tracer Uranine.....	60
4.2.1 Selection of Fit Parameters.....	60
4.2.2 Results.....	62
4.2.3 Parameter variations.....	66
4.2.4 Influence of the Injection Distribution.....	73
4.3 Sorbing Tracers.....	76
4.3.1 Selection of Fit Parameters.....	76
4.3.2 Results and parameter variations for Sodium.....	78
4.3.3 Results and parameter variations for Strontium.....	83
4.3.4 Comparison of Sorption Coefficients.....	92
4.4 Summary of Physical Parameters.....	97
5 PREDICTIONS OF BREAKTHROUGH CURVES FOR A SMALLER DIPOLE FLOW FIELD.....	99
6 CONCLUSIONS.....	104
7 ACKNOWLEDGMENTS.....	107
8 APPENDICES.....	108
9 REFERENCES.....	135

8	APPENDICES	108
	Appendix 1: The Width of the Breakthrough Curve taking into Account Advection and Matrix Diffusion only.....	108
	Appendix 2: Influence of Dispersion	109
	Appendix 3: Comments to the Parameters of the Porous Rock Zone.....	114
	Appendix 4: Error Estimate of the Physical Parameters derived from the Fit.....	117
	Appendix 5: Parameters of the Migration Zone as Deduced from Geological Investigations.....	122
	Appendix 6: Extrapolation of laboratory Results to the Conditions of the Migration Field Experiments.....	126
	Appendix 7: Selected Dipole Positions and Flow Fields for Tracer Experiments.....	129
	Appendix 8: Influence of the Dipole Flow Field Geometry to the Breakthrough Curve.....	130
9	REFERENCES	135

Abstract

In the migration field experiments at Nagra's Grimsel Test Site, the processes of nuclide transport through a well defined fractured shear-zone in crystalline rock are being investigated. For these experiments, model calculations have been performed to obtain indications on validity and limitations of the model applied and the data deduced under field conditions.

The **model** consists of a hydrological part, where the dipole flow fields of the experiments are determined, and a nuclide transport part, where the flow field driven nuclide propagation through the shear-zone is calculated. In addition to the description of the model, analytical expressions are given to guide the interpretation of experimental results.

From the **analysis** of experimental breakthrough curves for conservative uranine, weakly sorbing sodium and more strongly sorbing strontium tracers, the following main results can be derived:

- i) The model is able to represent the breakthrough curves of the migration field experiments to a high degree of accuracy. (A simple dual-porosity concept is used describing advective-dispersive transport in narrow water conducting zones and molecular diffusion into stagnant water of the adjacent porous rock zones – matrix diffusion).
- ii) The process of matrix diffusion is manifest through the special shape of the tail ends as well as through the tails of the breakthrough curves, with tracer concentrations decreasing with time as a function of $t^{-3/2}$, both features are confirmed by the experiments.
- iii) For nuclides which sorb rapidly, not too strongly and linearly, and which exhibit a reversible cation exchange process on fault gouge, the laboratory sorption coefficients can be reasonably well extrapolated to field conditions. Adequate care in selecting and preparing the rock samples is, of course, a necessary requirement.

Using the parameters determined in the previous analysis, predictions are made for experiments in a smaller and faster flow field. The agreement between predicted and measured breakthrough curves is good for the conservative uranine as well as for the weakly sorbing sodium, and still reasonable for the more strongly sorbing strontium – confirming that the model adequately describes the main nuclide transport processes.

The Grimsel radionuclide migration field experiments, performed with an exceptionally high precision, are a useful test of model and data. The modelling results represent an important step in improving the understanding of nuclide transport mechanisms and contribute to increasing confidence in the transport calculations within the framework of safety assessments.

Zusammenfassung

Das Migrationsexperiment im Felslabor Grimsel der Nagra hat zum Ziel, die Transportmechanismen von Nukliden in einer wohldefinierten Kluftzone in Kristallingestein zu untersuchen. Dabei sollen speziell Anwendbarkeit und Grenzen von Modell und Daten aufgezeigt werden.

Das **Modell** besteht einerseits aus einem Hydrologieteil, welcher die Dipol-Wasserströmung in den Experimenten beschreibt, und andererseits einem Nuklidtransportteil, welcher die Migration in diesem Wasserfliessfeld durch die Kluftzone darstellt. Als hilfreich zur Interpretation der experimentellen Resultate haben sich, neben der detaillierten Berechnung mit dem Code RANCHMDNL, auch analytische Abschätzungen erwiesen.

Die hauptsächlichlichen Resultate der **Analysen** von Experimenten mit Uranin, Natrium und Strontium lassen sich wie folgt zusammenfassen:

- i) Das Modell beschreibt die Durchbruchkurven der Migrationsexperimente mit hoher Zuverlässigkeit. (Es verwendet ein doppelt-poröses Konzept, welches advektiv-dispersiven Transport in engen wasserführenden Zonen ("Öffnungen") und Matrixdiffusion in die angrenzenden, stagnierendes Wasser enthaltenden, porösen Gesteinszonen darstellt).
- ii) Der Prozess der Matrixdiffusion verursacht typische Durchbruchkurven: einerseits ist die Tracerkonzentrationen im abfallenden Ast eine Funktion der Zeit ($t^{-3/2}$ -Gesetz) und andererseits – bei grosse Zeiten – ergibt sich eine charakteristische Form für das Ende der Durchbruchkurven. Beide Eigenschaften werden durch die Experimente bestätigt.
- iii) Für Nuklide, die schnell, nicht zu stark, linear und gemäss einem reversiblen Kationenaustauschprozess an der Kluftfüllung (Fault Gouge) sorbieren, können die im Labor bestimmten Sorptionskoeffizienten recht gut auf Feldbedingungen extrapoliert werden. Voraussetzung dafür ist eine angemessene Sorgfalt bei der Auswahl und Aufbereitung der Gesteinsproben.

Mit festgehaltenen Parametern aus dieser Analyse werden **Vorhersagen** für Experimente in einem kleineren und schnelleren Dipol-Wasserfliessfeld gemacht. Für den konservativen Tracer Uranin (Anion) und den schwach sorbierenden Tracer Natrium ist die Übereinstimmung zwischen Vorhersage und anschliessender Messung der Durchbruchkurven gut. Für den starker sorbierenden Tracer Strontium ist die Übereinstimmung befriedigend. Dies bestätigt weiter, dass das Modell die wesentlichen Transportmechanismen angemessen beschreibt.

Die Migrationsfeldexperimente im Felslabor Grimsel, die mit einer aussergewöhnlich hohen Präzision durchgeführt wurden, stellen einen nützlichen Test für Modelle und Daten dar. Die Resultate der Modellierung bilden einen wichtigen Schritt zur Erhöhung des Verständnisses von Transportmechanismen und tragen dazu bei, das Vertrauen in Nuklidtransportrechnungen im Rahmen von Sicherheitsanalysen zu verstärken.

Résumé

Les expériences de migration au laboratoire souterrain du Grimsel de la Cédra ont pour but d'étudier les mécanismes de transport en solution dans une fissure bien définie dans la roche cristalline. Dans le cadre de ces expériences, des calculs ont été réalisés en vue de tester la validité et les limites du modèle appliqué et des données pour les conditions du terrain.

Le modèle comporte une partie hydrologique, qui décrit les champs d'écoulement des dipôles expérimentaux, et une partie concernant le transport en solution, qui décrit la migration des nucléides dans la fissure. En outre, les expressions analytiques servant de guide à l'interprétation des résultats expérimentaux sont données.

Les principaux résultats de l'analyse des courbes d'écoulement pour l'uranine, traceur non sorbant, le sodium, traceur faiblement sorbant, et le strontium, traceur plus fortement sorbant, sont les suivants:

- i) Le modèle peut reproduire les courbes d'écoulement des expériences de migration avec une bonne précision. (Un concept de double porosité est utilisé, pour décrire le transport advectif et dispersif dans des zones conductrices et diffusion moléculaire dans l'eau stagnante des pores de la zone adjacente - diffusion dans la matrice).
- ii) Le processus de diffusion dans la matrice est mis en évidence par les queues des courbes d'écoulement, qui décroissent en fonction de $t^{-2/3}$ et par la forme spécifique des fins de queue. Ces deux effets sont confirmés par les expériences.
- iii) Pour des nucléides qui sorbent rapidement, pas trop fortement, de façon linéaire et qui exhibent un échange réversible des cations sur une brèche de remplissage, les coefficients de sorption obtenus au laboratoire peuvent raisonnablement être extrapolés aux conditions du terrain; une exigence nécessaire est un soin adéquat pour sélectionner et préparer les échantillons de roche.

En utilisant les paramètres de l'analyse précédente, des prédictions ont été faites pour les expériences dans un champ d'écoulement plus petit et plus rapide. Pour l'uranine, traceur non sorbant, et le sodium, traceur faiblement sorbant, la comparaison entre les courbes d'écoulement expérimentales et celles prédites est bonne. Pour le strontium, la comparaison est raisonnable. L'accord observé confirme que le modèle décrit de façon adéquate les principaux processus de transport des nucléides.

Les expériences de migration au Grimsel, réalisées avec précision exceptionnelle, constituent un test très précieux pour le modèle et les données. Les résultats du modèle représentent une étape importante quant à la compréhension des mécanismes de transport des nucléides et contribue à accroître la confiance dans les calculs de transport pour des analyses de sécurité.

1 Introduction

The safety of radioactive waste repositories in geological formations relies, among other factors, on the barrier function of the host rock. Therefore, models of radionuclide transport are important components of a safety assessment. In Switzerland, as elsewhere (e.g. Refs. [1] and [2]) testing of such models is a crucial and long-lasting activity. To this end, and in order to develop methods for site characterisation, an integrated migration experiment has been carried out at Nagra's Grimsel Test Site. Large effort and time has been taken to achieve high-quality field tracer measurements (cf. Ref. [3]).

The objectives of modelling the migration field experiments are:

- i) An improved understanding of nuclide transport.
- ii) A test of model and deduced transport parameters under field conditions.
- iii) Finally - improving the confidence in safety assessment models.

This report describes the modelling work performed at PSI in the framework of the migration experiment. It is envisaged to give a consistent summary of the model, to apply it to the analysis of selected experiments and to use it also for predictions of new measurements. The intention is to present a reference report containing enough details and comments that traceability of basic ideas and numerical values is ensured. Chapter 2 provides the necessary experimental information to understand the basic ideas of the model. Chapter 3 describes the theoretical model, first for the hydraulics of the dipole field and then for tracer transport. In addition, analytical expressions are given to guide the interpretation of experimental results. In chapter 4, the model is applied to the analysis of selected tracer migration experiments. The methodology is to calibrate tracer independent data with a conservative tracer and then, keeping those parameters fixed, to investigate transport of sorbing tracers. A comparison to sorption data from other than the migration field experiments is also carried out. In chapter 5 predictions are made for a new dipole arrangement and compared to subsequent experiments. In chapter 6 conclusions are drawn. The appendices give some detailed information on selected topics not elaborated in the main text.

2 Main Features of the Experiments

To provide the experimental information necessary to understand the basic ideas of the model, the main features of the migration experiments at GTS are briefly summarized. A detailed description of the site and the experimental set-up is given in Ref. [3]. Specific experimental details and results are presented in Ref. [4].

The experiments are performed in a fractured water conducting shear-zone of crystalline rock (the migration shear-zone). Several boreholes were drilled from the GTS laboratory drift into the migration shear-zone and the intersections packed off. After extensive hydraulic tests (cf. Ref. [3], chapter 4) suitable bore hole pairs were selected. Water is injected at one bore hole and extracted from the second at a higher rate generating a steady state unequal dipole flow field. Two different dipoles are considered in this report, corresponding to an injection-extraction point distance of 4.9 m and 1.7 m respectively (cf. App. 7). To investigate nuclide transport, tracer pulses with different properties are added to the injected water. Uncertainties due to unknown tracer perturbations within the equipment are avoided by minimizing packer interval volumes and measuring tracer concentrations down hole at the injection point of the fracture by quartz fiber fluorometry (cf. Ref. [3], section 6-5) ¹. Natural Grimsel water from the migration shear-zone² is used for injection so that tracer behaviour is not influenced by a possibly disturbed water chemistry. Typical water injection and extraction rates are 9 ml/min and 150 ml/min, respectively, leading to full tracer recovery, avoiding double peak breakthrough curves, minimizing perturbations by the natural water flow, and at the same time avoiding, as much as possible, changes to the migration shear-zone. The tracers analysed in this report are non-sorbing uranine (sodium salt of fluorescein), weakly sorbing sodium (^{22,24}Na) and more strongly sorbing strontium (⁸⁵Sr). Tracer breakthrough concentrations corresponding to the extraction point from the shear-zone are measured (the fluorotracer uranine down hole by quartz fiber fluorometry and the radiotracers at the GTS laboratory drift by γ -detection with a sodium iodide scintillation counter). The radiotracer concentrations are corrected for radioactive decay as well for the delay in tubing and equipment³.

The results of the experiments are carefully and reliably measured breakthrough curves, implicitly containing the informations on nuclide transport averaged over the relevant part

¹It was verified in various equipment tests, that the injection distribution determined for the fluorotracer also holds for radiotracers injected simultaneously.

²Taken from a location outside the dipole flow field and stored under cover gas atmosphere.

³The effect is small due to the high extraction velocity. The corresponding delay of the radiotracers (7 minutes) are therefore corrected only for the 1.7 m dipole experiments, exhibiting fast breakthroughs.

of the shear-zone. The model has to deduce from the experimental data explicitly nuclide transport parameters and to make breakthrough predictions.

3 Theoretical Model

In this section the concept of the model describing tracer transport in the migration field experiments is presented and discussed. The model consists of a hydrological part where the flow field is calculated and a transport part where, based on a known flow field, tracer transport through a fractured migration zone is calculated.

The details of the model, emphasizing especially the hydrological part, are described in Ref. [5]. The nuclide transport part is based on Ref. [6]. General background information on transport modelling can be found e.g. in Refs. [7], [8] and [9].

It should be emphasized right at the beginning that the model uses and allows for extraction of space averaged parameters. For dipole experiments, when measuring breakthrough curves, this averaging is done in a natural way: The experiments *eo ipso* average over the region of the dipole field.

3.1 Hydrology

The description of the hydrology relevant for the migration experiment relies on the following basic **hypotheses**:

1. The migration zone⁴ is defined as that part of the migration shear-zone⁵ (cf. Ref. [10], p. 9) which determines tracer transport in the migration experiments. On this restricted scale of several meters it can be simplified to a planar confined aquifer of constant width⁶. The validity of this assumption is corroborated by geological investigations (cf. Ref. [3], sections 2.1, 3.1.2 and 3.2 as well as Refs. [10] and [11]).
2. The flow in the aquifer obeys Darcy's law (equation of viscous fluid motion averaged over a representative elementary volume and neglecting drag forces, - conservation of momentum).
3. The fluid (water) compressibility can be neglected.

⁴"Migration zone" is used throughout this report as a modelling term.

⁵The term "migration shear-zone" is identical with "migration fracture (AU 96 m)" in Ref. ([3], p. 3-1).

⁶The term "width", often referred to as "thickness", is used here to be consistent with the notation in Ref. ([5], p. 27).

4. The temperature is constant (no consideration on conservation of energy).
5. The migration zone can be characterised by an average (time-independent) homogeneous isotropic transmissivity T and by an average (time-independent) homogeneous flow porosity ϵ . The first assumption is based on an evaluation of hydraulic single-borehole and interference tests. Although the evaluation of single-borehole hydraulic testing yielded a certain variability of T , any cross-hole hydraulic tests between the different borehole intervals indicated the same average T of about $2 \cdot 10^{-6} \text{ m}^2/\text{s}$ (cf. Ref. [3], section 4.1 ; the average value of T on p. 4-5, bottom).
6. The flow field can be approximated by an unperturbed dipole field governed by position and pumping rate of the injection and the extraction well (cf. Ref. [3], p. 6-5). To minimize perturbation by the natural flow field, the dipoles are positioned in a region of flat hydraulic potentials for closed wells (cf. Ref. [12], p. 16, Tab. 4, and p. 19, Fig. 9a, well 4/6 and 9/6). In addition the extraction rate is relatively high and the investigated flow fields narrow (cf. Fig. 4, ($\beta \approx 15$)).
7. The dipole flow field is stationary for one single experiment. This has been repeatedly tested by injecting non-sorbing tracers and measuring breakthrough.

The following **notation**⁷ is used:

P_i	: Injection point
P_w	: Extraction (withdrawal) point
P	: General field point
P_s	: Stagnation point
r, γ [m],[rad]	: Polar coordinates with origin at P_i
$r_w(r, \gamma)$ [m]	: Distance $\overline{P_w P}$
$\gamma_w(r, \gamma)$ [rad]	: Angle $(\overline{P_w P_i}, \overline{P_w P})$
r_s, γ_s [m],[rad]	: Coordinates of P_s
R [m]	: Radius indicating the outer boundary of the flow field
$\mathbf{v}(r, \gamma)$ [m/s]	: Flow velocity vector at P
$v_r(r, \gamma)$ [m/s]	: Component of \mathbf{v} in r direction
$v_\gamma(r, \gamma)$ [m/s]	: Component of \mathbf{v} in γ direction
$v(r, \gamma)$ [m/s]	: $ \mathbf{v}(r, \gamma) $
ρ [kg/m ³]	: Density of the fluid

⁷The stated units are typical consistent values. In the analysis of the experiments they are occasionally changed at our convenience.

a [m]	: Width (thickness) of the migration zone
ϵ [-]	: Flow porosity of the migration zone
(ϵa) [m]	: Flow width of the migration zone
T [m ² /s]	: Transmissivity of the migration zone
L_o [m]	: Dipole distance $\overline{P_i P_w}$
r_o [m]	: Radius of well (at P_i and P_w)
Q_i [m ³ /s]	: Water injection rate at P_i
Q_w [m ³ /s]	: Water extraction rate at P_w
β	: Q_w/Q_i
$\Phi(r, \gamma)$ [m]	: Hydraulic potential
Φ_o [m]	: Normalizing constant of the hydraulic potential
H [m]	: Background potential
$\Psi(r, \gamma)$ [m ² /s]	: Stream function
k [-]	: Streamline index (representing also a stream tube if $k \neq 0$)
ψ_k [m ² /s]	: Streamline constant (representing also a stream tube if $k \neq 0$)
Ω_k [rad]	: Streamline angle (representing also a stream tube if $k \neq 0$)
Q_{lm} [m ³ /s]	: Water flow within a stream tube bounded by the two streamlines (corresponding to ψ_l and ψ_m)
Q_k [m ³ /s]	: Water flow within a stream tube k
$d\mathbf{s}$ [m]	: Vector defining a line element
$d\mathbf{n}$ [m]	: Vector defining the normal to a line element
L_k [m]	: Length of the internal streamline k (representing also an internal stream tube if $k \neq 0$)
B_k [m]	: Average depth of the internal stream tube k
\bar{t}_k [s]	: Flow transit time along the internal streamline k (representing also an internal stream tube if $k \neq 0$)
\bar{v}_k [m/s]	: Average flow velocity along the internal streamline k (representing also an internal stream tube if $k \neq 0$)
k_{max} [-]	: Number of internal stream tubes within the half space ($0 \leq \gamma \leq \pi$)

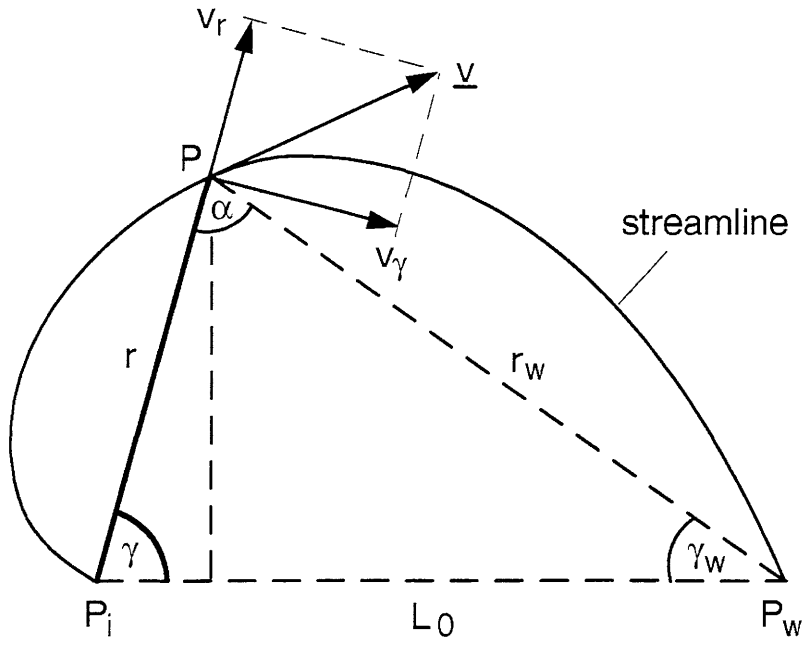


Figure 1. Representation of the flow field point P .

The basic equations of the model are:

Darcy's law⁸

$$\mathbf{v}(r, \gamma) = -\frac{T}{(\epsilon a)} \nabla \Phi(r, \gamma) \quad , \quad (1a)$$

$$\nabla \equiv (\nabla_r, \nabla_\gamma) \equiv \left(\frac{\partial}{\partial r}, \frac{1}{r} \frac{\partial}{\partial \gamma} \right) \quad . \quad (1b)$$

⁸ v is used instead of the usual Darcy velocity to keep (ϵa) explicitly in the equations since it is a fitting parameter in the analysis of breakthrough curves.

Conservation of mass⁹

$$\nabla \cdot \mathbf{v}(r, \gamma) = 0 \quad , \quad (2a)$$

$$\Delta \Phi(r, \gamma) = 0 \quad , \quad (2b)$$

$$\Delta \equiv \frac{\partial}{\partial r^2} + \frac{1}{r} \frac{\partial}{\partial r} + \frac{1}{r^2} \frac{\partial^2}{\partial \gamma^2} \quad . \quad (2c)$$

The potential field for a single injection well can directly be deduced from Eqs. (1) and (2b) taking into account the radial symmetry of the problem (compare e.g. Ref. [8], p. 147-149).

The inner boundary condition at the surface of the well ($r = r_o$) is determined by the radial symmetric injection flow, applying Eq. (1):

$$\frac{\partial \Phi(r)}{\partial r} \Big|_{r=r_o} = \frac{d \Phi(r)}{dr} \Big|_{r=r_o} = \frac{-Q_i}{2\pi r_o T} \quad . \quad (3a)$$

To achieve stationary flow an outer boundary at a finite radius R has to be defined. It is assumed that at a reasonable large R the potential is determined by a constant background potential H :

$$\Phi(r = R) = H \quad . \quad (3b)$$

Taking into account the boundary conditions, conservation of mass (cf. Eq. (2b)) leads to the following hydraulic potential field ¹⁰:

$$\Phi(r) = \frac{-Q_i}{2\pi T} \ln(r) + \left(\frac{Q_i}{2\pi T}\right) \ln(R) + H \quad (3c)$$

with $r \geq r_o$,

⁹For unsteady flow and compressible fluid, the density ρ would be dependent on r, γ, t and conservation of mass would have to be expressed by $\partial \rho / \partial t + \nabla \cdot (\rho \mathbf{v}) = 0$ instead of Eq. (2a).

¹⁰In Eq. (3c), $\ln(r)$ is used instead of the usual $\ln(r/R)$ to be able to drop R in the subsequent equations.

and to allow for arguments not being dimension-less

$$\ln(w) = \int_1^w \frac{1}{\xi} d\xi \quad ; \quad w = r \text{ or } R \quad .$$

The velocity and the advection time of radial flow from a single injection well are added here because of its usefulness for quick estimates (cf. Eqs. (1) and (3c)):

$$v_r(r) = \frac{Q_i}{2\pi(\epsilon a)} \cdot \frac{1}{r} \quad ; \quad v_\gamma \equiv 0 \quad (3d)$$

$$\bar{t}(r) = \int_{r_o}^r \frac{d\tilde{r}}{v_r(\tilde{r})} = \frac{\pi(\epsilon a)}{Q_i} (r^2 - r_o^2) \quad . \quad (3e)$$

The equation for velocity $v_r(r)$ shows that the fluid flow through the outer boundary corresponds to the injection rate ($2\pi \cdot R \cdot (\epsilon a) \cdot v(R) = Q_i$) which is a consequence of conservation of mass and not a boundary condition. For an extraction well, equations similar to Eqs. (3d) and (3e) could be derived¹¹.

The potential field of the dipole is calculated as superposition of the injection field (single well at P_i) and the extraction field (single well at P_w). This is justified by the linearity of the field equation (2b) and by the fact that the outer boundary is far outside the region of interest¹²:

$$\Phi(r, \gamma) = \Phi_o - \frac{Q_i}{2\pi T} \ln(r) + \frac{Q_w}{2\pi T} \ln(r_w(r, \gamma)) \quad , \quad (4a)$$

$$\begin{aligned} \text{with } r_w(r, \gamma) &= \sqrt{r^2 - 2rL_o \cdot \cos(\gamma) + L_o^2} & (4b) \\ \Phi_o &= \text{constant (determined by the background} \\ &\quad \text{potential and the outer boundary).} \end{aligned}$$

$$\begin{aligned} r &\geq r_o \\ r_w(r, \gamma) &\geq r_o \end{aligned}$$

¹¹ Q_i replaced by Q_w , v_r replaced by $-v_r$, and integration limits interchanged.

¹²The outer boundaries of the 2 single well fields are displaced by the dipole distance $L_o \ll R$. The outer boundary of the total field is therefore not well defined. This is not of importance when representing the potential field in the vicinity of the bore holes.

The velocity field of the dipole can directly be deduced from the potential field according to Eq. (1):

$$v_r(r, \gamma) = \frac{Q_i}{2\pi(\epsilon a)} \left[\frac{1}{r} + \frac{\beta (L_o \cos(\gamma) - r)}{r_w^2(r, \gamma)} \right] , \quad (5a)$$

$$v_\gamma(r, \gamma) = \frac{-Q_i}{2\pi(\epsilon a)} \left[\frac{\beta L_o \sin(\gamma)}{r_w^2(r, \gamma)} \right] , \quad (5b)$$

$$\beta = \frac{Q_w}{Q_i} > 1 . \quad (5c)$$

The velocity is expressed in terms of pumping rates (Q_i , $\beta = Q_w/Q_i$) instead of the more commonly used pumping pressures. This is in line with the experimental set-up where the pumping rates are kept constant. As a consequence the velocity is independent of transmissivity.

To prevent flow from P_i to the outer boundary, the migration experiments are restricted to $\beta > 1$. The theoretical considerations take over this restriction to avoid unnecessary complications.

The representation of the flow field can be simplified¹³ by introducing the stream function $\Psi(r, \gamma)$. A possibility to define the stream function are the **Cauchy-Riemann conditions** (e.g. Ref. [7], p. 119¹⁴):

$$v_r(r, \gamma) = -\frac{T}{(\epsilon a)} \nabla_r \Phi(r, \gamma) = -\nabla_\gamma \Psi(r, \gamma) , \quad (6a)$$

$$v_\gamma(r, \gamma) = -\frac{T}{(\epsilon a)} \nabla_\gamma \Phi(r, \gamma) = +\nabla_r \Psi(r, \gamma) . \quad (6b)$$

¹³This is possible since the macroscopic flow field is two dimensional, stationary, a potential field and therefore irrotational ($\nabla \times \mathbf{v} = 0$), isochoric and having the source as well as the sink excluded by boundary conditions ($\nabla \cdot \mathbf{v} = 0$).

¹⁴Eq. (4.6.8) of Ref. [7] written in polar coordinates, keeping our definitions of Ψ and Φ , using \mathbf{v} instead of \mathbf{q} and taking into account that T and (ϵa) are constant. It is worth noting that an alternative representation of the Cauchy-Riemann conditions (normally used in physics textbooks) is possible which has changed signs of $\nabla_\gamma \Psi$ and $\nabla_r \Psi$ in Eqs. (6) and would lead to the opposite direction of $\nabla \Psi$.

Eqs. (6) essentially mean that $\nabla\Psi$ is perpendicular to \mathbf{v} and $\nabla\Phi$ (cf. Fig. 2)¹⁵:

$$\mathbf{v} \cdot \nabla \Psi = 0 \quad , \quad (6c)$$

$$\nabla\Phi \cdot \nabla\Psi = 0 \quad . \quad (6d)$$

Eqs. (6) include implicitly the continuity Eq. for an incompressible¹⁶ fluid in steady state:

$$\nabla \cdot \mathbf{v} = 0 \quad . \quad (6e)$$

Combining Eqs. (5) with Eqs. (6) and normalizing to $\Psi(r, \gamma = 0) = 0$ leads to the following expressions for the **stream function** $\Psi(\mathbf{r}, \gamma)$ ¹⁷:

$$\Psi(r, \gamma) = \frac{-Q_i}{(\epsilon a)} \cdot \frac{[\gamma + \beta \gamma_w(r, \gamma)]}{2\pi} \quad , \quad (7a)$$

$$\gamma_w(r, \gamma) = \text{arc cos} \left(\frac{L_o - r \cos(\gamma)}{r_w(r, \gamma)} \right) \quad . \quad (7b)$$

The range of consideration can be limited to half of the migration zone since the flow field is symmetric with respect to the axis $\overline{P_i P_w}$:

$$0 \leq \gamma \leq \pi \longrightarrow 0 \leq \gamma_w \leq \pi \quad . \quad (7c)$$

The instantaneous curves that are at every point tangent to the direction of the velocity at that point are called **streamlines**. Since $\nabla\Psi$ is normal to \mathbf{v} and always normal to the line $\Psi = \text{const.}$, this line must be tangent to \mathbf{v} . Therefore, the condition of a streamline is satisfied by

$$\Psi(r, \gamma) = \psi_k = \text{const.} \quad . \quad (8a)$$

¹⁵For an anisotropic transmissivity, Eq. (6c) would still be valid but not Eq. (6d).

¹⁶For a compressible fluid, Eq. (6) would have to be reformulated so that $\nabla\psi$ is correlated to $\rho \mathbf{v}$ instead of \mathbf{v} . By this measure the continuity equation for a compressible fluid $\nabla \cdot (\rho \mathbf{v}) = 0$ is implicitly fulfilled.

¹⁷The detailed calculation is omitted. In Eq. (7b) an *arc cos* is used because it is single valued and has no arguments that are infinite in the range $0 \leq \gamma_w \leq \pi$. Geometrical considerations show that other expressions such as $\gamma_w(r, \gamma) = \text{arc tg} [r \cdot \sin(\gamma)/(L_o - r \cos(\gamma))]$ are also possible (if adequate care is taken).

The change of Ψ along a point moving with the flow is indicated by the substantial derivative:

$$\frac{D\Psi}{Dt} = \frac{\partial\Psi}{\partial t} + \mathbf{v} \cdot \nabla\Psi \quad . \quad (8b)$$

In a steady state the first term is zero. According to Eq. (6c) the second term, too, has to be zero:

$$\frac{D\Psi}{Dt} = 0 \quad . \quad (8c)$$

Therefore, the path of a point moving with the flow is a streamline (a line $\Psi = \text{const.}$)¹⁸. According to Eq. (6d) streamlines are perpendicular to the lines of constant potential.

Renormalizing the streamline constant ψ_k leads to a **streamline equation** which represents a simple relation of angles (compare Eq. (7a) and Fig. 1):

$$\gamma + \beta \gamma_w(r, \gamma) = \Omega_k = \text{constant} \quad , \quad (8d)$$

$$\Omega_k = - \frac{2\pi(\epsilon a)}{Q_i} \psi_k \quad . \quad (8e)$$

The corresponding relation between r_k and γ can be written as¹⁹

$$r_k(\gamma) = L_0 \frac{\sin\left(\frac{(\Omega_k - \gamma)}{\beta}\right)}{\sin\left(\frac{(\Omega_k - \gamma)}{\beta} + \gamma\right)} \quad . \quad (8f)$$

Since $\gamma_w = 0$ at $P = P_i$ and $\gamma = 0$ at $P = P_w$ (see Fig. 1) the renormalized streamline constant Ω_k can be interpreted as streamline angle:

$$\Omega_k = \gamma \quad : \text{ Injection angle of streamline } k \text{ at } P_i \quad , \quad (8g)$$

$$\Omega_k/\beta = \gamma_w(L_0, 0) : \text{ Extraction angle of streamline } k \text{ at } P_w \quad . \quad (8h)$$

¹⁸In unsteady flow, path lines and streamlines are different (Eq. (8c) is not fulfilled any longer).

¹⁹For $\Omega_k = 0$ the streamline is the straight line $\overline{P_i P_w}$ (cf. Eq. (8d)). For $\Omega_k = \pi$ the streamline is discussed later and presented more accurately by Eq. (11f) for $\gamma = \pi - \delta\gamma$, ($\delta\gamma \ll \pi$).

Geometrical considerations ($0 \leq \gamma \leq \pi$, $\beta > 1$) yield the ranges of streamline angle Ω_k :

$$0 \leq \Omega_k \leq \pi \quad \text{for internal streamlines (originating at } P_i \text{ and ending at } P_w) \quad , \quad (8i)$$

$$\pi \leq \Omega_k \leq \beta \pi \quad \text{for external streamlines (originating at the outer boundary and ending at } P_w). \quad (8j)$$

Eqs. (8d), (7b) and (4b) show that the streamlines are only dependent on the dipole distance L_0 and the pumping rate ratio β but not on either the flow width (ϵa) or on the absolute values of the pumping rates (Q_i and Q_w).

A **stream tube** is a region bounded by 2 streamlines and, in our case, having the width a of the migration zone.

The **flow in a stream-tube** can be expressed by (cf. Fig. 2)²⁰

$$Q_{lm} = (\epsilon a) \int_{P_l}^{P_m} \mathbf{v} \cdot d\mathbf{n} \quad . \quad (9a)$$

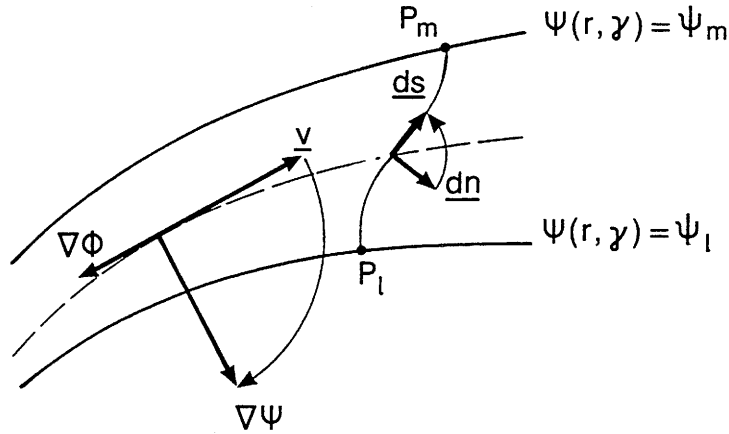


Figure 2 Notation describing the stream tube flow.

²⁰ $d\mathbf{n}$ defines the direction of positive flow across the line $P_l P_m$. It is chosen so that it is consistent with the direction of \mathbf{v} .

Applying Cauchy-Riemann (cf. Eqs. (6)) and taking into account that $\nabla\Psi$ is obtained from \mathbf{v} by a clockwise rotation of $\pi/2$ and $d\mathbf{s}$ from $d\mathbf{n}$ by a counter-clockwise rotation of $\pi/2$ we get

$$Q_{lm} = -(\epsilon a) \int_{P_i}^{P_m} \nabla\Psi \cdot d\mathbf{s} \quad . \quad (9b)$$

$(\nabla\Psi \cdot d\mathbf{s})$ is the differential of Ψ along the line element $d\mathbf{s}$. Therefore, Eq. (9b) can be written as²¹

$$Q_{lm} = -(\epsilon a) \int_{\psi_l}^{\psi_m} d\Psi = -(\epsilon a)[\psi_m - \psi_l] \quad . \quad (9c)$$

According to Eqs. (9c) and (8d) the flow in a stream tube can be expressed as follows:

a) for internal stream tubes originating at P_i :

$$Q_{lm} = Q_i \frac{(\Omega_m - \Omega_l)}{2\pi} \quad \text{for } 0 > \Omega_m \leq \pi \text{ and } \Omega_l < \Omega_m \quad , \quad (9d)$$

$$Q_{lm} = Q_w \frac{(\frac{\Omega_m}{\beta} - \frac{\Omega_l}{\beta})}{2\pi} \quad \text{for } 0 < \Omega_m \leq \pi \text{ and } \Omega_l < \Omega_m \quad . \quad (9e)$$

b) for external stream-tubes originating at the outer boundary:

$$Q_{lm} = Q_w \frac{(\frac{\Omega_m}{\beta} - \frac{\Omega_l}{\beta})}{2\pi} \quad \text{for } \pi < \Omega_m \leq \beta \pi \text{ and } \Omega_l < \Omega_m \quad . \quad (9f)$$

It shows that the flow in an internal stream tube is completely determined by the injection rate and the range of relative injection angle $(\Omega_m - \Omega_l)/2\pi$. It is not dependent on the extraction rate Q_w but can be expressed in terms of the extraction rate and the range of relative extraction angle $(\Omega_m/\beta - \Omega_l/\beta)/2\pi$. Flow in the external stream tubes, on the other hand, is determined by the extraction rate and the range of relative extraction angle. Eqs. (9d) to

²¹The negative signs on the left side of Eqs. (9b), (9c) but also (7a) and (8e) are due to the definition of the stream function in Eq. (6) which directs $\nabla\Psi$ to the streamline l so that $\psi_l > \psi_m$.

(9f) reflect the fact that the azimuthal flow distributions at the injection and the extraction well are symmetric.

To illustrate the features of the flow field, a typical example of the field is depicted in Fig. 3.

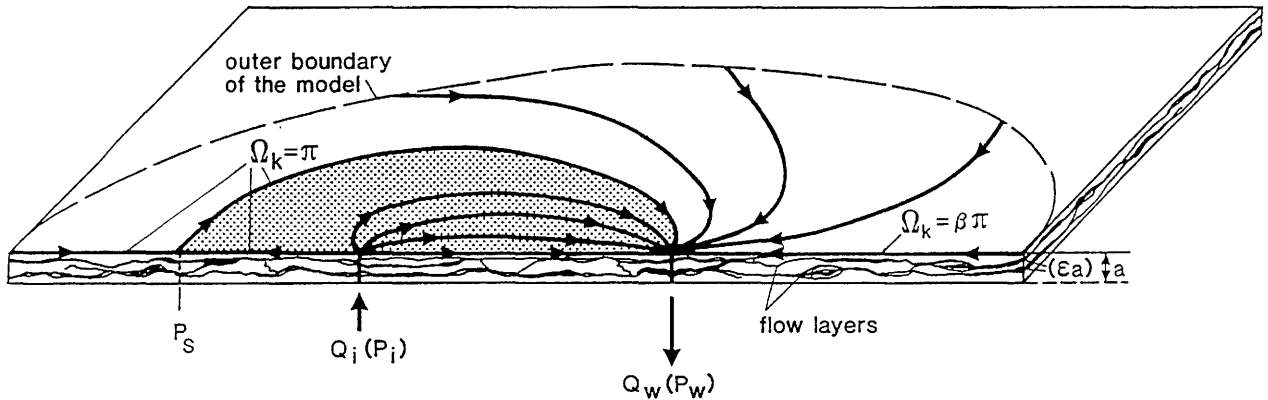


Figure 3 Idealized dipole flow field in the migration zone represented by a few streamlines. The extraction rate $Q_w (P_w)$ is higher than the injection rate $Q_i (P_i)$, generating a restricted internal flow region of the injected water (shaded area).

The figure shows the migration zone²² which, at the Grimsel Test Site, is orientated so that the axis $\overline{P_i P_w}$ is subhorizontal and the plane subvertical. The streamlines represent a dipole flow field generated by a fluid injection rate Q_i at P_i being a factor 2 smaller than the extraction rate Q_w at P_w . The width a of the migration zone is scaled up by a factor 10 to show the different layers of fluid flow. They are taken into account by the average flow width (ϵa) representing the space covered by the fluid in the third dimension. It is useful to note the following features:

- The flow field can be divided into 2 regions. The first, indicated as darker part and characterised by the internal streamlines, contains the injected water; the second characterised by the external streamlines contains external fracture water. Internal and

²²Since the flow field is symmetric, only half of the migration zone is presented.

external water, completely separated in the migration zone, are mixed in the extraction well.

- The streamlines representing the flow field in Fig. 3 are chosen so that the individual flow between 2 lines is equal throughout the whole field. Most of the internal flow is concentrated near the dipole axis $\overline{P_i P_w}$ showing a relatively high velocity²³. Only a small part is spread over a larger area and flowing slowly. The external flow is fairly slow as long as it has not reached the close vicinity of the extraction well²⁴.
- As a consequence of $(Q_w/Q_i) = 2$, the extraction angles of the internal streamlines are a factor of 2 smaller than the corresponding injection angles (cf. Eqs. (8g) and (8h)). This is the reason why the boundary line between internal and external flow region has the extraction angle $\Omega_k/\beta = \pi/2$.
- Special attention has to be drawn to the streamline defined by the streamline angle $\Omega_k = \pi$. One solution of the corresponding streamline equation (8d) is the line $\gamma = \pi$. The velocity on this line is determined by Eqs. (4b) and (5):

$$v_r(r, \pi) = \frac{Q_i}{2\pi(\epsilon a)} \left[\frac{L_o - (\beta - 1)r}{r^2 + L_o r} \right] , \quad (10a)$$

$$v_\gamma(r, \pi) = 0 . \quad (10b)$$

A stagnation point $P_s(r_s, \gamma_s)$ is generated where the internal flow ($v_r(r, \pi) > 0$) collides with the external flow ($v_r(r, \pi) < 0$). The position r_s is determined by the condition $v_r(r, \pi) = 0$ leading to the following coordinates of the stagnation point:

$$r_s = \frac{L_o}{(\beta - 1)} , \quad (11a)$$

$$\gamma_s = \pi . \quad (11b)$$

A mass point starting at P_i and travelling along the streamline $\Omega_k = \pi$ requires the following time to reach P_s :

$$t_s = \int_0^{r_s} \frac{dr}{v_r(r, \pi)} . \quad (11c)$$

²³Small distances between two streamlines indicate high velocities.

²⁴Under the assumption of an unperturbed dipole.

Using Eqs. (10a) and (11a) and integrating leads to

$$t_s = \frac{2\pi(\epsilon a)}{Q_i} \left[\frac{-\beta L_o^2}{(\beta-1)^3} \ln \{L_o - (\beta-1)r\} + f(r) \right]_o^{r_s}, \quad (11d)$$

with $f(o)$ and $f(r_s)$ being finite.

Applying the limits shows:

$$t_s = +\infty. \quad (11e)$$

An infinite time is necessary to reach the stagnation point. The same is true for a corresponding mass point coming from the outer boundary along the line $\gamma = \pi$.

At P_s the streamline $\Omega_k = \pi$ is branching out. The second branch leaving the line $\gamma = \pi$ defines the boundary between the internal and external flow region. Some information of this branch near P_s is obtained by investigating the streamline at the angle $\gamma = \pi - \delta\gamma$ with $\delta\gamma \ll \pi$. Expanding Eq. (8f) and calculating the line element δs at P_s corresponding to Eq. (12a) we get:

$$r_k(\Omega_k = \pi, \gamma) = r_s \left[1 + \frac{(\beta-2)}{6\beta} \cdot (\delta\gamma)^2 + \mathcal{O}\{(\delta\gamma)^4\} \right], \quad (11f)$$

$$\delta s(\Omega_k = \pi, \gamma) = (\mathcal{O}\{(\delta\gamma)^2\}, r_s \cdot [1 + \mathcal{O}\{(\delta\gamma)^2\}] \cdot \delta\gamma), \quad (11g)$$

$$\gamma = \pi - \delta\gamma; \quad \text{with } 0 < \delta\gamma \ll \pi. \quad (11h)$$

It shows that at P_s the second branch is crossing the line $\gamma = \pi$ at a right angle and at a curvature corresponding to a circle of radius r_s centred at P_i .

- For a fixed dipole distance L_o the streamlines and flow regions are determined completely by the extraction to injection rate ratio β . If β is sufficiently larger than 1, the internal flow region is limited to the vicinity of the dipole axis $\overline{P_i P_w}$. The closer β moves to 1, the larger the spread of the internal region. For the limit of $\beta = 1$ the internal flow field is spreading over the entire space (cf. Eq. (8f) with $\Omega_k = \pi$) and the stagnation point is positioned at $r_s = \infty$ (cf. Eq. (11a)). In this case any streamline k is the locus of points at which the dipole axis $\overline{P_i P_w}$ subtends the constant angle $\alpha(\Omega_k) = \pi - \Omega_k$ (cf. Eq. (8d) and Fig. 1). Therefore streamlines are circles over $\overline{P_i P_w}$ for $\beta = 1$.

To increase the conception of dipole flow field behaviour, **streamline figures** for the same dipole length ($L_0 = 4.9$ m) but different extraction to injection rate ratios ($\beta = 15, 3, 1.5$) are shown in Fig. 4 (solid lines = internal streamlines; dashed lines = external streamlines). The streamlines represent equal stream tube flow within the internal as well as the external flow region²⁵. The figure for $\beta = 15$, corresponding roughly to the experiments selected for analysis, demonstrates the narrowness of the internal flow region (half width $z_{max} \approx 0.7$ m). The internal streamlines indicate a fairly uniform flow field. The stagnation point is positioned relatively close to the injection point ($r_s = 0.35$ m) resulting in only a small range with low velocities. The external flow is not too far from a pure extraction flow as indicated by straight streamlines. For $\beta = 3$ the internal flow field is more spread out (half width $z_{max} \approx 3$ m) the stagnation point further away from the injection point ($r_s = 2.45$ m) and the external streamlines have a stronger curvature. The picture for $\beta = 1.5$ demonstrates the tendency of the internal flow field to spread over the whole space and to be represented by streamlines which are circles over the dipole axis both typical for an equal dipole flow field ($\beta = 1$).

The length of an internal streamline can be expressed by the following equations:

$$ds_k(\gamma) = \left(\frac{dr_k(\gamma)}{d\gamma} d\gamma, r_k(\gamma)d\gamma \right) , \quad (12a)$$

$$ds_k(\gamma) = d\gamma \cdot \sqrt{\left(\frac{dr_k(\gamma)}{d\gamma} \right)^2 + r_k^2(\gamma)} , \quad (12b)$$

$$L_k = \int_{\gamma=0}^{\Omega_k} ds_k(\gamma) - 2r_o . \quad (12c)$$

²⁵For $\beta = 15$ and 3 internal and external stream tube flow is different to avoid overloading the picture.

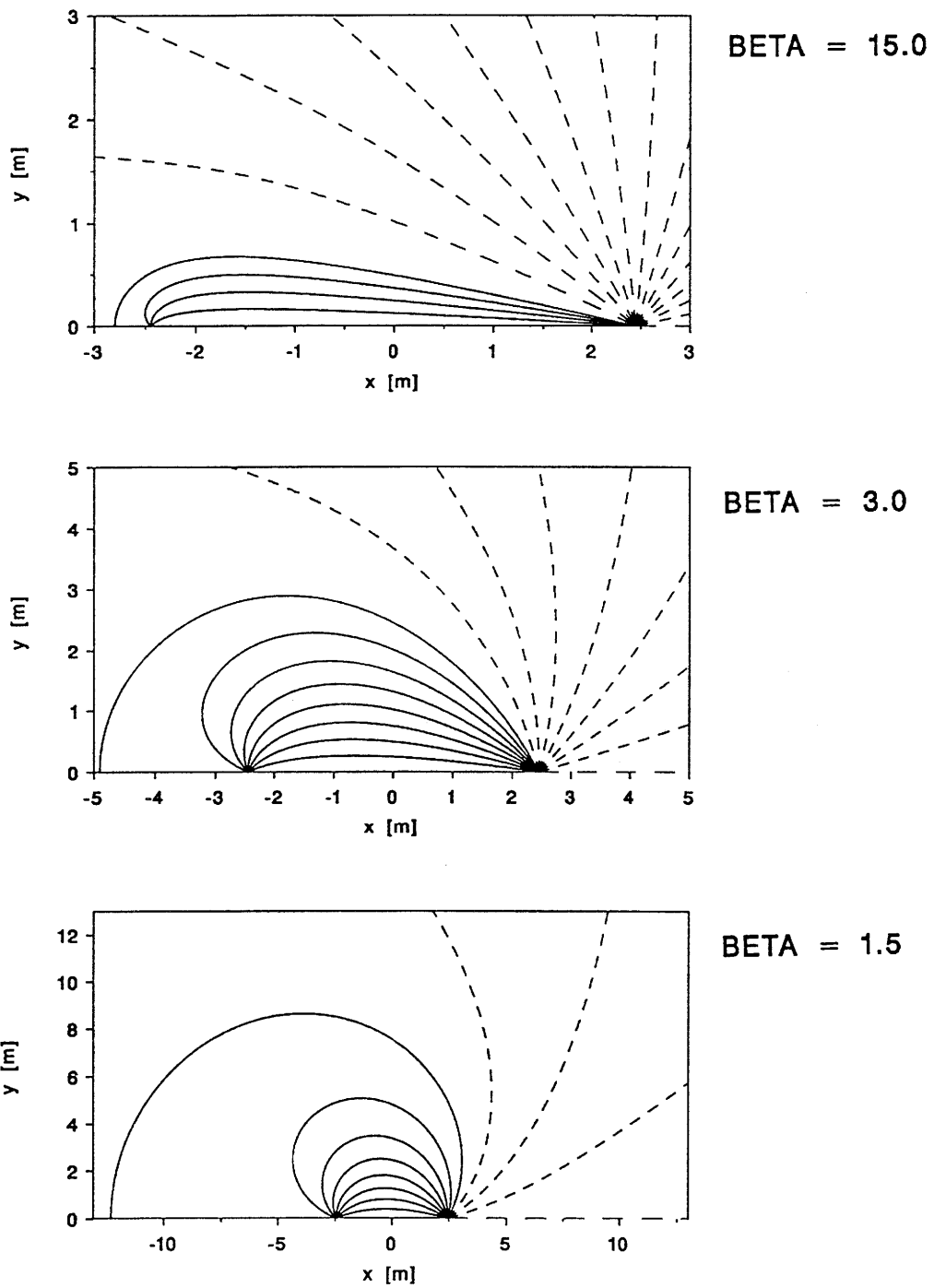


Figure 4 Influence of the extraction to injection rate ratio (β) on the flow field. Top picture: Typical experimental flow field conditions. Lower pictures: Reducing β deforms the internal streamlines gradually towards the circles of the equal dipole.

The calculation of the streamline length L_k can be performed numerically using the relation $r_k(\gamma)$ given in Eq. (8f). Note that:

$$L_k = L_k(\Omega_k, \beta, L_o, r_o) \quad , \quad (12d)$$

$$L_k \sim L_o \quad (\text{neglecting the small correction for the well radii } r_o). \quad (12e)$$

The flow transit time along an internal streamline is given by the following expression²⁶:

$$\bar{t}_k = \int_{\gamma=\Omega_k}^0 \frac{\mathbf{v}(r_k(\gamma), \gamma) \cdot d\mathbf{s}_k(\gamma)}{v^2(r_k(\gamma), \gamma)} \quad . \quad (13a)$$

The calculation of \bar{t}_k is performed numerically taking into account Eqs. (5a),(5b), (8f) and (12a). It is of note that as soon as velocities and times are required, the absolute pumping rates ($Q_i, \beta Q_i = Q_w$) and the flow width (ϵa) have to be considered (in addition to L_o and β):

$$\bar{t}_k = \bar{t}_k(\Omega_k, Q_i, \beta, (\epsilon a), L_o) \quad . \quad (13b)$$

From $r_k(\gamma) \sim L_o$ results $v(r_k, \gamma) \sim 1/L_o$ and $ds_k(\gamma) \sim L_o$ (cf. Eqs. (8f), (4b),(5) and (12a)). Taking into account also Eq. (13a) we observe:

$$\bar{t}_k \sim L_o^2 \quad . \quad (13c)$$

An average flow velocity \bar{v}_k along an internal streamline can be defined by

$$\bar{v}_k = \frac{L_k}{\bar{t}_k} \quad , \quad (14a)$$

²⁶For negative values of $d\gamma$, used in the integration from Ω_k to 0, the vector $d\mathbf{s}_k(\gamma, d\gamma)$ has the same direction as $\mathbf{v}(r_k(\gamma), \gamma)$. The value of \bar{t}_k is calculated from P_i to P_w neglecting the well radii r_o . This is a good approximation (cf. Eqs. (5a) and (5b)).

$$\bar{v}_k \sim \frac{1}{L_0} . \quad (14b)$$

The **smallest transit time**²⁷ corresponds to the flow along a straight line from P_i to P_w ²⁸. This is the shortest internal stream line and has the highest flow velocities²⁹. Along this line the transit time can be expressed as

$$\bar{t}_o = \int_o^{L_o} \frac{dr}{v_r(r, o)} . \quad (15a)$$

Inserting $v_r(r, o)$ from Eq. (5a) and integrating leads to the following analytical expression (compare also Ref. [13]):

$$\bar{t}_o = \frac{\pi(\epsilon a)}{Q_w} L_o^2 \cdot W_o(\beta) , \quad (15b)$$

$$W_o(\beta) = \frac{\beta}{(\beta-1)^2} \left[(\beta+1) - \frac{2\beta}{(\beta-1)} \cdot \ln \beta \right] , \quad (15c)$$

$$W_o(\beta) = \frac{1}{3} \left[1 + \frac{\delta\beta}{2} + o\{(\delta\beta^2)\} \right] \quad \text{for } \beta = 1 + \delta\beta , \delta\beta \ll 1 , \quad (15d)$$

$$\lim_{\beta \rightarrow \infty} W_o(\beta) = 1 \quad \text{corresponds to monopole extraction flow.} \quad (15e)$$

Increasing $Q_i \leq Q_w$ (and keeping Q_w constant) reduces \bar{t}_o . The maximum reduction, a factor of 3, is obtained comparing an equal dipole to a monopole.

²⁷This time is occasionally useful as a first guess of the advection time in a dipole field.

²⁸ $\Omega_o = 0$ in Eq. (8d) corresponds to this line.

²⁹Inserting Eqs. (5a) and (5b) into $v(r, \gamma) = \sqrt{v_r^2(r, \gamma) + v_\gamma^2(r, \gamma)}$ shows directly that: $v(r, \gamma=0) > v(r, \gamma \neq 0)$.

3.2 Tracer Nuclide Transport

3.2.1 Basic Procedure

The internal flow field of the half space ($0 \leq \gamma \leq \pi$) is divided into k_{max} stream tubes each carrying equal parts Q_k of the total flow³⁰:

$$Q_k = \frac{Q_i}{2k_{max}} = constant. \quad (16a)$$

Within a stream tube, a characteristic streamline is chosen separating the stream tube flow into two halves, the injection angle given by:

$$\Omega_k = \frac{(k - \frac{1}{2})\pi}{k_{max}}. \quad (16b)$$

Along this streamline, length L_k and average velocity \bar{v}_k are determined (cf. Eqs. (12c), (13a) and (14a)). Using these parameters³¹ each stream tube flow is approximated by a 1D-flow assuming a consistent average cross section $(\epsilon a) \cdot B_k$ as indicated in Fig. 5:

$$(\epsilon a) \cdot B_k = \frac{Q_k}{\bar{v}_k}. \quad (16c)$$

The total flow from P_i to P_w can now be represented by a superposition of different 1D-flow fields. Tracer nuclide transport is calculated for these 1D-flow fields (assuming constant concentration perpendicular³² to the fluid flow direction and neglecting transverse nuclide flow between adjacent stream tubes). The breakthrough curve $C_f(t)$, at P_w is a superposition of the stream tube outflow concentrations $C_{fBk}(t)$, defined in Eq. (18f), weighted with the ratio of

³⁰Compare Eq. (9d).

³¹The approximation of a constant water velocity \bar{v}_k within a stream tube is justified by relatively small velocity variations with exception of the immediate neighbourhood of the wells (cf. Ref. [5], p. 24).

³²i.e. along B_k of Fig. 5.

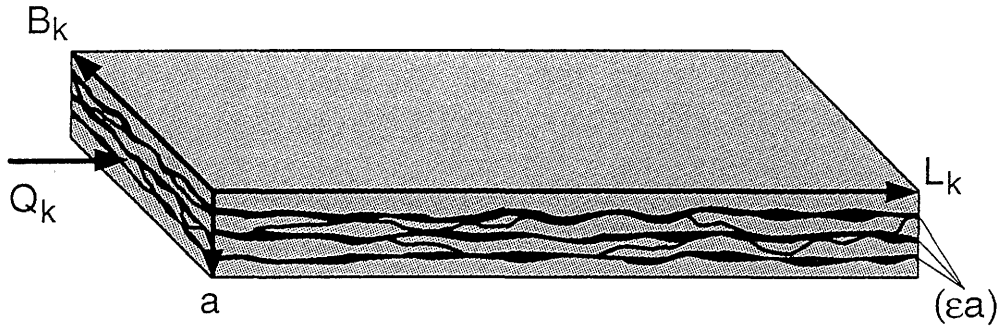


Figure 5 Schematic representation of a stream tube in the 1D-approximation.

stream tube flow $Q_i/2k_{max}$ to total outflow $Q_w/2$ (within the half space):

$$C_f(t) = \left(\frac{Q_i}{Q_w} \right) \cdot \frac{1}{k_{max}} \sum_{k=1}^{k_{max}} C_{fBk}(t) \quad . \quad (17a)$$

The normalization of the breakthrough curve (using the tracer injection concentration $C_0(t)$ and the total tracer mass M_0) can be expressed by

$$Q_w \int_0^{\infty} C_f(t) dt = Q_i \int_0^{\infty} C_0(t) dt = M_0 \quad . \quad (17b)$$

The number of stream tubes necessary to represent flow and nuclide transport adequately is dependent on the flow field and the required accuracy (within the model assumptions) of the final breakthrough curve³³. By this procedure widening³⁴, tailing³⁵ and dilution³⁶ of the tracer pulse by the dipole flow is taken into account.

Valid information on the **structural geology** is of great help in modelling nuclide transport. It is described in Ref. ([10], particularly important are p.20-30 and p.47-49) and summarized

³³In this work narrow dipole fields are used ($\beta \approx 15$) and therefore $k_{max} = 5$ is adequate.

³⁴Due to small flow field differences in the stream tubes near the dipole axis.

³⁵Due to the contributions from stream tubes near the boundary of the internal flow region (see also Appendix 8).

³⁶Due to mixing with external fracture water (which is assumed to be instantaneous).

in Ref. ([3], section 3.1). A simplified representation is given in Fig. 6. From the structural point of view the migration zone is considered to be the region of high flow porosity in the migration shear-zone described in Ref. [10]. The flow porosity is caused mainly by a small number of interconnected fractures, partially filled with highly porous micaceous fault gouge. These fractures are connected to sheet silicate pores (in the mylonite) and to grain boundary pores (in the granodiorite mainly, but also in quartz ribbons within the mylonite). Although basically representing an open porosity, both types of pores are so narrow that they can contain to a large extent practically stagnant³⁷ water. Similarly this might be true for certain parts of the fault gouge.

The **nuclide transport part of the model** is based on a dual porosity concept as indicated in Fig. 6. The migration zone is modelled as several planar water conducting zones without infill, representing small channelled regions of flowing water within the fault gouge. They are separated by porous rock zones representing rock regions with stagnant pore water (mainly fault gouge but also mylonite and granodiorite). In the water conducting zones, nuclide transport is governed by advection and dispersion - the latter accounting for variability of zone geometry and water velocity, for zone interconnections as well as for possible sorption heterogeneities³⁸ along the flow path³⁹. Nuclide diffusion into stagnant water of the porous rock zones (matrix diffusion) is taken into account perpendicular to advective transport⁴⁰. Sorption on surfaces of the water conducting zones (surface sorption) as well as on the pore surfaces of the porous rock zones (bulk sorption) is calculated under the assumption of instantaneous equilibrium. In batch sorption experiments, often slow sorption kinetics is observed which is a combination of diffusion kinetics of tracer into the rock samples and kinetics of the sorption reaction in the surface layers. The first mechanism is taken into account explicitly by the matrix diffusion mechanism. For nuclide concentrations far below natural background, a linear sorption isotherm is used. For higher concentrations non-linear sorption can be taken into account, e.g. by using a Freundlich isotherm.

³⁷Stagnant with respect to the time scale of the experiments.

³⁸The contribution of sorption heterogeneities to dispersion is considered in Ref. [14].

³⁹Dispersion basically is dependent on the largest type of flow heterogeneity and therefore on the migration length.

⁴⁰This does not mean considering only pore spaces perpendicular to advective flow but, on a macroscopic scale, neglecting (in the porous rock zones) diffusion in advective flow direction with respect to the much larger effect of dispersion in the water conducting zones. On a microscopic scale however the geometry of the pore network reduces substantially nuclide propagation in the considered direction which is taken into account by a "pore diffusion coefficient". In our application it is an order of magnitude smaller than the free fluid diffusion coefficient. In general terms, the pore diffusion coefficient would be a second rank tensor (cf. Ref. [7] p. 165, comment to Eq. (6.2.15)).

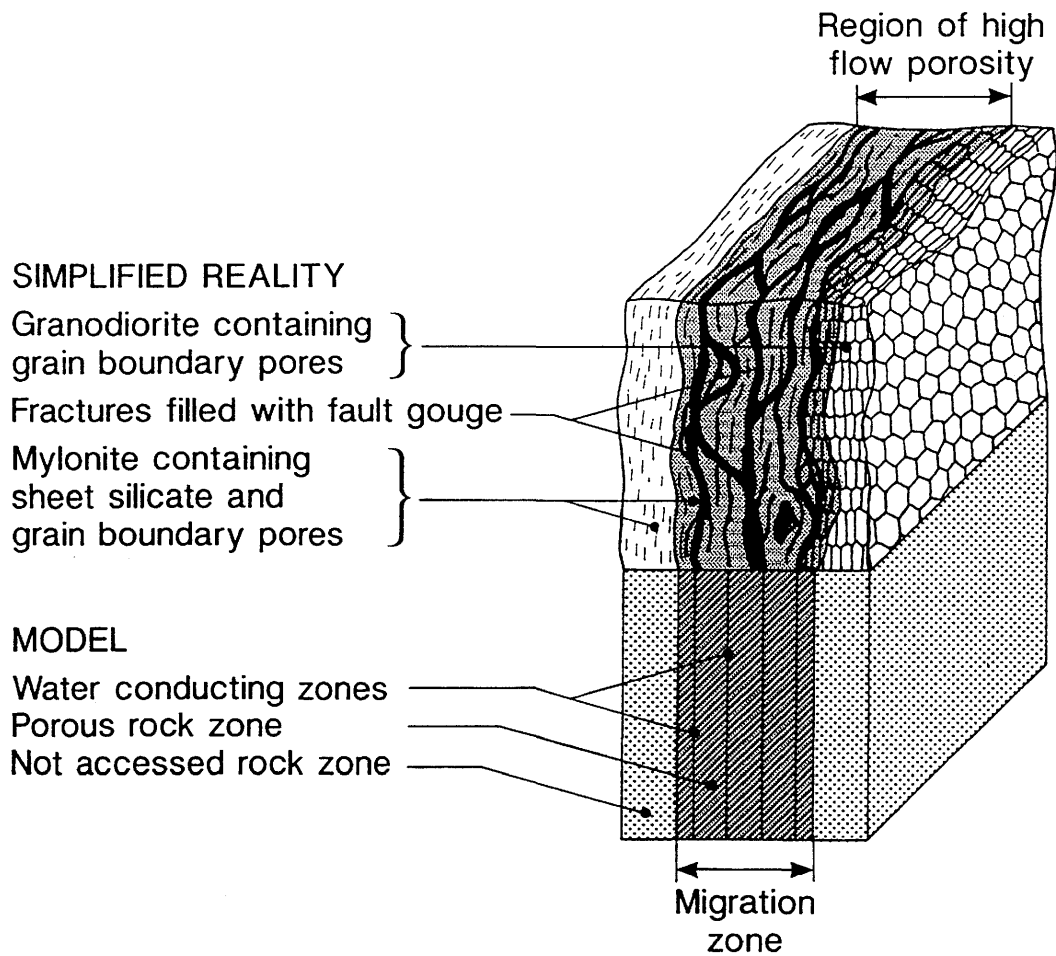


Figure 6 Based on structural geology results (upper part) a conceptual model for the geometrical structure is derived (lower part).

3.2.2 Transport Equations

To provide further insight into the model, the main equations are given here. They are to a large extent a selection of results relevant to our application taken from the original literature Ref. ([6], p.9-20).

The following **assumptions** are made in addition to the approximations of section 3.2.1:

1. Nuclide concentrations (dissolved or sorbed) and the transport parameters (including the water velocity) are macroscopic continuum quantities. They describe microscopic values averaged over the corresponding portion of a representative equivalent volume⁴¹. Advective, dispersive and diffusive nuclide fluxes are deduced from the macroscopic concentrations using the transport parameters.
2. Time and space dependence of macroscopic transport parameters are neglected.
3. Temperature is assumed constant (no consideration of conservation of energy).
4. Molecular diffusion in direction of advective flow within the water conducting zones is neglected with respect to dispersion (diffusion coef. \ll dispersion coef.).
5. Dispersion is considered only in direction of advective flow. The corresponding dispersion coefficient is assumed to be proportional to the water velocity (i.e. expressible by the product of water velocity and dispersion length⁴²). It can be described by Fick's law, representing the macroscopic effect of a large number of microscopic heterogeneities. It has to be kept in mind that Fick's law represents reality only a few dispersion lengths away from boundaries or discontinuities.
6. Molecular diffusion across⁴³ the narrow individual water conducting zones is not considered explicitly (obviously it provides the nuclide source for the matrix diffusion

⁴¹Compare e.g. Ref. ([7], p. 17-21). In our application a separate portion of the representative equivalent volume has to be considered for the water conducting and for the porous rock zones.

⁴²In general, the dispersion length (or dispersivity) is a fourth rank tensor relating the components of the water velocity and a velocity dependent function to the components of the dispersion coefficient, a velocity dependent second rank tensor (cf. Ref. [7], p. 161, Eq. (6.2.6)). In our simplification considering one dimension only, the dispersion length is a scalar leading to the (scalar) dispersion coefficient if multiplied with the velocity and the velocity dependent function. Approximating this function by 1 is valid for a large range of fluid velocities (including the Grimsel experiments with Peclet number $Pe \approx 10^4$) as demonstrated by numerous experiments (cf. Ref. [7], p. 166, slope of 45 degrees on Fig. 6.6 for $10^3 < Pe < 10^6$).

⁴³i.e. within the water conducting zone perpendicular to advective flow direction and to the dipole plane.

process). In this direction a constant nuclide concentration is assumed instead, representing an “equilibrium” which is reached fast compared to transport in flow direction.

7. The symmetry of model geometry allows the representation of the different water conducting and porous rock zones by a single pair of zones. The water conducting and the porous rock zone is characterised by one single set of transport parameters, each.
8. Individual sorption parameters can be used for the water conducting and the porous rock zone. Surfaces in the porous rock zones are much larger than surfaces of water conducting zones, such that bulk sorption usually is dominant. For systems with strongly sorbing surface coating, however, discrimination of surface sorption and bulk sorption might be important.
9. The radioactive decay of tracer nuclides is included in the model. In the case of linear sorption, as the applications described in chapters 4 and 5, it can be omitted by comparing the calculations to decay corrected experimental results. In the case of non-linear sorption, however, radioactive decay has to be treated explicitly by the model. A non-linear calculation for a mixture of decaying radiotracer and a non-decaying carrier cannot be performed with the present code.
10. Isotopic exchange affecting non-linear sorbing radiotracers (especially without carriers) at low concentrations (not much higher than the natural background) is neglected. The upper limit of the consequences of isotopic exchange, however, can be estimated (cf. comments to Eqs. (22)).
11. According to the requirements of the experiments it is not necessary to consider radioactive chains (also possible with the present code).
12. Infill material in the water conducting zone is not included explicitly in the model but can be taken into account by redefining the transport parameters accordingly (cf. section 3.2.4).

The following notation (omitting the stream tube index k) is used:

1. In the water conducting zone (index f)

z [m]	:	Coordinate along streamline
$C_f(z,t)$ [mol/m ³]	:	Concentration of tracer in the flowing water
$C_{fB}(t)$ [mol/m ³]	:	Tracer outflow concentration at the down stream boundary
$S_f(z,t)$ [mol/m ²]	:	Concentration of tracer on the sorbing surfaces
$j_f(z,t)$ [mol/(m ² s)]	:	Tracer flux (along the z -axis)
$R_f(C_f)$ [-]	:	Retardation function (for linear sorption retardation factor)
$\tilde{R}_f(C_f)$ [-]	:	Source correction function ⁴⁴
K_a [m]	:	Area specific sorption coefficient (distribution coefficient)
$A_f \left[\frac{\text{mol/m}^2}{(\text{mol/m}^3)^{N_f}} \right]$:	Amplitude of the Freundlich isotherm
N_f [-]	:	Exponent of the Freundlich isotherm
$C_o(t)$ [mol/m ³]	:	Injection concentration distribution
\bar{v} [m/s]	:	Water velocity
$j_o(t)$ [mol/(m ² s)]	:	Injection flux
a_L [m]	:	Longitudinal dispersion length (dispersivity)
b [m]	:	Half-width of the water conducting zone
n [-]	:	Number of water conducting zones
M_0 [mol]	:	Total mass injected into the flow field

2. Describing possible infill material in the water conducting zone (index I ; cf. section 3.2.4)

$S_{f,I}(z,t)$ [mol/kg]	:	Concentration of tracer sorbed on the infill
$K_{d,I}$ [m ³ /kg]	:	Mass specific sorption coefficient (distribution coefficient)
$A_{f,I} \left[\frac{\text{mol/kg}}{(\text{mol/m}^3)^{N_f}} \right]$:	Amplitude of the Freundlich isotherm
$N_{f,I}$ [-]	:	Exponent of the Freundlich isotherm
ϵ_I [-]	:	Porosity of the water conducting zone
$\tilde{\rho}_I$ [kg/m ³]	:	Bulk density of the water conducting zone

⁴⁴In our application multiplying the radioactive decay term.

3. In the porous rock zone (index p)

x [m]	: Coordinate into porous rock zone
d [m]	: Depth of the zone (up to the symmetry plane)
$C_p(x, z, t)$ [mol/m ³]	: Concentration of tracer in the pore water
$S_p(x, z, t)$ [mol/kg]	: Concentration of tracer sorbed on the pore walls
$j_p(x, z, t)$ [mol/(m ² s)]	: Tracer flux (along the x-axis)
$R_p(C_p)$ [-]	: Retardation function (for linear sorption retardation factor)
$\tilde{R}_p(C_p)$ [-]	: Source correction function ⁴⁵
K_d [m ³ /kg]	: Mass specific sorption coefficient (distribution coefficient)
A_p [$\frac{\text{mol/kg}}{(\text{mol/m}^3)^{N_p}}$]	: Amplitude of the Freundlich isotherm
N_p [-]	: Exponent of the Freundlich isotherm
ϵ_p [-]	: Porosity
D_p [m ² /s]	: Pore diffusion coefficient
$\tilde{\rho}_p$ [m ³ /kg]	: Bulk density $(1-\epsilon_p)\rho_p$
ρ_p [m ³ /kg]	: Solid phase density

4. General

L [m]	: Length of stream tube
B [m]	: Width of stream tube
λ [s ⁻¹]	: Decay constant
<i>nat</i>	: Index indicating natural background concentrations
<i>tot</i>	: Index indicating cumulative concentrations of natural background and tracer

5. For the analytical expressions of matrix diffusion (cf. section 3.2.5)

$\bar{t}(z)$ [s]	: Tracer advection time
$\tau_o(z)$ [s]	: Delay parameter
$C_{fm}(z)$ [mol/m ³]	: Peak height of the breakthrough curve
$t_m(z)$ [s]	: Peak position of the breakthrough curve
$s(z)$ [s]	: $(1/\sqrt{e})$ -width of the breakthrough curve
$\delta(t)$ [1/s]	: Dirac delta function
$t_p(x)$ [s]	: Penetration time
$\{x_p(t)-b\}$ [m]	: Penetration depth

⁴⁵In our application multiplying the radioactive decay term.

The mass balance in the water conducting zone can be written as

$$\frac{\partial C_f(z, t)}{\partial t} = \frac{1}{R_f(C_f)} [A_A + A_B + A_C + A_D] \quad , \quad (18a)$$

$$A_A = -\bar{v} \cdot \frac{\partial C_f(z, t)}{\partial z} \quad (\text{advection}) \quad ,$$

$$A_B = a_L \bar{v} \cdot \frac{\partial^2 C_f(z, t)}{\partial z^2} \quad (\text{dispersion}) \quad ,$$

$$A_C = \frac{\epsilon_p}{b} D_p \cdot \frac{\partial C_p(x, z, t)}{\partial x} \Big|_{x=b} \quad (\text{diffusion into the porous rock zone}) \quad ,$$

$$A_D = -\lambda \tilde{R}_f(C_f) \cdot C_f(z, t) \quad (\text{radioactive decay}) \quad ,$$

with the boundary conditions (BC)

$$\alpha_1 C_f(z=0, t) + \beta_1 \frac{\partial C_f(z, t)}{\partial z} \Big|_{z=0} = \gamma_1 C_0(t) \quad , \quad (18b)$$

$$\alpha_2 C_f(z=L, t) + \beta_2 \frac{\partial C_f(z, t)}{\partial z} \Big|_{z=L} = \gamma_2 \quad , \quad (18c)$$

using the parameters⁴⁶

$$\begin{aligned} \alpha_1 = 1 \quad , \quad \beta_1 = -a_L \quad , \quad \gamma_1 = 1 \quad & (\text{flux BC at the inlet}) \quad , \\ \alpha_2 = 0 \quad , \quad \beta_2 = 1 \quad , \quad \gamma_2 = 0 \quad & (\text{zero gradient BC at the outlet}) \quad , \end{aligned}$$

and the initial condition

$$C_f(z, t=0) = 0 \quad ; \quad 0 < z < L \quad . \quad (18d)$$

⁴⁶Injection flux = $j_0(t) = \bar{v} \cdot C_0(t)$. A flux BC is used at the inlet to conserve the injected mass. A concentration BC would in general imply an imprecisely defined source (due to the dispersive flux). The injection distribution $C_0(t)$ has to be normalized according to Eq. (17b). The zero gradient BC at the outlet is consistent with the transition to a non-dispersive (non-diffusive) medium.

The flux (along the z -axis) is given by:

$$j_f(z, t) = \bar{v} \cdot C_f(z, t) - a_L \bar{v} \cdot \frac{\partial C_f(z, t)}{\partial z} , \quad (18e)$$

and the outflow concentration at the down stream boundary⁴⁷

$$C_{fB}(t) = \frac{j_f(z = L, t)}{\bar{v}} . \quad (18f)$$

The mass balance in the stagnant water of the porous rock zone can be formulated as

$$\frac{\partial C_p(x, z, t)}{\partial t} = \frac{1}{R_p(C_p)} [A_E + A_F] , \quad (19a)$$

$$A_E = D_p \cdot \frac{\partial^2 C_p(x, z, t)}{\partial x^2} \quad (\text{diffusion}) ,$$

$$A_F = -\lambda \tilde{R}_p(C_p) \cdot C_p(x, z, t) \quad (\text{radioactive decay}) ,$$

with the boundary conditions⁴⁸

$$C_p(x = b, z, t) = C_f(z, t) ; \quad 0 < z < L , \quad (19b)$$

$$\frac{\partial C_p(x, z, t)}{\partial x} \Big|_{x=b+d} = 0 ; \quad 0 < z < L , \quad (19c)$$

and the initial condition

$$C_p(x, z, t = 0) = 0 ; \quad b < x < (b + d) , \quad 0 < z < L . \quad (19d)$$

⁴⁷The outflow concentration $C_{fB}(t)$ is introduced as the (undiluted) concentration outside the fracture being consistent with the mass balance (independent of the BC applied at the outlet). For the special cases of a zero gradient BC or of a non-dispersive flow, $C_{fB}(t) = C_f(z=L, t)$.

⁴⁸The concentration boundary condition (19b) is justified by assumption 6. The zero flux boundary condition (19c) corresponds to the symmetry of the model (cf. Fig. 6).

The flux (along the x -axis) is given by

$$j_p(x, z, t) = -D_p \cdot \frac{\partial C_p(x, z, t)}{\partial x} . \quad (19e)$$

The retardation function $R(C)$ and the source correction function $\tilde{R}(C)$ used in the mass balance Eqs. (18a) and (19a) take into account nuclide sorption, and are defined as ⁴⁹

$$R_f(C_f) = 1 + \frac{1}{b} \cdot \frac{dS_f(C_f)}{dC_f} , \quad (20a)$$

$$\tilde{R}_f(C_f) = 1 + \frac{1}{b} \cdot \frac{S_f(C_f)}{C_f} , \quad (20b)$$

$$R_p(C_p) = 1 + \frac{\tilde{\rho}_p}{\epsilon_p} \cdot \frac{dS_p(C_p)}{dC_p} , \quad (20c)$$

$$\tilde{R}_p(C_p) = 1 + \frac{\tilde{\rho}_p}{\epsilon_p} \cdot \frac{S_p(C_p)}{C_p} . \quad (20d)$$

For linear sorption isotherms the retardation and the source correction functions are reduced to constants:

$$S_f(z, t) = K_a C_f(z, t) \longrightarrow R_f \equiv \tilde{R}_f = 1 + \frac{1}{b} \cdot K_a , \quad (21a)$$

$$S_p(x, z, t) = K_d C_p(x, z, t) \longrightarrow R_p \equiv \tilde{R}_p = 1 + \frac{\tilde{\rho}_p}{\epsilon_p} \cdot K_d . \quad (21b)$$

⁴⁹ $1/b$ is the surface to volume ratio of the water conducting zone. This is a good approximation of the sorbing surface to volume ratio required in Eqs. (20a) and (20b). It could be improved by using $(1-\epsilon_p)/b$, instead.

For non-linear sorption, Freundlich isotherms are applied⁵⁰:

$$S_{tot}(C_{tot}) = A \cdot C_{tot}^N \quad , \quad (22a)$$

$$S_{nat}(C_{nat}) = A \cdot C_{nat}^N \quad , \quad (22b)$$

$$C_{tot} = C_{nat} + C \quad , \quad (22c)$$

$$S_{tot} = S_{nat} + S \quad . \quad (22d)$$

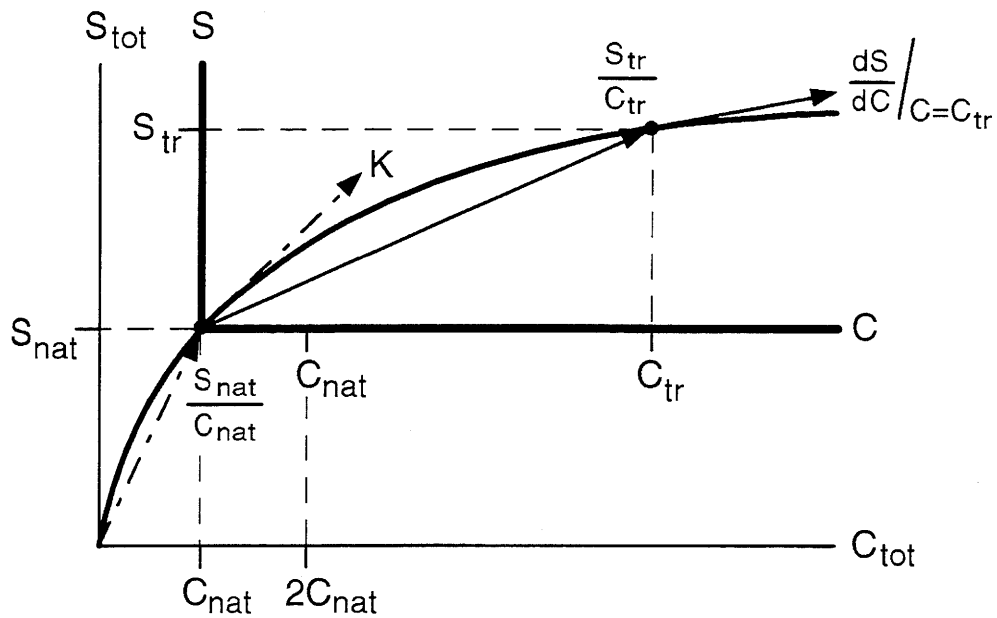


Figure 7 The Freundlich sorption isotherm describing the relation between the tracer concentrations S on the rock and C in the water. In the case of non-linear sorption, it can be important to distinguish strictly between the tracer concentrations (S and C) and the total nuclide concentrations (S_{tot} and C_{tot}).

⁵⁰Indices f, p, a and d are omitted because the same formal relationships apply for the water conducting zone as well as for the porous rock zone.

The following relations for the tracer nuclides (including possible carriers if radiotracers are considered) can be derived from Eqs. (22) and applied to Eqs. (20):

$$S(C) = A \cdot C_{nat}^N \left[\left(1 + \frac{C}{C_{nat}} \right)^N - 1 \right] , \quad (22e)$$

$$\frac{dS(C)}{dC} = K \cdot \left(1 + \frac{C}{C_{nat}} \right)^{N-1} , \quad (22f)$$

$$\frac{dS(C)}{dC} = K \cdot \left[1 - (1-N) \left(\frac{C}{C_{nat}} \right) + o \left\{ \left(\frac{C}{C_{nat}} \right)^2 \right\} \right] \approx K \quad \text{for } C \ll C_{nat} , \quad (22g)$$

$$\frac{S(C)}{C} = K \cdot \frac{\left[\left(1 + \frac{C}{C_{nat}} \right)^N - 1 \right]}{N \cdot \left(\frac{C}{C_{nat}} \right)} , \quad (22h)$$

$$\frac{S(C)}{C} = K \cdot \left[1 - \frac{(1-N)}{2} \left(\frac{C}{C_{nat}} \right) + o \left\{ \left(\frac{C}{C_{nat}} \right)^2 \right\} \right] \approx K \quad \text{for } C \ll C_{nat} , \quad (22i)$$

$$K = A \cdot N \cdot C_{nat}^{N-1} . \quad (22k)$$

Eqs. (22e) to (22k) can be interpreted as a shift in scale for the tracer nuclides as shown in Fig. 7. dS/dC is represented by the tangent and S/C by the secant line. For $C \gg C_{nat}$ the sorbed tracer concentration almost corresponds to the usually applied simple power law. For $C \approx C_{nat}$, the simple power law is no longer valid⁵¹. For $C \ll C_{nat}$ sorption according to the Freundlich isotherm (!) is linear ($dS/dC = S/C = K$). Isotopic exchange affecting non-linear sorbing radiotracers (especially without carriers) is not included in the model. This is a good approximation for $C \gg C_{nat}$. For $C \approx C_{nat}$, further consideration could improve the calculation. The largest influence of isotopic exchange, occurring at $C \ll C_{nat}$ for radiotracers without carriers, would increase the linear Freundlich sorption coefficient K to $S_{nat}/C_{nat} = K/N$ (cf. Eq. (22b) and (22k)). In this case, the consequence of isotopic exchange on the breakthrough curve can directly be calculated.

The **numerical calculations** are performed by the computer code RANCHMDNL (cf. Ref. [6]). From the two coupled partial differential equations describing mass balance, a

⁵¹Neglecting this fact can lead to occasionally observed misinterpretations of the Freundlich isotherm, no longer being linear on a log-log scale for that tracer range.

set of time-dependent ordinary differential equations are derived by the Lagrange interpolation technique. Time integration is performed by Gear's variable order predictor-corrector method.

3.2.3 Effective Surface Sorption Approximation

If matrix diffusion up to the total depth of the porous rock zone is sufficiently fast⁵² with respect to advection in the water conducting zone, the concentration in the pore water of the porous rock zone can be approximated by the corresponding concentration in the water conducting zone ($C_p(x, z, t) \approx C_f(z, t)$). In this case surface sorption in the water conducting zone, matrix diffusion and bulk sorption in the porous rock zone can be combined to an effective surface sorption in the water conducting zone. The corresponding effective retardation and decay correction functions replacing Eq. (20a) and (20b) have the following form⁵³:

$$R_{f,eff} = 1 + \frac{1}{b} [A_G + A_H + A_I] \quad , \quad (23a)$$

$$A_G = \frac{dS_f(C_f)}{dC_f} \quad (\text{surface sorption in the water conducting zone}) \quad ,$$

$$A_H = \epsilon_p d \quad (\text{diffusion into the porous rock zone}) \quad ,$$

$$A_I = \tilde{\rho}_p d \cdot \frac{dS_p(C_f)}{dC_f} \quad (\text{bulk sorption in the porous rock zone}) \quad ,$$

$$\tilde{R}_{f,eff} = 1 + \frac{1}{b} [\tilde{A}_G + A_H + \tilde{A}_I] \quad , \quad (23b)$$

$$\tilde{A}_G = \frac{S_f(C_f)}{C_f} \quad (\text{surface sorption in the water conducting zone}) \quad ,$$

⁵²The necessary condition can roughly be estimated by the relation:

$t_p(2d) = d^2 \cdot R_p(C_f(z, t))/D_p \gg s(z)$ where $s(z)$ is the $(1/\sqrt{e})$ -width of the time dependent tracer pulse distribution passing the point z (cf. Eq. (31e)).

⁵³The physical/geometrical meaning of the coefficients are: i) $1/b =$ surface to volume ratio of the water-conducting zone, ii) $\epsilon_p d/b =$ pore water volume to flowing water volume ratio, iii) $\tilde{\rho}_p d/b =$ porous rock mass to flowing water volume ratio.

$$\tilde{A}_I = \tilde{\rho}_p d \cdot \frac{S_p(C_f)}{C_f} \quad (\text{bulk sorption in the porous rock zone}) \quad .$$

For linear sorption, the expressions in the square brackets of Eqs. (23a) and (23b) can be combined into one single area specific effective sorption coefficient. For non-linear sorption, however, it is necessary to have equal Freundlich exponents for the water-conducting and the porous rock zone as well as to neglect the diffusion term to simplify the square brackets into expressions for one single area specific effective Freundlich sorption relation.

3.2.4 Infill of the Water Conducting Zone

A possible infill of the water conducting zone does not change the mass balance equation (18) for that zone⁵⁴. The surface sorption of the water conducting zone, however, has to be replaced by the bulk sorption of the infill, leading to a new definition of the retardation and source correction functions:

$$R_f(C_f) = 1 + \frac{\tilde{\rho}_I}{\epsilon_I} \cdot \frac{dS_{f,I}(C_f)}{dC_f} \quad , \quad (24a)$$

$$\tilde{R}_f(C_f) = 1 + \frac{\tilde{\rho}_I}{\epsilon_I} \cdot \frac{S_{f,I}(C_f)}{C_f} \quad , \quad (24b)$$

$$S_{f,I}(C_f) = A_{f,I} \cdot C_{nat}^{N_{f,I}} \left[\left(1 + \frac{C_f}{C_{nat}} \right)^{N_{f,I}} - 1 \right] \quad . \quad (24c)$$

For linear sorption we obtain

$$R_f \equiv \tilde{R}_f = 1 + \frac{\tilde{\rho}_I}{\epsilon_I} \cdot K_{d,I} \quad . \quad (24d)$$

In the numerical calculations, Eqs. (24a) to (24d) are taken into account by redefining A_f and N_f used in the Eqs. (22e), (20a) and (20b), as well as K_a used in Eq. (21a):

⁵⁴The reason that the expression Eq. (18a; A_C) for the diffusion into the porous rock zone is not changed by the infill is, that the volume of the flowing water, as well as the interface surface between flowing and stagnant water, are reduced by the same factor when taking an infill into account.

$$A_f = b \cdot \frac{\tilde{\rho}_I}{\epsilon_I} \cdot A_{f,I} \quad , \quad (24e)$$

$$N_f = N_{f,I} \quad , \quad (24f)$$

$$K_a = b \cdot \frac{\tilde{\rho}_I}{\epsilon_I} \cdot K_{d,I} \quad . \quad (24g)$$

The boundary condition, Eq. (19b), is formally unchanged if assumption 6 of section 3.2.2 remains correct.

The effect of the infill on the transport parameters can be described redefining

$$b = \frac{(\epsilon a)}{2n} \quad , \quad (24h)$$

$$d = \frac{a - \frac{(\epsilon a)}{\epsilon_I}}{2n} \quad , \quad (24i)$$

$$\bar{v} \sim \frac{1}{(\epsilon a)} \quad , \text{ no effect}^{55} \quad , \quad (24j)$$

$$a_L \quad \text{effect of infill implicitly included}^{56} \quad . \quad (24k)$$

The main influence of infill material, not changing flow width (ϵa) and corresponding water velocity \bar{v} , is an enlarged half-width b and, therefore, a reduced matrix diffusion effect. For sorbing nuclides, it is coupled with a correspondingly larger retardation effect (R_f and \tilde{R}_f).

3.2.5 Influence of Matrix Diffusion

To improve understanding of the diffusion process into the porous rock zone, analytical expressions for mass balance and the breakthrough curve are helpful. They are derived in Ref. ([16], App. 3) for a square pulse injection and simplifying assumptions, and discussed

⁵⁵The infill has no effect since (ϵa) is defined with respect the flowing water.

⁵⁶ a_L is only slightly affected since dispersion from the fracture system is on a larger scale than from the infill.

in a broader context in Ref. [17]. They are presented, here, for the limit of a Dirac delta injection.

In addition to those in section 3.2.2, the following assumptions were used:

1. No dispersion ($a_L = 0$).
2. 1D-flow field for one single stream tube (Fig. 5; $Q_k = Q_i$, $L_k = L$, $B_k = B$).
3. Infinite length of the stream tube ($0 \leq z \leq L = \infty$)⁵⁷.
4. Semi-infinite porous rock zones ($d = \infty$).
5. No radioactive decay.
6. Linear sorption.
7. Dirac delta injection boundary condition at $z = 0$.

The equations of chapter 3.2.2 can be simplified as follows:

The mass balance in the water conducting zone is expressed as

$$\frac{\partial C_f(z, t)}{\partial t} = \frac{1}{R_f} \left[-\bar{v} \frac{\partial C_f(z, t)}{\partial z} + \frac{\epsilon_p}{b} D_p \frac{\partial C_p(x, z, t)}{\partial x} \Big|_{x=b} \right] , \quad (25a)$$

with the boundary conditions⁵⁸

$$C_f(z = 0, t) = C_o(t) = \frac{M_0}{Q_i} \delta(t) , \quad (25b)$$

$$Q_i = (\epsilon a) B \bar{v} \quad \text{with} \quad (\epsilon a) = n \cdot 2b , \quad (25c)$$

$$C_f(z = \infty, t) = 0 , \quad (25d)$$

⁵⁷The breakthrough curve is not influenced by a boundary condition at the observation point z .

⁵⁸The concentration BC's are identical with flux BC's since dispersion is neglected.

and the initial condition

$$C_f(z, t = 0) = 0 \quad , \quad z > 0 \quad . \quad (25e)$$

The flux (along the z -axis) is given by

$$j_f(z, t) = \bar{v} \cdot C_f(z, t) \quad , \quad (25f)$$

and the retardation factor R_f given by Eq. (21a).

The mass balance in the stagnant water of the porous rock zone is formulated as

$$\frac{\partial C_p(x, z, t)}{\partial t} = \frac{1}{R_p} D_p \cdot \frac{\partial^2 C_p(x, z, t)}{\partial x^2} \quad , \quad (26a)$$

with the boundary conditions

$$C_p(x = b, z, t) = C_f(z, t) \quad ; \quad z > 0 \quad , \quad (26b)$$

$$C_p(x = \infty, z, t) = 0 \quad ; \quad z > 0 \quad , \quad (26c)$$

and the initial condition

$$C_p(x, z, t = 0) = 0 \quad ; \quad b < x < (b + d) \quad , \quad z > 0 \quad . \quad (26d)$$

The flux (along the x -axis) is given by

$$j_p(x, z, t) = - D_p \frac{\partial C_p(x, z, t)}{\partial x} \quad , \quad (26e)$$

and the retardation factor R_p given by Eq. (21b).

Eqs. (25) and (26) have an analytical solution which is presented here without derivation.

The tracer concentration in the water conducting zone is calculated as

$$C_f(z, t) = 0 \quad ; \quad t < \bar{t}(z) \quad , \quad (27a)$$

$$C_f(z, t) = \frac{M_0}{Q_i} \cdot f_f(z, t) \quad ; \quad t \geq \bar{t}(z) \quad , \quad (27b)$$

$$f_f(z, t) = \frac{1}{\sqrt{\pi}} \cdot \sqrt{\frac{\tau_0(z)}{(t - \bar{t}(z))^3}} \cdot \exp\left[-\frac{\tau_0(z)}{t - \bar{t}(z)}\right] \quad , \quad (27c)$$

$$\int_0^{\infty} f_f(z, t) dt = 1 \quad , \quad (27d)$$

$$\bar{t}(z) = \frac{z}{\left(\frac{v}{R_f}\right)} \quad , \quad (27e)$$

$$\tau_0(z) = \left(\frac{\epsilon_p}{b}\right)^2 \cdot \frac{D_p R_p}{4} \cdot \left(\frac{z}{v}\right)^2 \quad . \quad (27f)$$

The breakthrough curve (concentration distribution in time) exhibits the following expressions for peak height $C_{fm}(z)$, peak position $t_m(z)$ and peak width $s(z)$ ⁵⁹:

$$C_{fm}(z) = \left[\frac{1}{\sqrt{\pi}} \cdot \left(\frac{3}{2}\right)^{\frac{3}{2}} \cdot \exp\left(-\frac{3}{2}\right) \right] \cdot \frac{M_0/Q_i}{\tau_0(z)} \approx 0.23 \frac{M_0/Q_i}{\tau_0(z)} \quad , \quad (28a)$$

$$t_m(z) = \bar{t}(z) + \frac{2}{3}\tau_0(z) \quad , \quad (28b)$$

$$s(z) \approx 1.4 \cdot \tau_0(z) \quad , \quad (28c)$$

and for the behaviour at large times⁶⁰

$$C_f(z, t) = \frac{M_0 \sqrt{\tau_0(z)}}{Q_i \sqrt{\pi}} \cdot t^{-\frac{3}{2}} \left[1 + o\left\{\frac{t_m(z)}{t}\right\} \right] \quad \text{for } t \gg t_m(z) \quad . \quad (29)$$

⁵⁹Eqs. (28a) and (28b) are derived from Eqs. (27a) to (27c) applying $\partial C_f / \partial t = 0$ for $t = t_m$. The width $s(z)$ corresponds to the height $C_{fm}(z)/\sqrt{e}$. Eq. (28c) is derived in Appendix 1.

⁶⁰Obtained by expansion of Eq. (27c) ($t \gg t_m$ implies $t \gg \bar{t}$ as well as $t \gg \tau_0$).

At the limit of no matrix diffusion the advected injection pulse is obtained:

$$\lim_{D_p \rightarrow 0} C_f(z, t) = \frac{M_0}{Q_i} \cdot \delta(t - \bar{t}(z)) \quad . \quad (30)$$

The tracer concentration in the stagnant water of the porous rock zone is calculated as⁶¹

$$C_p(x, z, t) = 0 \quad ; \quad t < \bar{t}(z) \quad , \quad (31a)$$

$$C_p(x, z, t) = \frac{M_0}{Q_i} \cdot f_p(x, z, t) \quad ; \quad t \geq \bar{t}(z) \quad , \quad (31b)$$

$$f_p(x, z, t) = A_1(x, z, t) \cdot \exp \left[- \frac{(\sqrt{\tau_0(z)} + \sqrt{t_p(x)})^2}{t - \bar{t}(z)} \right] \quad , \quad (31c)$$

$$A_1(x, z, t) = \frac{1}{\sqrt{\pi}} \cdot \frac{\sqrt{\tau_0(z)} + \sqrt{t_p(x)}}{\sqrt{(t - \bar{t}(z))^3}} \quad , \quad (31d)$$

using the penetration time⁶²

$$t_p(x) = \frac{1}{4} \cdot \frac{R_p}{D_p} \cdot (x - b)^2 \quad . \quad (31e)$$

The corresponding flux for $t \geq \bar{t}(z)$ is deduced from Eq. (31) according to Eq. (26e):

$$j_p(x, z, t) = A_2(z, t) \cdot \exp \left[- \frac{(\sqrt{\tau_0(z)} + \sqrt{t_p(x)})^2}{t - \bar{t}(z)} \right] \quad , \quad (31f)$$

⁶¹ $C_p(x, z, t)$ can formally be deduced from $C_f(z, t)$ by replacing $\sqrt{\tau_0(z)}$ with $(\sqrt{\tau_0(z)} + \sqrt{t_p(x)})$, (cf. Eqs. (27) and (31)). The same procedure could be applied to deduce from Eq. (28) the maximum peak height and position at a specific point of the porous rock zone.

⁶²The parameter $t_p(x)$ is defined consistently to the penetration depth $\{x_p(t) - b\} = 2 \cdot \sqrt{\frac{D_p}{R_p} t}$ of the diffusion process and therefore called penetration time. The penetration depth is the time dependent distance not exceeded by 87% of the nuclides diffusing from a constant concentration boundary into the half space. Correspondingly, the penetration time is the time at which 87% of the diffusing nuclides have not yet passed a fixed distance x .

$$A_2(z, t) = \frac{M_0}{Q_i} \cdot \frac{\sqrt{R_p D_p}}{2} \cdot \frac{1}{\sqrt{(t - \bar{t}(z))^3}} \left[\frac{2(\sqrt{\tau_0(z)} + \sqrt{t_p(x)})^2}{t - \bar{t}(z)} - 1 \right] . \quad (31g)$$

The breakthrough curve shows the following behaviour:

1. The **general shape of the breakthrough curve** (Fig. 8, upper part) is strongly dependent on the parameter values. For the values chosen, it shows an increase which is fairly fast as well as a slow decrease and a long tailing. The rising part is determined by advection and diffusion out into the porous rock zone flattening the front during transport. The time of first arrival corresponds to the advection time which is a consequence of neglecting dispersion. Decrease and tailing are determined by advection and diffusion back into the water conducting zone. Since diffusion is much slower than advection it produces a slow decrease and a long tailing. The longer the travelling distance the more nuclides diffuse out of the pulse and the deformation of the pulse (flattening of the front edge and increasing of tail amplitude) becomes stronger.
2. The **spatial concentration distribution**, at the advection time, up to the observation point $z = z_o$ (Fig. 8, lower part) is positioned completely before z_o since dispersion is neglected. It is much higher and has a completely different shape than the breakthrough curve. This is not the case if only advection and dispersion are considered (cf. Fig. A2.1 of App. 2).
3. The **maximum of the breakthrough curve** can be described by simple expressions with $\tau_o(z)$ as the key parameter (cf. Eq. (28)).

The maximum is governed by the following proportionalities⁶³:

- i) Peak height: $C_{m,f} \sim M_0/Q_i, 1/(\epsilon_p/b)^2, 1/(z/\bar{v})^2, 1/(D_p R_p)$
- ii) Delay by matrix diffusion: $(t_m - \bar{t}) \sim (\epsilon_p/b)^2, (z/\bar{v})^2, D_p R_p$

4. **Surface sorption in the water conducting zone** produces only a shift of the breakthrough curve to larger times since surface sorption (R_f) enlarges \bar{t} and the breakthrough curve is dependent on $(t - \bar{t})$, (cf. Eqs. (27e) and (27c)). Delay by matrix diffusion is independent of surface sorption⁶⁴ as well as the peak height reduction (cf. Eq. (28)).

⁶³In discussing the proportionalities, one should keep in mind that \bar{v} can be correlated to Q_i or b (assuming $B = \text{const.}$, cf. Eq. (25c)).

⁶⁴From a microscopic point of view we can say that matrix diffusion affects only those nuclides which are passing the pore surfaces.

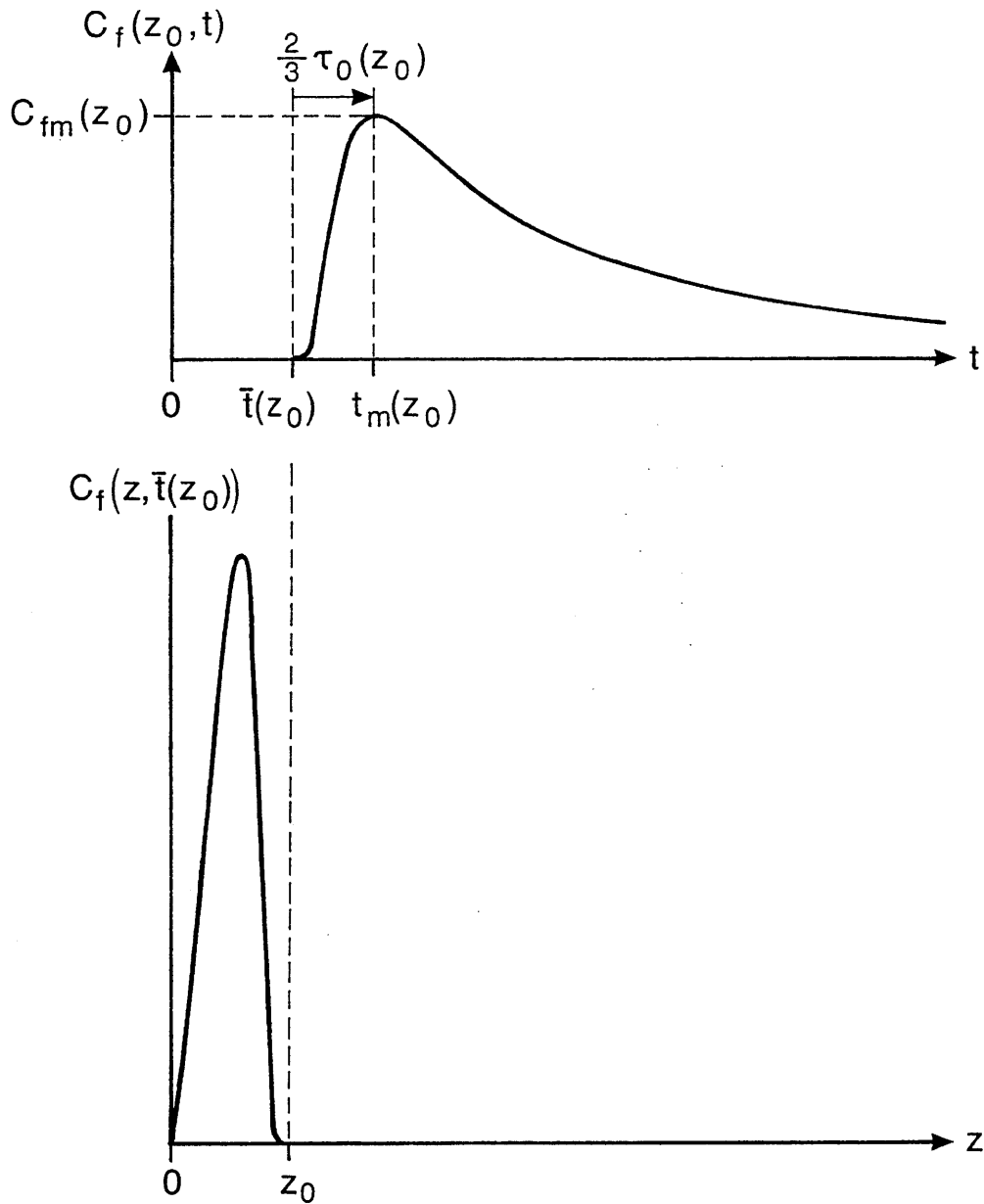


Figure 8 Concentration distributions for nuclide transport by advection and matrix diffusion only. Upper part: The breakthrough curve at the observation point $z = z_0$ shows the characteristic delay of the peak beyond the advection time $\bar{t}(z_0)$ and a long tailing. Lower part: The spatial distribution at $t = \bar{t}(z_0)$ has a completely different shape and is positioned before z_0 (note the difference to Fig. A2.1 in App. 2).

5. **Bulk sorption in the porous rock zone** reduces the peak height, and enlarges the delay time as well as the width of the breakthrough curve, but does not affect the advection time ($C_{f,m} \sim 1/R_p$, $(t_m - \bar{t}) \sim R_p$, $s(z) \sim R_p$); (cf. Eqs. (27f) and (28)). Qualitatively, this is due to an enlarged flux into the porous rock zone⁶⁵.

6. The **tail concentration of the breakthrough curve** at large times ($t \gg t_m$) is decreasing with $t^{-3/2}$ due to the backflow from the diffusion process in the porous rock zone (cf. Eq. (29) as well as (31f) and (31g)). The tail amplitude is proportional to $\sqrt{\tau_0}$, whereas the peak height is to $1/\tau_0$. This reflects a fast tracer flow into the porous rock zone during peak transit and a slow tracer backflow at large times. The detailed proportionalities of the tail amplitude are:

$$C_f(t \gg t_m) \sim M_o/Q_i, \epsilon_p/b, z/v, \sqrt{D_p R_p}.$$

7. The following **main differences to the single porosity model**⁶⁶ (described in App. 2) can be observed:

- Asymmetric form of the breakthrough curve with long tailing compared to a relatively small asymmetry (cf. Eqs. (27), Fig. 8, (upper part) and Eqs. (A2.3), Fig. A2.1, (upper part)).
- Different delay of the breakthrough peak position (cf. Eqs. (28b) and (A2.5c)).
 - i) Dual porosity : $t_m = \bar{t} + \frac{2}{3} \tau_0$
 - ii) Single porosity: $t_m \approx \bar{t}$
- Different parameter dependencies for peak height of breakthrough (cf. Eqs. (28a) and (A2.5a)):
 - i) Dual porosity : $C_{fm} \sim (1/\tau_0) \cdot (M_o/Q_i)$
 - ii) Single porosity: $C_{fm} \sim (1/\sigma) \cdot (M_o/\{(\epsilon a) B \cdot R_f\})$

In the dual porosity model the parameter sensitivity is stronger (τ_0 compared to σ) and inversly proportional to the injection rate (Q_i compared to $(\epsilon a) B \cdot R_f$).
- Tailing according to $t^{-3/2}$ compared to an exponential drop (cf. Eqs. (29) and (A2.3b)).
- Different parameter dependencies for width of breakthrough (cf. Eqs. (28c) and (A2.5e))

⁶⁵Slower nuclide propagation and therefore steeper gradients.

⁶⁶Note that in contrast to the analytical solution of the dual porosity model, the single porosity model includes dispersion!

- i) Dual porosity : $s \sim \tau_0$
- ii) Single porosity: $s \sim \sigma$
- The effect of bulk sorption (R_p) in the porous rock zone compared to single porosity sorption (R_f) shows differences and similarities (cf. Eq. (28) and (A2.5))⁶⁷:
 - i) Dual porosity : $C_{fm} \sim 1/R_p$
 $(t_m - \bar{t}) \sim R_p$!
 $s \sim R_p$
 - ii) Single porosity: $C_{fm} \sim 1/R_f$
 $t_m \sim R_f$
 $s \sim R_f$

Note especially the reduced influence of weak sorption on peak position in the dual porosity model.

- Different parameter dependence on travelling distance:
 - i) Dual porosity: $\tau_0 \sim z^2$ (matrix diffusion)
 - ii) Single porosity: $\sigma \sim \sqrt{z}$ (dispersion)

8. When using the analytical expressions as a **guide to understand breakthrough curve behaviour of the dipole experiments**, we have to take into account:

- The concentrations are based on a 1D-water flow. When making comparisons with results from the dipole experiments, the dilution factor $\beta = Q_w/Q_i$ has to be applied.
- The expressions are reasonable approximations if:
 - a) the influence of the dipole flow is small ($\beta \gg 1$), see also Appendix 8,
 - b) the width of the injection distribution is small compared to τ_0 ,
 - c) the effect of matrix diffusion is large compared to dispersion ($\tau_0 \gg \sigma/(\bar{v}/R_f)$),
 - d) the boundary of both the water conducting zone at $z = L$ and of the porous rock zone at $x = b+d$ have a negligible influence.

⁶⁷The dual porosity proportionalities are valid only if sorption is strong enough to justify neglecting dispersion and the influence of the injection distribution or if corresponding corrections are applied. Special care is therefore necessary in the comparison of a sorbing and a non-sorbing tracer.

4 Analysis of Experimental Breakthrough Curves

Various approaches have been applied for testing transport models with experimental data, especially field data [2]. The main problem is on two levels. First, the model concepts are uncertain. Ideally, the results from a whole set of different models should be compared (the models should clearly be as simple as possible, but not simpler). Such a comparison is outside the scope of the present work. We have chosen, based on available information, a simple dual porosity model and varied the model concept by neglecting certain processes, e.g. matrix diffusion. Second, the parameters are uncertain. We have compared parameter values extracted from the field experiments with data from independent experiments and with general knowledge from the literature. Ideally, one would like to determine model and data completely by the analysis of a first set of experiments and subsequently make predictions for fully independent new experiments. This was partially possible, only.

Our procedure in the analysis is as follows: First, parameters describing the experimental layout and a few parameters pertaining to the geological structure are fixed in advance. Second, nuclide independent parameters are calibrated with data from a non-sorbing tracer, uranine. Then, keeping these parameters fixed, nuclide dependent parameters are determined for uranine and, using new experimental data, also for the sorbing tracers sodium and strontium.

4.1 Experimental Conditions and Fixed Parameters

Experimental conditions: TEST 50 of the migration field experiments (cf. Ref. [4], sections 3.1 and 4.2.2) was selected for detailed analysis. In this experiment the conservative uranine and the reactive tracers were injected simultaneously into the flow field. The injection concentrations of ^{22}Na and ^{85}Sr (including the carriers) were small enough to sorb linearly. The flow field was determined by the following experimental conditions:

$$L_o = 4.9 \text{ m} \quad , \quad (32a)$$

$$Q_i = 9.3 \text{ ml/min} \quad , \quad (32b)$$

$$Q_w = 148.5 \text{ ml/min} \quad , \quad (32c)$$

$$\beta = 16.0 \quad . \quad (32d)$$

The large β , leading to a fairly uniform flow field, simplifies the analysis (at the expense of covering only a narrow region of the fracture). The influence of widening the flow field to $\beta = 3$ and 1.5 is discussed in App. 8. The errors of Q_i and Q_w , usually in the order of percent⁶⁸, are neglected with respect to the large uncertainties originating in model simplifications.

The injection flux boundary condition is determined from the down hole measurement of the concentration distribution (cf. Fig. 9). It shows a substantial delay, broadening, and shape deformation of the original 3 minute square pulse injected into the inlet tubing. An attempt

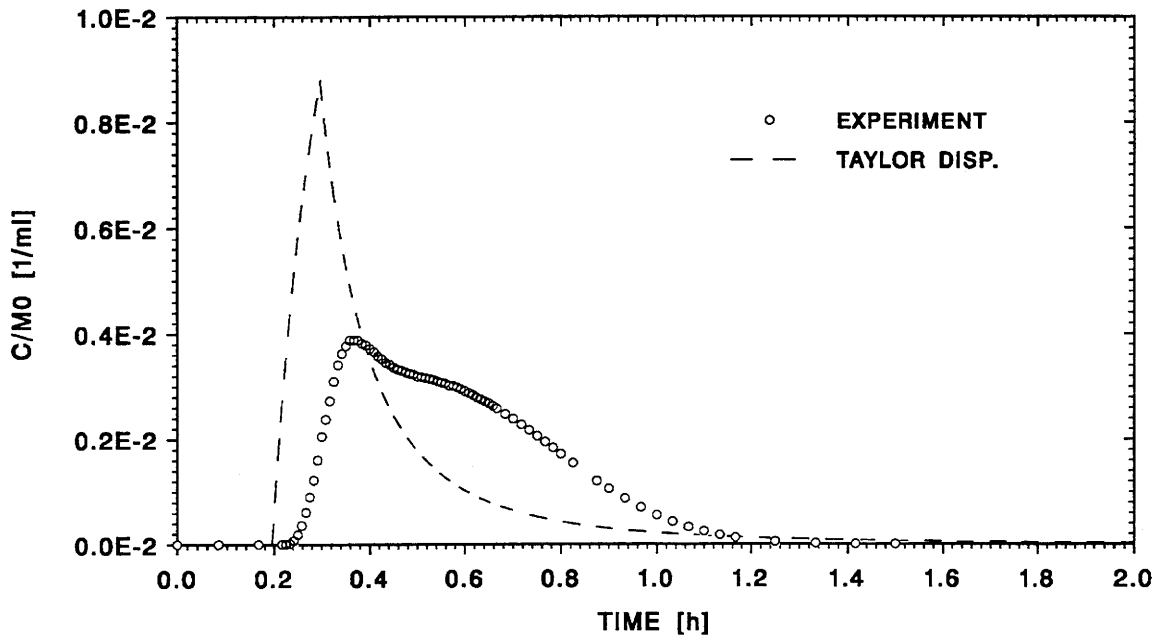


Figure 9 Down hole tracer injection distribution for the experiments in the 4.9 m dipole flow field. An attempt to estimate the effect of the inlet equipment by Taylor dispersion failed. For modelling breakthrough, the experimental curve is used.

⁶⁸It has to be mentioned, however, that due to a pumpe failure, Q_w was reduced by a factor 2 in the time interval $t=167$ h to 187 h (long after tracer injection was terminated). The response of the experimental breakthrough curves were increases up to 10% in that time interval (cf. [4], Fig. 32, particularly ⁸⁵Sr). For our applications, the experimental breakthrough concentrations of all three tracer nuclides were therefore omitted from $t=167$ h to $t=192$ h.

to simulate the injection equipment by calculating Taylor dispersion for a straight tube (neglecting molecular diffusion and the deviations from a straight tube) failed, emphasizing the necessity of the down-hole measurement.

Fixed Parameters: In order to restrict the number of fit parameters, the width a of the migration zone, the number n of the water conducting zones and the bulk density $\tilde{\rho}_p$ are fixed in advance. a , n and the corresponding uncertainties are guesses based on the results of a structural analysis (Ref. [10], p. 25). $\tilde{\rho}_p$ was determined earlier in geological investigations (Ref. [18], referenced in Ref. [5], p. 43) and the corresponding uncertainty estimated. To be consistent with the other parameters, the numerical values are assumed to be medians of log-normal distributions with uncertainties corresponding to one geometric standard deviation Σ^{69} .

$$a = (5_{-2.5}^{+5}) \cdot 10^{-2} \text{ m} ; \quad \Sigma(a) = 2 \quad , \quad (33a)$$

$$n = 4_{-1}^{+2} ; \quad \Sigma(n) = 1.5 \quad , \quad (33b)$$

$$\tilde{\rho}_p = (2670 \pm 200) \text{ kg/m}^3 ; \quad \Sigma(\tilde{\rho}_p) = 1.08 \quad . \quad (33c)$$

4.2 Calibration with the Conservative Tracer Uranine

4.2.1 Selection of Fit Parameters

According to mass balance and the restriction to linear sorption four independent parameters⁷⁰ can be adjusted to fit the model to the experimental breakthrough curve (cf. Eqs. (18) and (19)). The following parameters are chosen with the aim to separate as much as possible the individual influences onto the breakthrough curve and to facilitate physical understanding:

⁶⁹Compare App. 4, Eqs. (A4.1).

⁷⁰Note, however, that for breakthrough curves not being influenced by the outer boundary of the porous rock zone, only 3 parameters are independent.

(ϵa): **The flow width**; to fit mainly the peak position in time.

(ϵa) defines, consistent with the number n of the water conducting zones and the width a of the migration zone, the following parameters for the transport calculation:

$$\bar{v}_k \sim \frac{1}{(\epsilon a)} \quad (\text{cf. Eqs. (5), (12), (13a) and (14a)}) \quad , \quad (34a)$$

$$b = \frac{(\epsilon a)}{2n} \quad , \quad (34b)$$

$$d = \frac{a - (\epsilon a)}{2n} \quad . \quad (34c)$$

a_L : **Dispersion length**; to fit mainly peak height and width.

F_c : **An interface flux⁷¹ parameter**; to fit mainly tail amplitude⁷².

$$F_c = \epsilon_{pc} \cdot \sqrt{D_{pc}} \quad . \quad (34d)$$

B_c : **A tail end parameter**; to fit the tail end perturbation⁷³.

$$B_c = \frac{1}{\sqrt{D_{pc}}} \quad . \quad (34e)$$

Once determined with the conservative tracer, ϵa , and consequently \bar{v}_k , b and d are kept constant for all nuclides (calibration). For the other 3 fit parameters, a nuclide dependence cannot be excluded *a priori*.

⁷¹Interface flux = flux from the water conducting to the porous rock zone (and vice versa).

⁷² F_c is chosen as closely as possible to (App. 3, Eq. (A3.2b)), taking into account that b is fixed by the fit of (ϵa). The index c signifies extraction from the calibration experiment.

⁷³Tail end perturbation = the observed bump and drop at the end of the tail. B_c is chosen as closely as possible to (App. 3, Eq. (A3.3d)), taking into account that d is fixed by the fit of (ϵa). The choice of B_c instead of D_{pc} keeps the parameter in line with the corresponding parameter of the sorbing nuclides (cf. Eq. (39b)).

4.2.2 Results

Fitted Breakthrough Curve: The fit of the model to the experimental breakthrough curve for the conservative tracer uranine is depicted in Fig. 10. It is possible to reproduce the full range of the curve rather well. We especially emphasize the agreement in peak value and in the shape of the tail.

The comparison to a calculation without matrix diffusion (dashed line) shows the inadequacy of that model (and the futility to try a fit). Within our conceptual model matrix diffusion is absolutely necessary to represent the experiment. The question arises whether any mechanism other than matrix diffusion could produce such a tail. For times large compared to the peak position, the matrix diffusion mechanism causes a $t^{-3/2}$ dependency resulting from tracer back-flow into the water conducting zones. This is true as long as the outer boundary in the porous rock zone is not influencing matrix diffusion. However, as soon as the no-flow boundary in the porous rock zone influences tracer back-flow, an increase in the breakthrough concentration arises because of the restriction of further out-diffusion. For still later times, the breakthrough concentration decreases rapidly because of the limited volume of the porous rock zone. The tail of the experimental breakthrough curve, approaching first the analytical guide (not only in the $t^{-3/2}$ slope but also in the amplitude⁷⁴) and exhibiting the subsequent bump and drop, is a strong support for the dual porosity concept⁷⁵. From the geological structure analysis (Ref. [10], p. 25, Fig. 12) it is not clear-cut whether the flow within the porous fault gouge regions is homogeneously distributed or channelled. Modelling of the migration experiment gives here a clear evidence that the flow must be channelled. The deviation between model and experiment at the end of the tail indicates that a more detailed representation of the porous rock zone would be needed for a closer fit, e.g. different parameters within and outside the fault gouge. The linear time scale representation in Fig. 10 (lower part) is given in order to depict the comparison not only in relative but also in absolute units and in addition to put the deviations of the front edge into perspective. The characteristic data of the experimental breakthrough curve and the derivations of the fitted model values are given in Tab. 1. On the whole the comparison of experiment and model demonstrates the quality of the experiment and the ability of the model to describe the salient features of tracer transport.

⁷⁴The analytical guide [$C_f(t) / M_o$ for $t \gg t_m$] is calculated according to Eqs. (29) and (27f) taking into account dilution by the factor β .

⁷⁵In general, the bump at the end of the tail is only seen in those special cases when the outer no-flow boundary in the porous rock zone is efficacious and its effects are not smeared out during transport along the migration path.

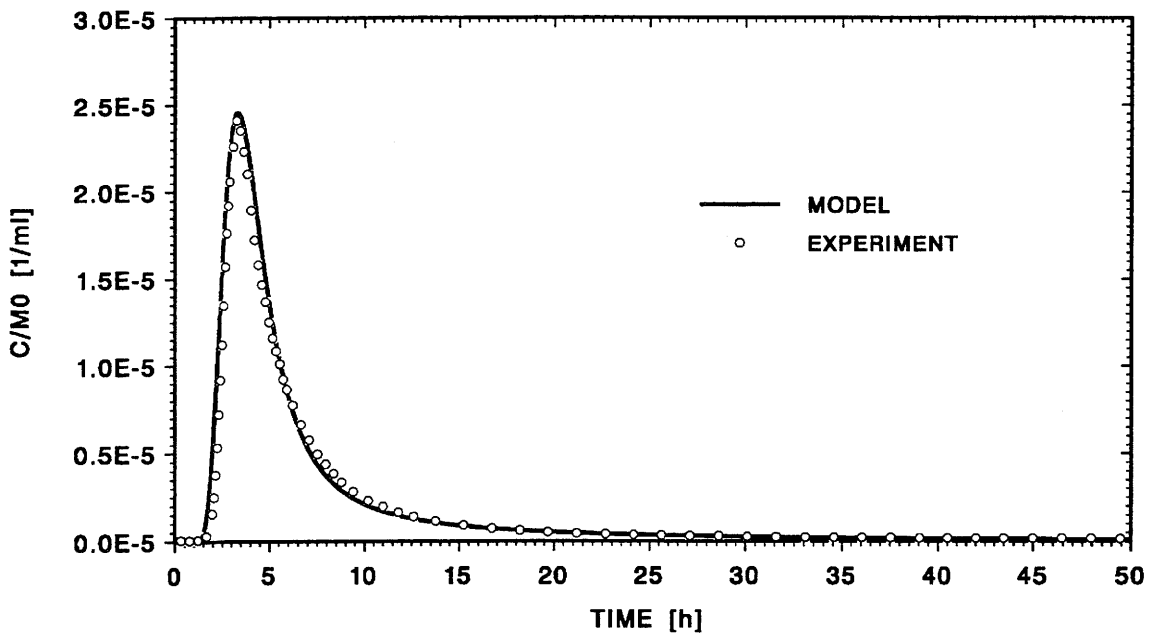
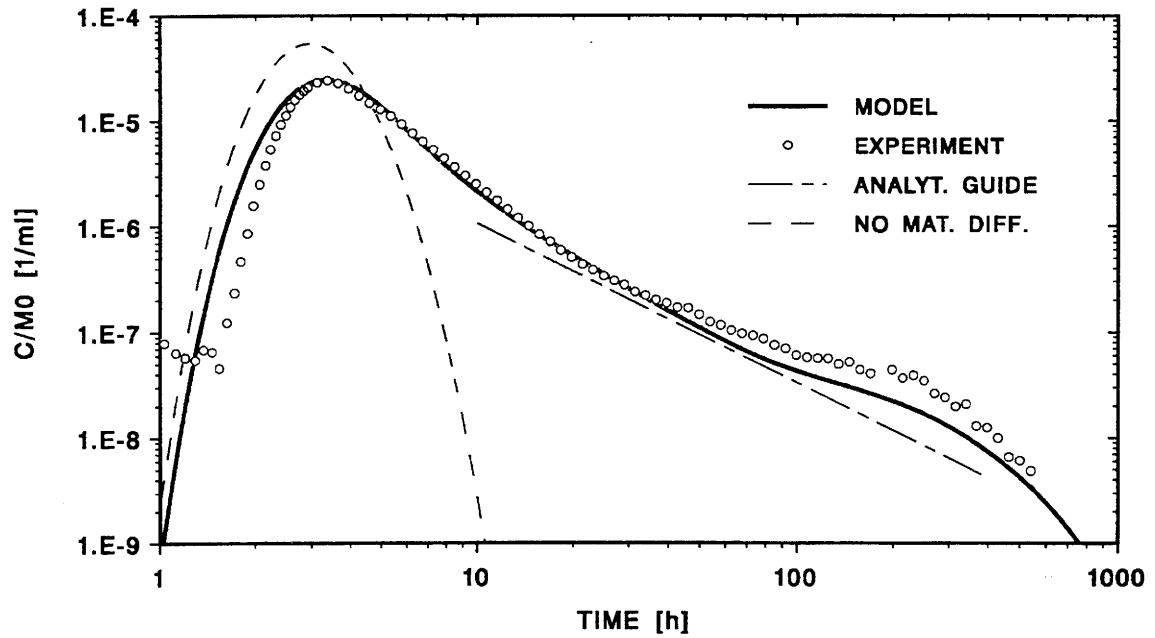


Figure 10 Breakthrough curves for uranine in the 4.9 m dipole flow field (TEST 50). Upper part: The model (solid line) is able to fit the experiment (circles). A calculation without matrix diffusion (dashed line) and the experimental tail approaching the $t^{-3/2}$ decay (dot-dashed line) is a clear indication for matrix diffusion. Lower part: The presentation on linear scale confirms the quality of the fit.

Tab. 1 Characteristic Data of the Breakthrough Curve for Uranine

PART	DATUM	EXPERIMENT	(MOD-EXP)/EXP
PEAK	C_{fm}/M_o	$2.42 \cdot 10^{-5} \text{ ml}^{-1}$	2 %
	t_m	3.30 h	1 %
	$s/2$	0.98 h	20 %
TAIL	$C_f (33 \text{ h})/M_o$	$2.27 \cdot 10^{-7} \text{ ml}^{-1}$	- 4 %
TOT	Recovery (500 h)	1.00 ± 0.05	0 %

Parameters: From the fit of the breakthrough curve, the following parameters have been extracted. These are assumed to follow a log-normal distribution in order to perform a consistent error estimate, including the large errors of the fixed parameters:

$$(\epsilon a) = (3.7 \pm 0.2) \cdot 10^{-4} \text{ m} \quad ; \quad \Sigma(\epsilon a) = 1.05 \quad , \quad (35a)$$

$$a_L = (0.25^{+0.05}_{-0.04}) \text{ m} \quad ; \quad \Sigma(a_L) = 1.2 \quad , \quad (35b)$$

$$F_c = (3.10^{+0.2}_{-0.1}) \cdot 10^{-7} \text{ ms}^{-1/2} \quad ; \quad \Sigma(F_c) = 1.05 \quad , \quad (35c)$$

$$B_c = (2.00^{+0.4}_{-0.3}) \cdot 10^5 \text{ m}^{-1} \text{ s}^{1/2} \quad ; \quad \Sigma(B_c) = 1.2 \quad . \quad (35d)$$

The best fit was selected “by eye”⁷⁶. The uncertainties given are the maximum ranges yielding a still reasonable fit and are taken as pessimistic guesses for 1 geometric standard deviation.

From the fit parameters F_c and B_c ⁷⁷, the physical parameters of the porous rock zone can be deduced by the following relations:

⁷⁶It is envisaged to redo the fit using a non-linear least-square technique.

⁷⁷It must be stressed that, in cases where the breakthrough curve is not measured up to the final drop of the tail, no information to determine B_c is available and a separate evaluation of ϵ_{pc} and D_{pc} is impossible.

$$\epsilon_{pc} = F_c \cdot B_c \quad , \quad (36a)$$

$$D_{pc} = \left(\frac{1}{B_c} \right)^2 \quad , \quad (36b)$$

b , d from Eqs. (34b) and (34c) .

Using the numerical values of Eqs. (35), we obtain the physical parameters. The errors are calculated according to App. 4. The total errors include the uncertainties of the fixed parameters. The contribution of the fitting error is separately exhibited. The error contributions of the fixed parameters, Eqs. (33), are dominant, especially in the case of D_{pc} ⁷⁸:

$$\epsilon_{pc} = (6.2_{-3.2}^{+6.8}) \cdot 10^{-2} \quad , \quad (37a)$$

$$\Sigma_{tot}(\epsilon_{pc}[\delta a]) = 2.1 \quad ; \quad \Sigma_{fit}(\epsilon_{pc}) = 1.2 \quad , \quad (37b)$$

$$D_{pc} = (2.5_{-2.0}^{+10.5}) \cdot 10^{-11} \text{ m}^2/\text{s} \quad , \quad (37c)$$

$$\Sigma_{tot}(D_{pc}[\delta a, \delta n]) = 5.2 \quad ; \quad \Sigma_{fit}(D_{pc}) = 1.4 \quad , \quad (37d)$$

$$b = (4.63_{-1.5}^{+2.3}) \cdot 10^{-5} \text{ m} \quad , \quad (37e)$$

$$\Sigma_{tot}(b[\delta n]) = 1.5 \quad ; \quad \Sigma_{fit}(b) = 1.05 \quad , \quad (37f)$$

$$d = (6.20_{-3.4}^{+7.4}) \cdot 10^{-3} \text{ m} \quad , \quad (37g)$$

$$\Sigma_{tot}(d[\delta a, \delta n]) = 2.2 \quad ; \quad \Sigma_{fit}(d) = 1.0 \quad . \quad (37h)$$

⁷⁸The error of D_{pc} is dependent on the square of both fixed parameters, a and n (cf. App. 4, Eq. (A4.4b)).

From independent investigations of the migration fracture, average physical parameters for the fault gouge region (approximating the model's porous rock zone) can be deduced (cf. App. 5, Eqs. (A5.2e) and (A5.4a)):

$$\epsilon_{pF} = (1.2_{-0.5}^{+0.8}) \cdot 10^{-1} \quad , \quad (38a)$$

$$D_{pF} = (7.5_{-4}^{+8}) \cdot 10^{-11} \text{ m}^2/\text{s} \quad . \quad (38b)$$

Within error bars, and within a factor of 3 for the median, these values agree with those given above showing a nice general consistency. A qualitative explanation of the higher median values in Eqs. (38) is the omission of the rock outside the fault gouge.

The depth d_F of the fault gouge corresponding to a single water conducting zone surface can also be estimated from the pictures of structural analysis (cf. App. 5, Eq. (A5.2d)):

$$d_F = 8.3 \cdot 10^{-4} \text{ m} \quad . \quad (38c)$$

The half width b of the water conducting zone deduced from the fit is roughly a factor 20 smaller than d_F which is in line with the idea of narrow water conducting zones within the fault gouge. The depth d of the porous rock zone corresponding to the fit is a factor 7 larger than d_F . This might be explained by the approximation of the model, representing the fault gouge as well as the adjacent mylonite or granodirite (up to the plane of symmetry) by one single porous rock zone.

4.2.3 Parameter Variations

In order to get indications on the impact of parameter uncertainties, such as given in previous sections, and to improve physical understanding, the influence of parameter changes on the calculated breakthrough characteristic is investigated⁷⁹. The impact is clearly dependent on the starting values, in our case for a breakthrough curve dominated by advection-dispersion and noticeably modified by matrix diffusion.

⁷⁹The values for Q_i , β , M_0 and $C_0(t)$ remain unchanged.

Flow width: A change of the flow width (ϵa) means essentially⁸⁰ change of b and \bar{v}_k according to Eqs. (34a) and (34b). The influence of an increase of (ϵa) by a factor of 2 is depicted in Fig. 11 (upper part): The delay of the front is due to the smaller advection velocities \bar{v}_k . The reduction of the peak height C_{fm}/M_0 is due to the larger cross section areas $(\epsilon a) \cdot B_k$ of the water conducting zones to which the tracer nuclides (from an unchanged injection flow $Q_i \cdot C_0(t)$) have to be distributed⁸¹. The unchanged tail reflects the compensating effects of changing b and \bar{v}_k ⁸². To isolate the influence of these changes, the calculation was also carried out for velocities \bar{v}_k reduced by a factor of 2 (triangles)⁸³. An additional decrease of peak height and increase of tail amplitude due to enlarged matrix diffusion effects, not compensated any more, is seen. The breakthrough curves without matrix diffusion, shown in Fig. 11 (lower part), confirm that the change of peak height, position and width is mainly due to advection and dispersion⁸⁴. Quantitative information summarized in Tab. 2, shows that the increase of (ϵa) by a factor of 2 reduces the peak height C_{fm}/M_0 by 37% (factor 1/1.6) and enlarges the peak width s in a similar way by 75% (factor 1.8). Without matrix diffusion, the corresponding effects are noticeably larger. The reason is that matrix diffusion widens both curves in a comparable way (same τ_0). Therefore the effect of (ϵa) is reduced. The analytical guess, when approximating the peak by considering advection and dispersion only, and the tail by considering advection and matrix diffusion only, provides a reasonable rough estimate of the changes. The reason that the changes of the peak from the analytical guess and the numerical calculation without matrix diffusion differ (especially for Δt_m), is that the experimental injection distribution is taken into account, in the numerical calculation only. Keeping b constant, the change of \bar{v}_k , ($\bar{v}_k' = \bar{v}_k/2$) shows how strongly an uncompensated matrix diffusion would reduce C_{fm}/M_0 and increase s . Especially noteworthy is the increase of the tail amplitude by $\approx 100\%$. The analytical guess is a reasonable guide, also in this case.

⁸⁰The corresponding change of d is almost negligible.

⁸¹Compare Eq. (A2.4a), since the peak is dominated by advection and dispersion.

⁸²Compare Eqs. (34a), (34b), (27f) and (29), since the tail is dominated by matrix diffusion.

⁸³The flow through the water conducting zones is the same as before. It flows through a cross section $(\epsilon a) \cdot B_k$, where instead of (ϵa), B_k is now changed correspondingly to \bar{v}_k . The advective-dispersive reduction of peak height is the same as before. (Only a change of \bar{v}_k generated by a change of Q_i and Q_w , to keep β constant, would have no advective-dispersive change of C_{fm}/M_0 , since in this case, M_0 is changed accordingly, as shown in Eq. (17b)).

⁸⁴Without matrix diffusion the case $(\epsilon a)' = 2(\epsilon a)$ is identical to the case $\bar{v}_k' = \bar{v}_k/2$.

Tab. 2 Influence of Parameter Changes to the Calculated Breakthrough Curve of the Conservative Tracer Uranine

PARAMETER-CHANGE	PEAK			TAIL 4)	COMMENTS
	$\Delta (C_{fm} / M_o) [\%]$	$\Delta t_m [\%]$	$\Delta s [\%]$	$\Delta (C_{ft} / M_o) [\%]$	
$(\epsilon a)' = 2 (\epsilon a)$	-37 -49 -50 1)	74 79 100 1)	75 94 100 1)	19 -- 0 2) 3)	numerical with mat. diff. numerical no mat. diff. analytical guess
$\bar{v}_k' = \bar{v}_k / 2$ (b const.)	-62 -50 1)	93 100 1)	135 100 1)	125 100 2)	numerical with mat. diff. analytical guess
$a_L' = a_L / 2$	11 21 41 1)	8 7 3 1) 3)	-13 -16 -29 1)	2 -- 0 2) 3)	numerical with mat. diff. numerical no mat. diff. analytical guess
$F_c' = 2 F_c$	-48 --	16 18 2) 5)	52 --	91 100 2)	numerical with mat. diff. analytical guess
$B_c' = 2 B_c$	0	0	0	0	numerical with mat. diff.
$D_{pc}' = 2 D_{pc}$ (ϵ_{pc} const.)	-25 --	6 6 2) 5)	19 --	39 41 2)	numerical with mat. diff. analytical guess

- 1) Analytical guess according to advection and dispersion only (cf. App.2, Eqs. (A2.5a), (A2.5c) and (A2.5e)).
- 2) Analytical guess according to advection and matrix diffusion, only (cf. Eqs. (27f), (28b) and (29)).
- 3) Independent of the size of the parameter change.
- 4) $C_{ft} = C_f(t = 33 \text{ h})$.
- 5) $t_m = \bar{t} + t(INJ) + \frac{2}{3} \tau_o$ where $\bar{t} \approx \bar{t} (3.ST) = 2.63 \text{ h}$ and $t(INJ) \approx 0.33 \text{ h}$ (The t_m from the analytical guess is corrected for the delay $t(INJ)$ from the injection distribution).

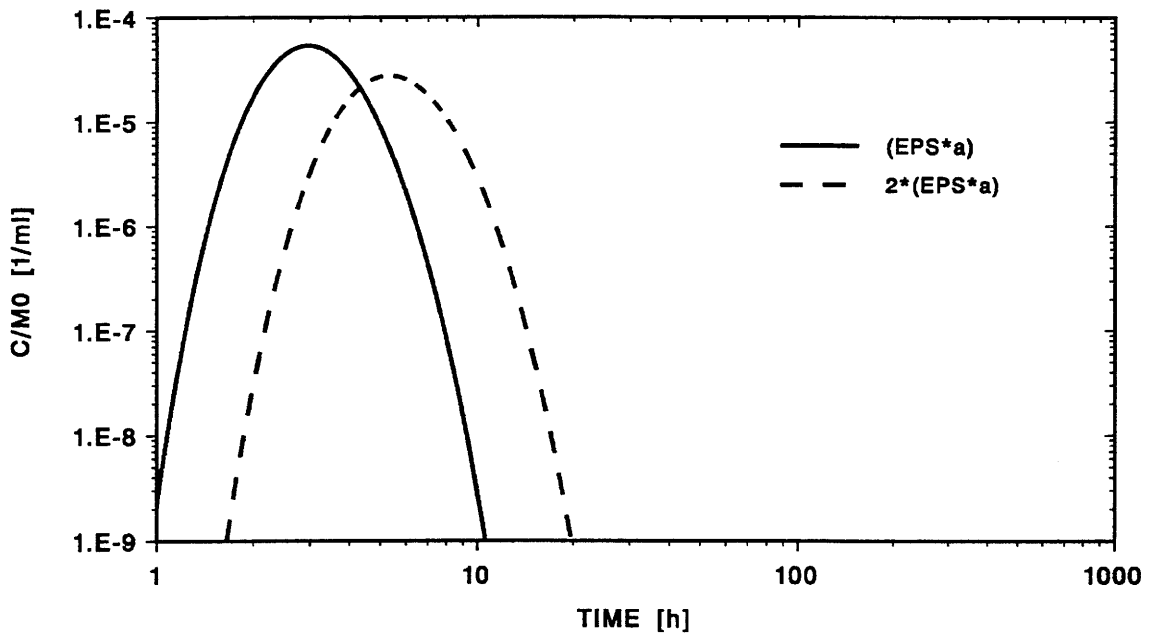
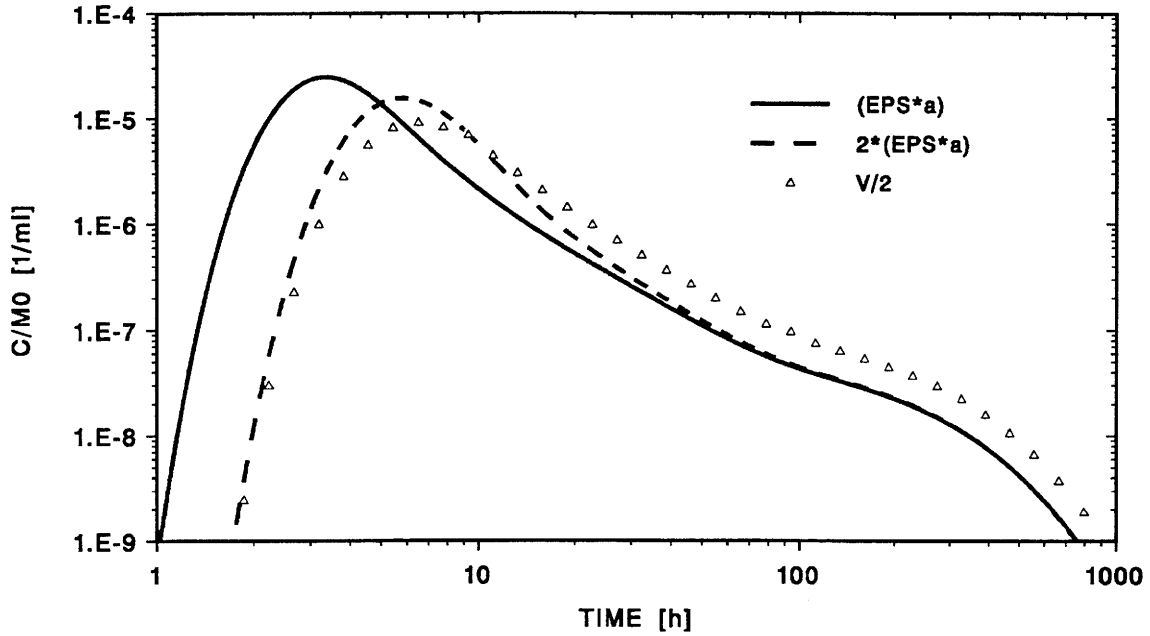


Figure 11 Influence of the flow width (ϵa) and the water velocities \bar{v}_k on the breakthrough curve for uranine. Upper part: By doubling (ϵa) the peak is delayed and reduced (from the solid to the dashed line). Halving \bar{v}_k instead (triangles) delays the peak in a similar way but increases simultaneously the tail amplitude. Lower part: A calculation without matrix diffusion shows that the change of peak is governed mainly by advection and dispersion.

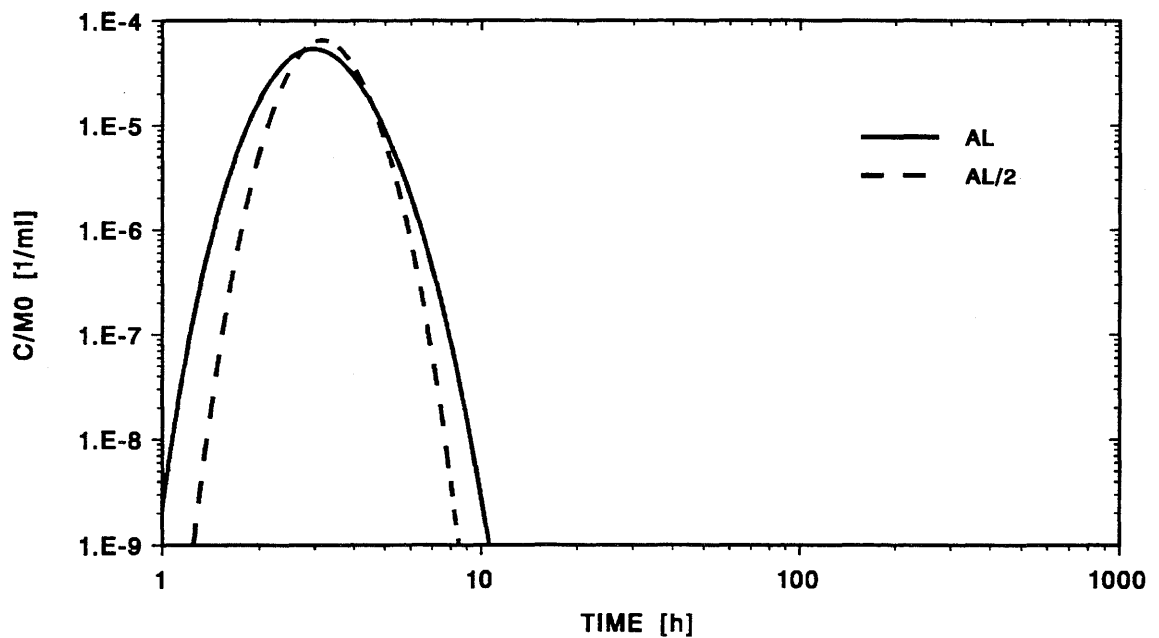
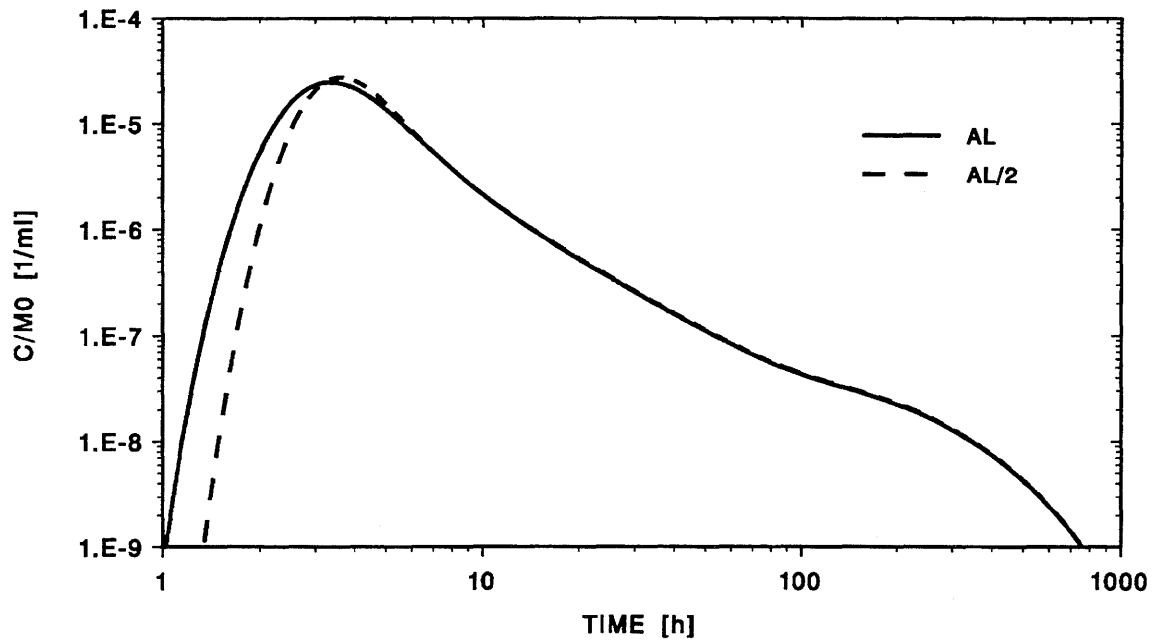


Figure 12 Influence of the dispersion length a_L on the breakthrough curve for uranine. Upper part: By halving a_L , the peak is shifted and slightly increased (from the solid to the dashed line). Lower part: A calculation without matrix diffusion exhibits more explicitly the influence of a_L onto the peak.

Dispersion Length: The influence of a reduction of the dispersion length a_L by a factor of 2⁸⁵ is shown in Fig. 12 (upper part) and Tab. 2. A relatively small increase of peak height, decrease of peak width, delay of peak position and practically no change of the tail is observed, as expected. The effect without matrix diffusion, presented in Fig. 12 (lower part) and Tab. 2, yields larger changes of C_{fm}/M_0 and s as is the case when changing (ϵa) . The difference of the effect between the analytical guess and the calculation without matrix diffusion is caused here, too, by the experimental injection distribution taken into account only in the numerical calculations⁸⁶.

Interface Flux Parameter: The influence of an increase of the interface flux parameter F_c by a factor 2 is presented in Fig. 13 (upper part) and complemented by the data in Tab. 2. We see the typical behaviour of an increased matrix diffusion (reduced peak height, increased tail amplitude and a small retardation)⁸⁷. The tail concentration is increased roughly proportional to F_c which is in line with the analytical guess. Noteworthy is the unchanged shape of the tail: After a long time, the backflow from the porous rock zone is dependent on the elapsed time, only, and not on the shape of the tracer peak having passed in the water conducting zone⁸⁸. Since the peak height is governed to a large extent by dispersion, the effect of stronger matrix diffusion cannot be estimated by the analytical guess (which neglects dispersion). However, for the peak position t_m a prediction is possible. The change of the breakthrough curve due to the increase of F_c is the same as the change from the dashed line to the triangles observed in Fig. 11 (upper part) (neglecting the shifted peak position due to the lower water velocities). The reason is that matrix diffusion is governed by $\epsilon_{pc}\sqrt{D_{pc}}/b$ (cf. App. 3, Eq. (A3.2b)). In Fig. 11 we see the effect of a decrease of b , and in Fig. 13 that of an increase of $\epsilon_{pc}\sqrt{D_{pc}}$, both by the same factor. The comparison of Fig. 11 and Fig. 13 also shows that, for our application, (ϵa) and F_c is a reasonable pair of fit parameters, describing essentially two different features of the breakthrough curve (which would not be the case taking the pairs \bar{v}_k and F_c , or \bar{v}_k and ϵ_{pc}).

⁸⁵Instead of an increase, a decrease is investigated in order to restrict the Peclet number, $Pe = L_k/a_L$, to values not substantially smaller than 20.

⁸⁶In the base case ($a_L = 0.25$ m) the influence of the injection distribution on C_{fm}/M_0 and s is almost “smeared out” by dispersion. The influence on t_m remains, but is minimized by dispersion (asymmetric form of the injection distribution having a steeper front). In the changed case ($a_L = 0.125$ m), however, the injection distribution still reduces C_{fm}/M_0 , enlarges s and enlarges t_m more than in the base case. This leads in the numerical calculations to a smaller increase of C_{fm}/M_0 , a smaller decrease of s but also a larger increase of t_m (compared to the analytical guess).

⁸⁷For $\epsilon_{pc}' = 2 \epsilon_{pc}$ (keeping $D_{pc} = \text{const}$) an identical effect would be apparent.

⁸⁸In Ref. ([16], App. 3) it is shown that for a porous rock zone with an infinite depth, the breakthrough curve C_f/M_0 is independent on the width of a narrow injection pulse. According to the Fig. 13 this seems also valid for a finite depth.

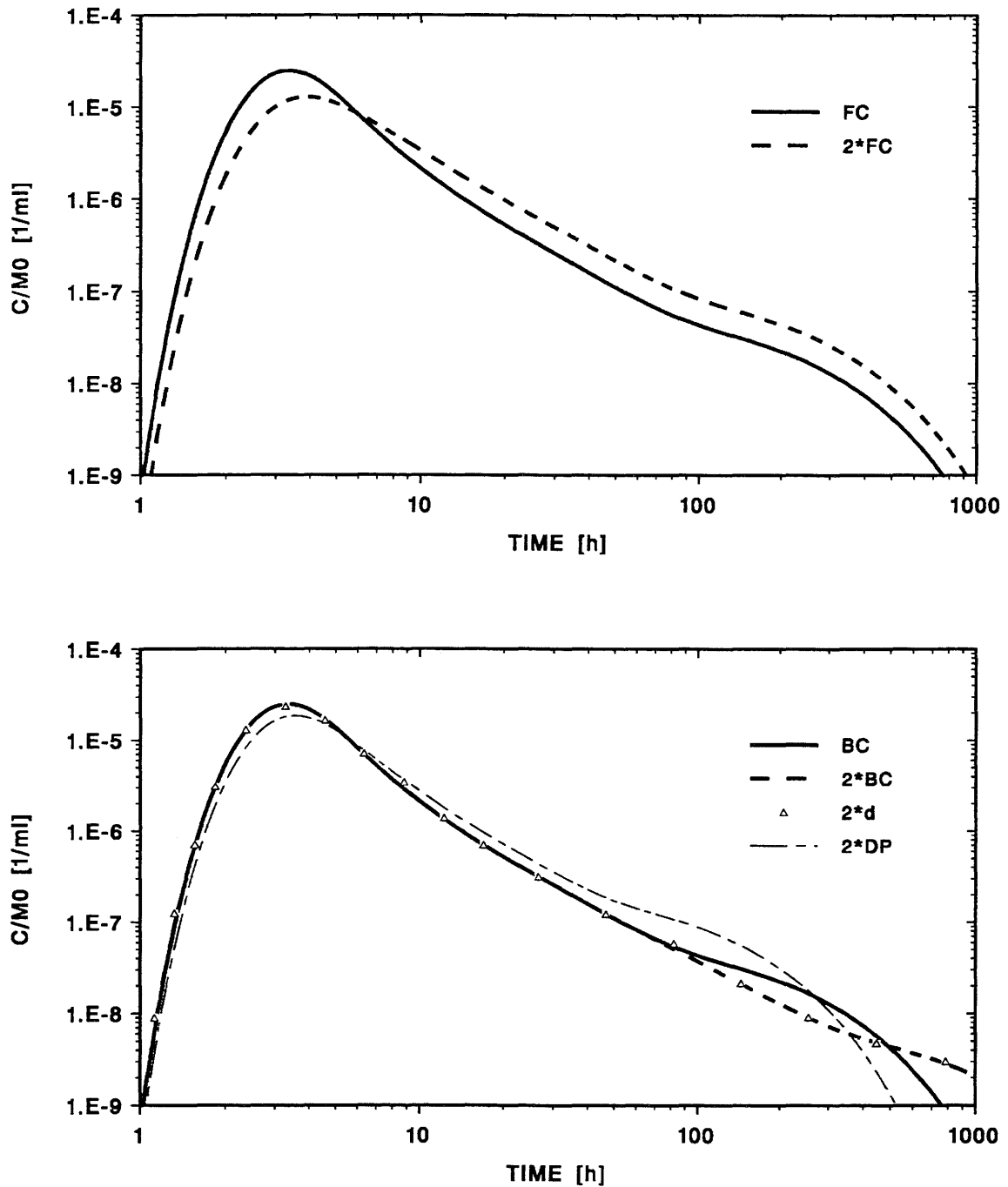


Figure 13 Influence of the interface flux parameter F_c and the tail end parameter B_c on the breakthrough curve for uranine. Upper part: By doubling F_c the tail amplitude is increased and the peak reduced (from the solid to the dashed line) showing the effect of matrix diffusion. Lower part: The most important result is the unchanged peak and the delayed tail end perturbation if B_c is doubled (dashed with respect to solid line).

Tail End Parameter: The effect of an increase of the tail end parameter B_c by a factor of 2 is depicted in Fig. 13 (lower part; dashed with respect to solid line) and complemented by the data in Tab. 2. We see that B_c only influences the position of the tail end perturbation. Alternatively, an increase of D_{pc} by a factor of 2, keeping ϵ_{pc} constant, (dot-dashed with respect to solid line) does not only shift the tail end perturbation, but changes also peak and tail of the breakthrough curve similar to F_c (but less pronounced⁸⁹). This demonstrates that, for our application, the fit parameter B_c nicely complements F_c , whereas the pair D_{pc} and ϵ_{pc} would be less favourable. According to Eq. (A3.3d) in App. 3 we expect the same effect for an increase of d instead of B_c . This is confirmed by the calculation (triangles). The increase of B_c shifts the beginning of the tail end perturbation from ≈ 80 h to ≈ 270 h. This is in line with the rough guess in App.3 (comment 3, Eq. (A3.4)), predicting a shift of the tail end region $\sim B_c^2$ (i.e. by a factor of 4).

4.2.4 Influence of the Injection Distribution

To illustrate this influence, breakthrough curves are calculated for different injection distributions. The selected injections are shown in Fig. 14. The high narrow square pulse on the left (dotted line) is typical for a tracer injection neglecting delay and dispersion in the inlet device. Taking into account such effects reduces the height, enlarges the width, and delays the position of the injection distribution as shown by the experimental pulse (solid line) measured down hole at the inlet of the migration shear zone. To enhance the influence of injection, the experimental pulse is artificially widened by maintaining the maximum concentration for 2 h (dot-dashed line) and for 10 h (dashed line). The reduced heights are a consequence of the normalization by the total mass M_0 .

The corresponding breakthrough curves, plotted on a linear scale in the upper part of Fig. 15, show especially the influence on the peak. Comparing first the breakthrough curves from the high square injection (dotted line) and the experimental injection (solid line), we observe, in spite of the very different injection heights (factor 9), an almost identical shape. The insensitivity of the breakthrough shape from substantially narrower injection distributions is demonstrated. This facilitates interpretation, and is the reason for normalizing our breakthrough curves by the total mass M_0 (at the expense of dimensional breakthrough curve representations). The shift of the two breakthrough curves nevertheless shows a strong de-

⁸⁹According to the results of the numerical calculations represented in Tab. 2, changing D_{pc} ($\epsilon_{pc} = \text{const.}$) increases the tail amplitude C_{ft}/M_0 by a factor of $1.4 \approx \sqrt{2}$, whereas changing F_c (or ϵ_{pc} ($D_{pc} = \text{const.}$)) leads to a factor of $1.9 \approx 2$. This is consistent with the analytical guess.

pendency on the average injection time. It is mainly this dependency which is taken into account by the down hole measurement of the injection distribution (in the 4.9 m dipole experiments considered here). As soon as the width of the injection distribution approaches that of the breakthrough curve the influence of the injection becomes substantial (dot-dashed line). The 1.7 m dipole experiments considered in chapter 5 are of this kind, and there it is especially important to take into account a properly measured injection distribution. For the long injection time (compared to the width of the dotted breakthrough curve), almost a step response is obtained (dashed line). Note the slow approach to a steady state situation due to matrix diffusion.

In the lower part of Fig. 15 the breakthrough curves are plotted on logarithmic scales. At times large with respect to the positions of the maximum breakthrough concentrations, the tails are independent of the very different injection distributions. It shows the usefulness of the adopted normalization and the insensitivity of the breakthrough tails to the detailed shape of the concentration distributions passing in the water conducting zones.

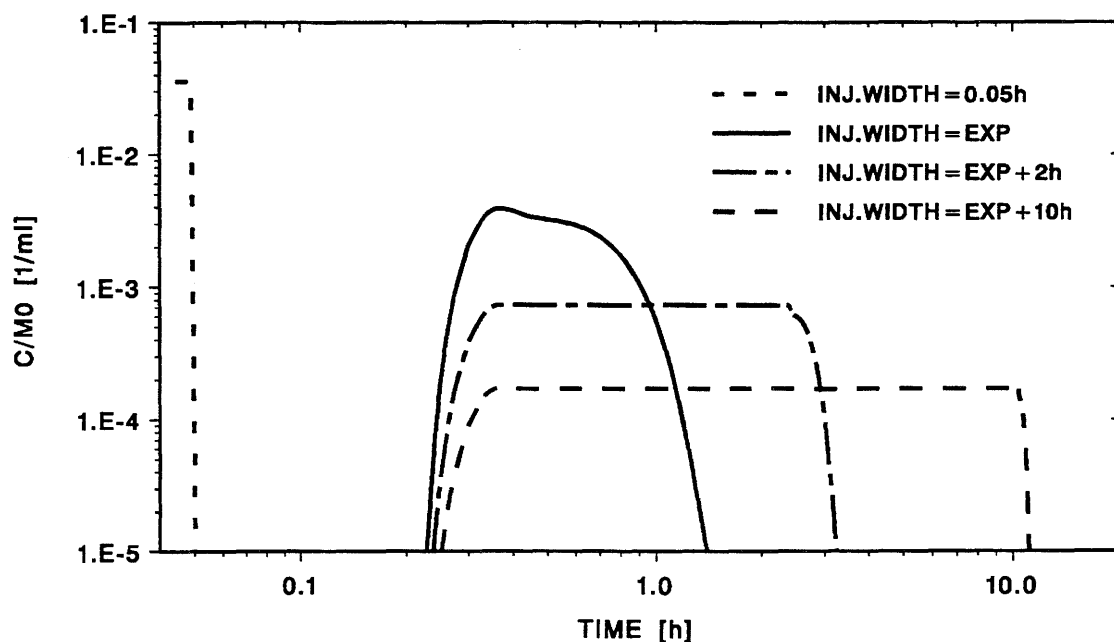


Figure 14 Injection distributions of different width, selected to demonstrate the influence of injection shape on the breakthrough curve.

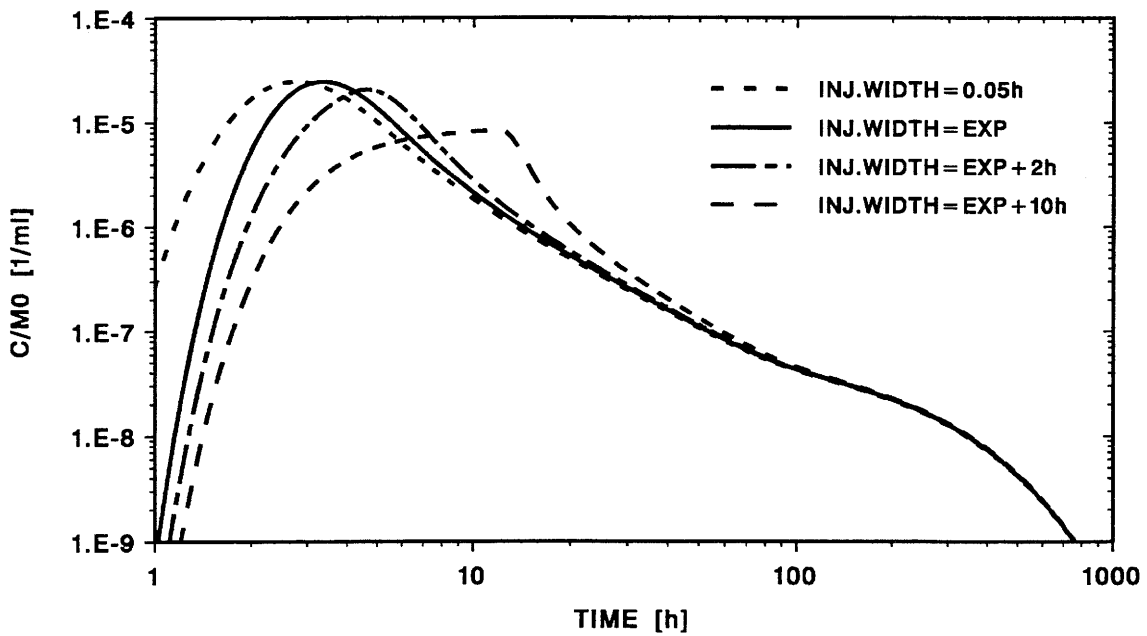
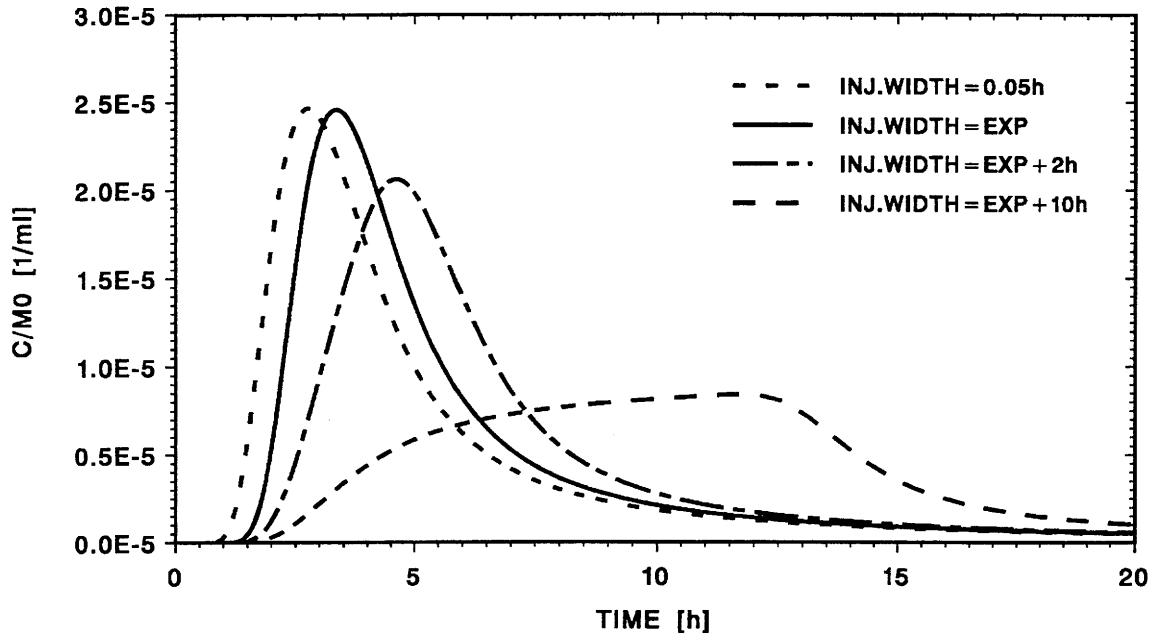


Figure 15 Breakthrough curves for different injection distributions (shown in Figure 14). Upper part: The linear scales show that the breakthrough curves have the same shape if the injection widths are small compared to the breakthrough width (dotted and solid line). Lower part: The logarithmic scales show at large times the same tail for all breakthrough curves.

4.3 Sorbing Tracers

Experimental breakthrough curves for the linearly⁹⁰ sorbing tracers Na and Sr were measured in the same dipole flow field. The analysis of these curves should answer the following questions:

1. How reliable is the model in describing sorbing tracer transport?
2. Is sorption controlled mainly by matrix diffusion and subsequent interaction of the tracer with pore surfaces? How strong is surface sorption in the water conducting zones?
3. Do we observe an indication for an infill in the water conducting zones?
4. Is there an influence of sorption heterogeneities along the flow path leading to a change in dispersion length, as proposed in Ref. [14].
5. How consistent are the sorption values from field measurements with those of other experiments?

4.3.1 Selection of Fit Parameters

Sodium: This nuclide is a weakly sorbing tracer. The tail end of the breakthrough curve can be measured. Similarly to the calibration experiment we use four fit parameters:

R_f : **The retardation factor due to surface sorption;** to correct peak position.

a_L : **The dispersion length;** to correct mainly the front shape, if necessary.

F_s : **The interface flux parameter,** including now the retardation factor R_{ps} ,⁹¹ due to porous rock zone sorption. Its adjustment mainly determines peak height position and width as well as the tail amplitude:

$$F_s = \epsilon_{ps} \cdot \sqrt{D_{ps}} \cdot \sqrt{R_{ps}} \quad . \quad (39a)$$

⁹⁰The tracers were injected at concentrations well below the natural background in the Grimsel water so that they do not change noticeably the chemical equilibrium.

⁹¹The index s signifies extraction from the experiment with a weakly sorbing tracer.

B_s : The tail end parameter; to fit the tail end perturbation, now including R_{ps} :

$$B_s = \frac{\sqrt{R_{ps}}}{\sqrt{D_{ps}}} . \quad (39b)$$

From the two fit parameters F_s and B_s , only combinations of the three physical parameters ϵ_{ps} , D_{ps} and R_{ps} can be deduced⁹². To derive R_{ps} , we have to know either ϵ_{ps} or D_{ps} . We assume that ϵ_{ps} can be approximated by ϵ_{pc} . This assumption is justified by the large value of ϵ_{pc} , (cf. Eq. (37a)) and by the fact that diffusion of both, sorbing and non-sorbing tracers, is taking place mainly in the same region, the fault gouge⁹³. Hence:

$$\epsilon_{ps} = \epsilon_{pc} . \quad (40)$$

From Eqs. (39), (36) and (21b) we get for the physical parameters:

$$D_{ps} = \frac{F_s}{B_s \cdot F_c \cdot B_c} , \quad (41a)$$

$$R_{ps} = \frac{F_s \cdot B_s}{F_c \cdot B_c} , \quad (41b)$$

$$K_{ds} = \frac{1}{\tilde{\rho}_p} \cdot F_s \cdot B_s \cdot \left[1 - \frac{F_c \cdot B_c}{F_s \cdot B_s} \right] . \quad (41c)$$

Strontium: This nuclide is more strongly sorbing. The procedure is similar as for sodium, the difference being a not detectable tail end perturbation. Therefore, only one single fit parameter for the porous rock zone can be determined⁹⁴:

⁹²For large sorption, R_{ps} is proportional to K_{ds}/ϵ_{ps} (cf. Eq. (21b)) and therefore K_{ds} can be determined by Eqs. (39), independently of ϵ_{ps} . In practical cases, however, this would rarely be possible, since for large sorption the tail end perturbation will be swamped by experimental detection limits.

⁹³The penetration depth $\{d_p(s) - b\} = 2 \sqrt{(D_p/R_p)} \cdot s$ for a square pulse, having the same width s as the breakthrough curve, is not substantially larger than the depth d_F of the fault gouge:

$\{d_p(s) - b\}$ (uranine) = $8.4 \cdot 10^{-4}$ m (Tab.1, Eqs. (37c) and (37e))

$d_F = 8.3 \cdot 10^{-4}$ m (Eq. (A5.2d))

$\{d_p(s) - b\}$ (sodium) = $5.8 \cdot 10^{-4}$ m (Tab. 3, Eqs. (46a) and (46c))

$\{d_p(s) - b\}$ (strontium) = $3.6 \cdot 10^{-4}$ m (Tab. 4, Eqs. (43b), (48) and (49a))

⁹⁴Here, the index ss signifies extraction from the experiment with the more strongly sorbing tracer.

$$F_{ss} = \epsilon_{pss} \cdot \sqrt{D_{pss}} \cdot \sqrt{R_{pss}} \quad . \quad (42)$$

To get an information on R_{pss} we have now to provide, in addition to ϵ_{pss} , the diffusion coefficient D_{pss} . It is postulated that D_{pss} can be deduced from D_{pc} by multiplication with a nuclide specific factor E_D . According to our assumptions and to Eqs. (42), (36) and (21b) we get:

$$\epsilon_{pss} = \epsilon_{pc} \quad , \quad (43a)$$

$$D_{pss} = E_D \cdot D_{pc} \quad , \quad (43b)$$

$$R_{pss} = \left(\frac{F_{ss}}{F_c} \right)^2 \cdot \frac{1}{E_D} \quad , \quad (44a)$$

$$K_{dss} = \frac{1}{\tilde{\rho}_p} \cdot \frac{F_{ss}^2 \cdot B_c}{F_c \cdot E_D} \cdot \left[1 - \left(\frac{F_c}{F_{ss}} \right)^2 \cdot E_D \right] \quad . \quad (44b)$$

4.3.2 Results and Parameter Variations for Sodium

Fitted Breakthrough Curve: The fit of the model to the experimental breakthrough curve is presented in Fig. 16 (upper part). It shows that the model is able to represent closely peak height position and width, as well as the overall shape of the tail. As was the case and commented for uranine, the fit of the tail end perturbation is less accurate. The analytical guide⁹⁵ (dot-dashed line) shows the usefulness of an estimate, considering only advection and matrix diffusion, even for cases with small sorption. It approximates large parts of the tail and also peak position surprisingly well. Clearly, a steep front, overestimating of peak height, and the missing tail end perturbation are typical limitations of the analytical solution. The single porosity breakthrough curve (dashed line) is also exhibited using a retardation factor R_f to match the peak position. As in the case of uranine, the salient features of the breakthrough curve are not reproduced by the single porosity model⁹⁶.

⁹⁵Eqs. (27) to (29) and accounting for dilution (division by β).

⁹⁶A detailed fit was not tried, since from the shape of the breakthrough curve it is already clear that a reasonable fit is not possible (tailing).

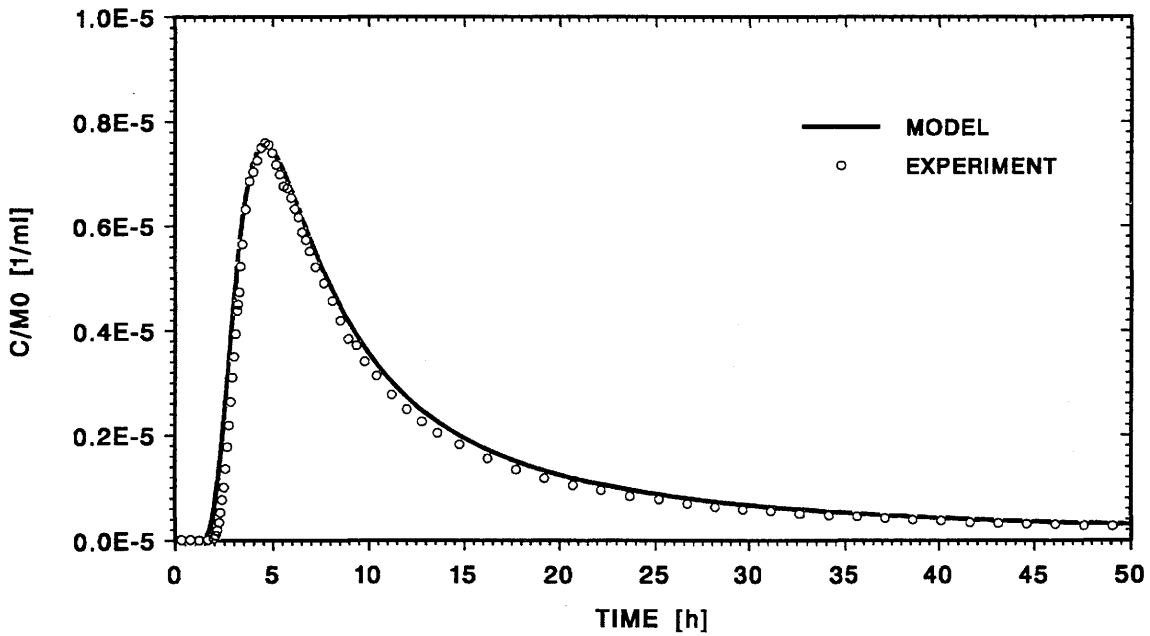
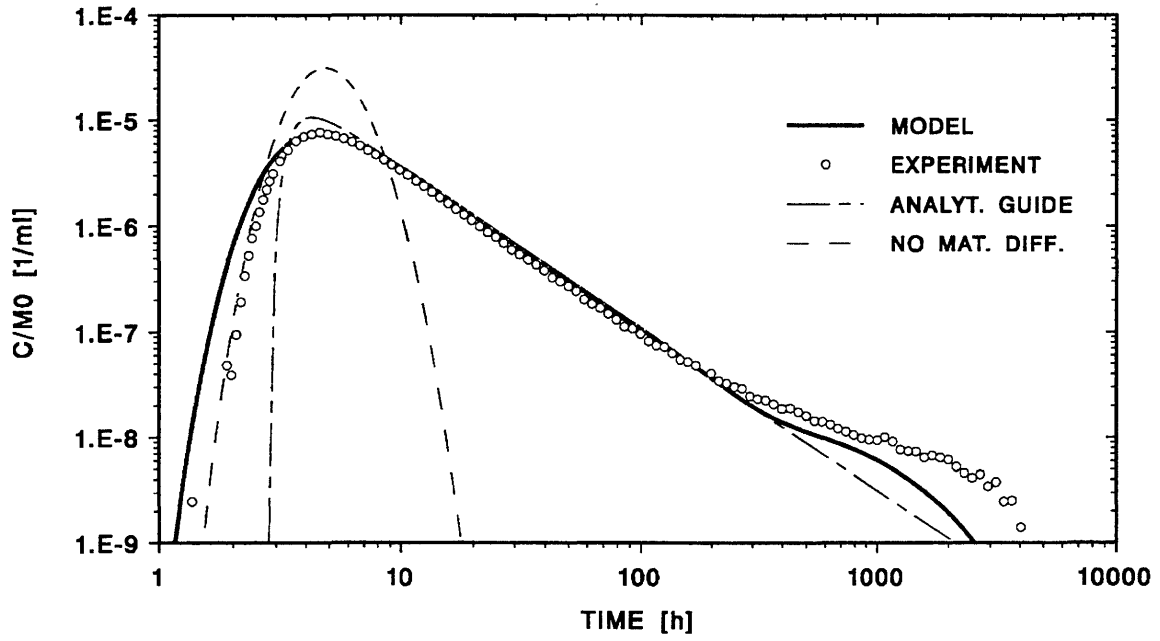


Figure 16 Breakthrough curves for sodium in the 4.9 m dipole flow field (TEST 50). Upper part: The model (solid line) is able to fit the experiment (circles). The tail is an impressive example for the $t^{-3/2}$ drop, indicated by a simplified analytical expression (dot-dashed line) and showing the signature of matrix diffusion. Lower part: The presentation on linear scales confirms the quality of the fit.

A quantitative summary of the experimental breakthrough curve and the deviations of the fitted model values is given in Tab. 3 confirming the good quality of the model also for sodium.

Tab. 3 Characteristic Data of the Breakthrough Curve for Sodium

PART	CHAR. DATA	EXPERIMENT	(MOD-EXP)/EXP
PEAK	C_{fm}/M_0	$7.70 \cdot 10^{-6} \text{ ml}^{-1}$	- 2 %
	t_m	4.70 h	- 2 %
	$s/2$	2.33 h	15 %
TAIL	$C_f (47 \text{ h})/M_0$	$2.88 \cdot 10^{-7} \text{ ml}^{-1}$	17 %
TOT	Recovery (4830 h)	1.04 ± 0.06	- 4 %

We now turn our attention to the influence of sorption and to a comparison with the results for uranine (Figs. 10 and 16, Tabs. 1 and 3). We observe a reduction of peak height by a factor of 3 and a shift of peak position by 40%, as well as a marked increase of the range where the $t^{-3/2}$ dependency applies. The reduction of peak height is generated by an increased outflow from the water conducting zone into the porous rock zone due to bulk sorption. The correspondingly small retardation of peak position is typical for a fractured medium field experiment situation with small distances, high mean velocities and small sorption. Large parts of the tracer inventory are not affected by the bulk sorption. Tracer back-flow from the porous rock zone is largely controlled by the $t^{-3/2}$ law. Since the advective-dispersive dominated peak is less pronounced for sodium, the $t^{-3/2}$ tail is seen earlier. Since sorption in the porous rock zone retards tracer diffusion, the influence of the no-flow boundary arises later and the $t^{-3/2}$ dependency holds over a longer period.

Parameters: The theoretical breakthrough curve corresponds to the following fit parameters:

$$R_f = 1 \quad (\text{same value as for uranine}^{97}) \quad , \quad (45a)$$

$$a_L = 0.25 \text{ m} \quad (\text{same value as for uranine}^{97}) \quad , \quad (45b)$$

$$F_s = (9.16_{-0.4}^{+0.5}) \cdot 10^{-7} \text{ m s}^{-1/2} \quad ; \quad \Sigma(F_s) = 1.05 \quad , \quad (45c)$$

$$B_s = (4.47_{-1.5}^{+2.2}) \cdot 10^5 \text{ m}^{-1} \text{ s}^{1/2} \quad ; \quad \Sigma(B_s) = 1.5 \quad . \quad (45d)$$

Applying Eqs. (41) and the error estimates in App. 4 we get⁹⁸:

$$D_{ps} = (3.3_{-2.7}^{+14}) \cdot 10^{-11} \text{ m}^2/\text{s} \quad , \quad (46a)$$

$$\Sigma_{tot}(D_{ps}[\delta a, \delta n]) = 5.3 \quad ; \quad \Sigma_{fit}(D_{ps}) = 1.6 \quad , \quad (46b)$$

$$R_{ps} = 6.6_{-2.5}^{+4.0} \quad , \quad (46c)$$

$$\Sigma_{tot}(R_{ps}) \equiv \Sigma_{fit}(R_{ps}) = 1.6 \quad , \quad (46d)$$

$$K_{ds} = (1.3_{-0.7}^{+1.6}) \cdot 10^{-4} \text{ m}^3/\text{kg} \quad , \quad (46e)$$

$$\Sigma_{tot}(K_{ds}[\delta a, \delta \tilde{\rho}]) = 2.2 \quad ; \quad \Sigma_{fit}(K_{ds}) = 1.5 \quad . \quad (46f)$$

⁹⁷The error is deemed to be a few percent and, hence, neglected.

⁹⁸Assuming $D_{ps} = D_{pc}$ instead of fitting B_s , would lead to $K_d = 1.8 \cdot 10^{-4} \text{ m}^3/\text{kg}$ (cf. Eq. (44b), $E_D = 1$, $F_{s,s} = F_s$). Likewise, assuming $D_{ps} = 3 D_{pc}$, according to the sodium-uranine ratio in free water (cf. App. 5, section 2), would lead to $K_d = 0.4 \cdot 10^{-4} \text{ m}^3/\text{kg}$, i. e. within the error band specified.

The following conclusion can be drawn:

1. Surface sorption is negligible. In addition, $R_f=1$ confirms the result from uranine that the water conducting zones have no infill.
2. The value for dispersivity does not deviate from that of uranine (consistent with $R_f=1$, we see no influence of surface sorption heterogeneity along the flow paths).
3. The pore diffusion coefficient D_p of sodium, derived from the fit, is only 30% higher than the value of uranine. In free water, however, the diffusion coefficient of sodium is a factor of 3 higher (cf. App. 5, section 2). The reason, that the change from uranine to sodium (with a distinctly higher mobility in free water) has only a small effect on D_p , is not clear. Model simplifications might be a possible cause.
4. A pore diffusion coefficient D_{pF} for the fault gouge region was estimated, using the diffusion coefficient in free water, the porosity from structural analysis and a formation factor derived from an empirical relationship (cf. App. 5). The numerical result reads: $D_{pF} = (2.3_{-1.3}^{+2.4}) \cdot 10^{-10} \text{ m}^2/\text{s}$.
The diffusion coefficient from the fit is a factor 7 smaller but nevertheless consistent within the errors.
5. A K_d extracted from a single porosity model matching the retardation of the peak would be about a factor 60 smaller⁹⁹.
6. The model parameters derived in a previous analysis of very early migration experiments for sodium were not consistent with the corresponding values for uranine and differ from the results presented here (cf. [5] and [3], Tab. 6-2 on p. 6-10 and Tab. 7-4 on p. 7-17). The main reasons for the improvements achieved with the present analysis are:
 - i) New information on structural analysis (not available previously).
 - ii) Revised fit procedures to determine the model parameters.
 - iii) Considerable higher quality of the experiments (improved equipment, smaller packer volumes, down hole concentration measurements and stable flow rates).

⁹⁹ $R_f = 1.8$, $\epsilon = 7.4 \cdot 10^{-3}$ (cf. Eqs. (33a) and (35a)) , $(1-\epsilon) \rho \approx 2670 \text{ kg/m}^3$ (cf. Eq. 33c) and, hence, $K_{d,s} = 2.2 \cdot 10^{-6} \text{ m}^3/\text{kg}$ (cf. App. 2, Eq. (A2.2f)). This is unrealistically small.

Parameter variations: To show the influence of the four fit parameters, breakthrough curves for varying single parameters are given.

Retardation factor: The influence of increasing R_f by factor of 2 is shown in Fig. 17 (upper part). It is very similar to the influence of (ϵa) for uranine (cf. Fig. 11, upper part). The reason is that the mass balance, Eq. (18), is affected by R_f in the same way as by $(\epsilon a)^{100}$. Enlarging surface sorption has the same effect as proportionally enlarging the cross sections of the water conducting zones.

Dispersion length: The reduction of a_L by a factor of 2, presented in Fig. 17 (lower part), changes the front similar to the case of uranine (cf. Fig. 12, upper part).

Interface flux parameter: The increase of F_s by a factor of 2, shown in Fig. 18 (upper part), increases the tail amplitude also by roughly a factor of 2, as was the case of uranine (cf. Fig. 13, upper part). The peak, however, (due to the larger outflow into the sorbing porous rock) is affected to a larger extent. In line with uranine, the effect would be the same when changing ϵ_{ps} by a factor of 2 (keeping D_{ps} and R_{ps} constant).

Tail end parameter: The increase of B_s by a factor of 2, presented in Fig. 18 (lower part), delays the beginning of the tail end perturbation from ≈ 400 h to ≈ 1200 h, leaving the rest of the breakthrough curve unchanged. The delay is only 30% smaller than the estimated value (factor of 4 according to $(B'_s)^2/B_s^2$; cf. Eq. A3.4). The effect is analogous to uranine.

4.3.3 Results and Parameter Variations for Strontium

Fitted Breakthrough Curve: The fit of the model to the experimental breakthrough curve is presented in Fig. 19 (upper part). The model is able to reproduce the experimental breakthrough curve reasonably well, though time and concentration scales differ vastly from those of uranine (cf. Fig. 10) and sodium (cf. Fig. 16). The effect of the stronger sorption, described properly by the model, shows the usefulness of the concept of bulk sorption in the porous rock zone. The fairly flat breakthrough curve differs considerably

¹⁰⁰Uranine: $\bar{v}_k' = \bar{v}_k \cdot \frac{(\epsilon a)}{(\epsilon a)'} ; \left(\frac{1}{b}\right)' = \left(\frac{1}{b}\right) \cdot \frac{(\epsilon a)}{(\epsilon a)'} ; d' \approx d ; \lambda = 0$.
Sodium: $\left(\frac{\bar{v}_k}{R_f}\right)' = \left(\frac{\bar{v}_k}{R_f}\right) \cdot \frac{R_f}{R_f'} ; \left(\frac{1}{bR_f}\right)' = \left(\frac{1}{bR_f}\right) \cdot \frac{R_f}{R_f'} ; d' = d ; \lambda = 0$.

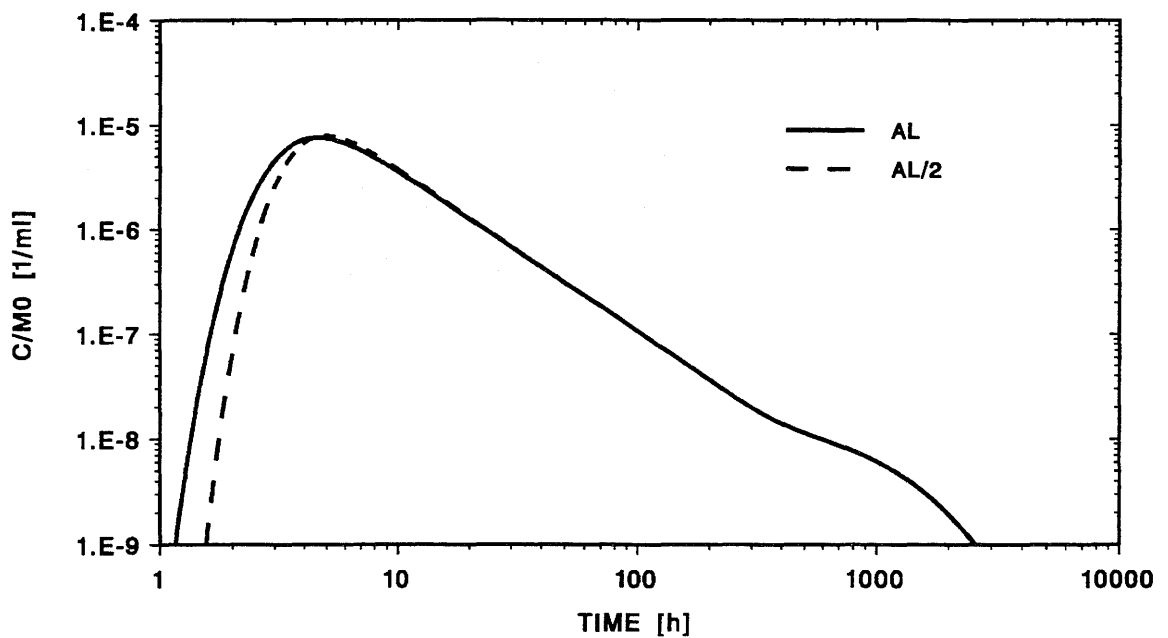
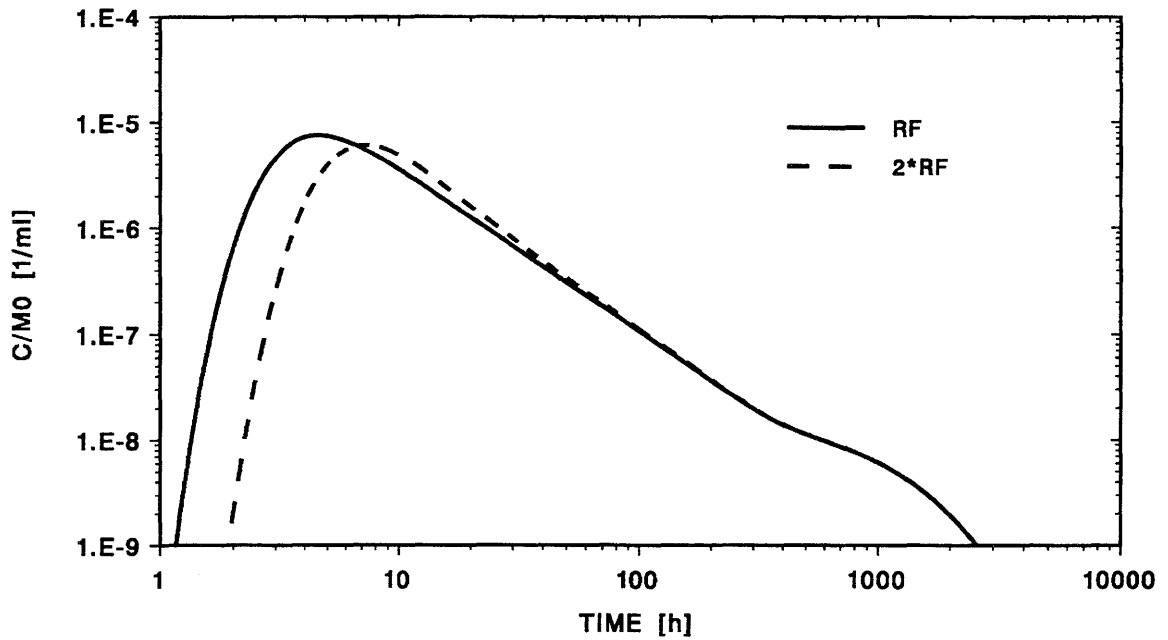


Figure 17 Influence of the retardation factor R_f and the dispersion length a_L on the breakthrough curve for sodium. Upper part: By doubling R_f the peak is delayed and reduced (from the solid to the dashed line) Lower part: For sorbing nuclides mainly the change of the front edge (from the solid to the dashed line) can be observed as a result of halving a_L .

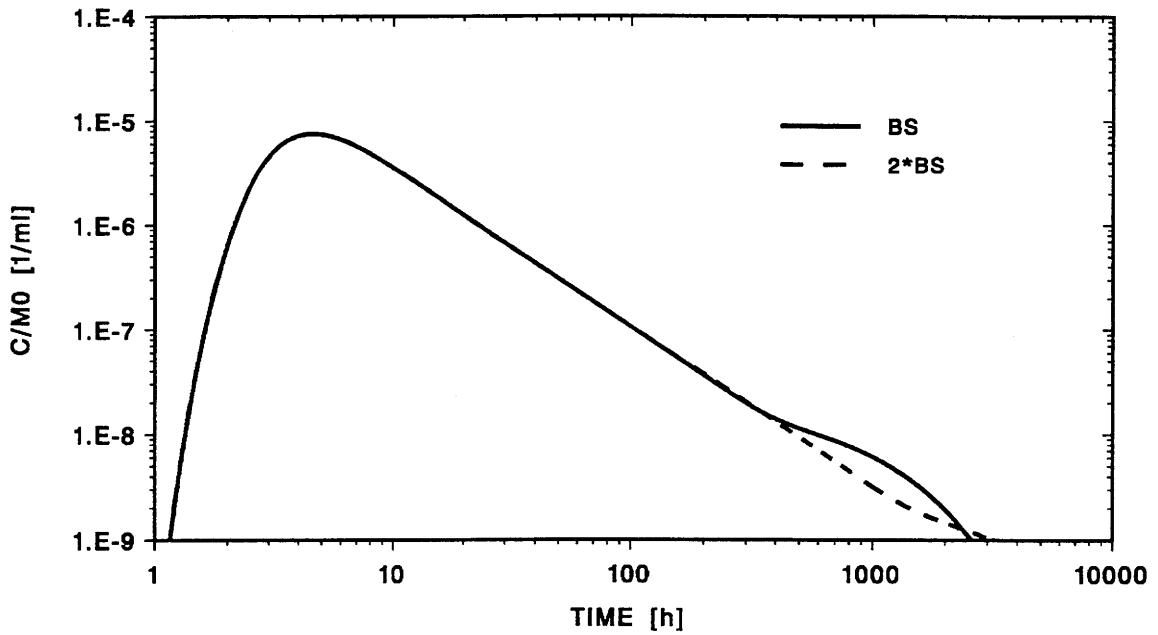
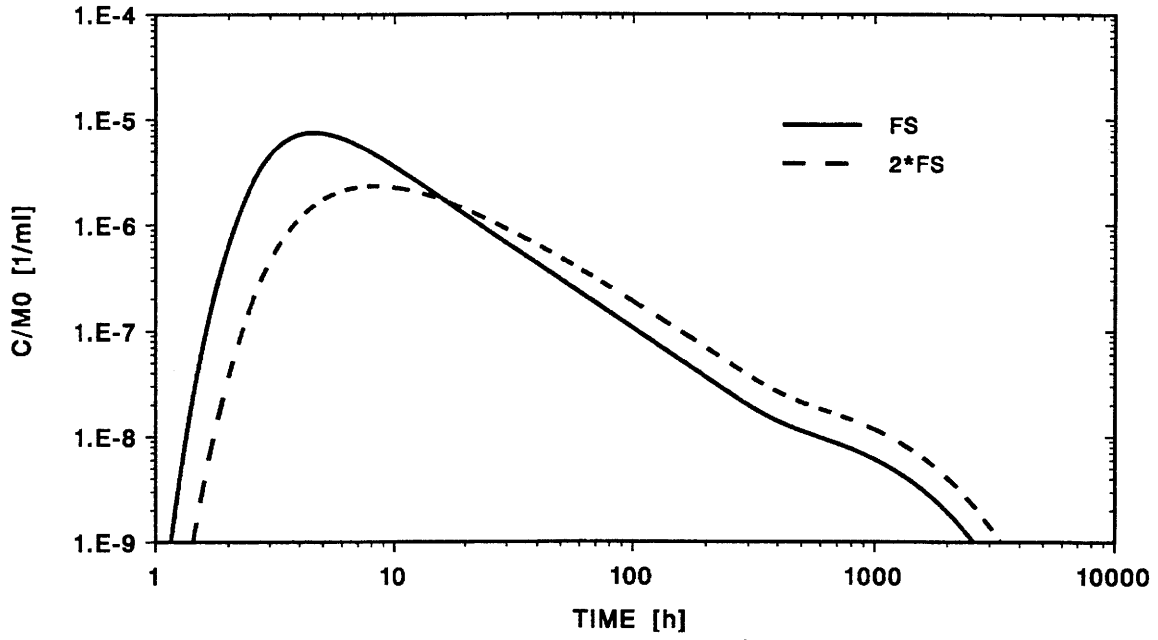


Figure 18 Influence of the interface flux parameter F_s and the tail end parameter B_s on the breakthrough curve for sodium. Upper part: Doubling F_s generates an effect similar to uranine (dashed with respect to the solid line). Lower part: Doubling B_s (dashed with respect to the solid line) demonstrates the good separation of the effects from F_s and B_s .

from the shape obtained for uranine: no narrow peak at a position around the advection time (due to the large tracer flux into the porous rock zone¹⁰¹) and no tail end perturbation (due to the longer penetration time to the plane of symmetry in the porous rock zone). The analytical guide¹⁰² (dot-dashed line) representing peak height position and tail properly, confirms the dominance of the porous rock zone effects and demonstrates the power of that approximation. Due to the large value of τ_0 , the $t^{-3/2}$ decrease (dotted line), revealing back flow from the porous rock zone at large times, is reached only asymptotically. From the above discussion it is not astonishing, that the single porosity model (dashed line), matching peak position by using an adjusted R_f , does not describe the experimental breakthrough curve¹⁰³. A summary of experimental breakthrough curve data and the deviations of the fitted model values is given in Tab. 4. With respect to uranine (Tab. 1) the peak height C_{fm}/M_0 is reduced by a factor of 250 and the peak position t_m delayed by a factor of 45.

Tab. 4 Characteristic Data of the Breakthrough Curve for Strontium

PART	CHAR. DATA	EXPERIMENT	(MOD-EXP)/EXP.
PEAK	C_{fm}/M_0	$9.60 \cdot 10^{-8} \text{ ml}^{-1}$	3 %
	t_m	150 h	- 13 %
	$s/2$	164 h	6 %
TAIL	$C_f (1500 \text{ h})/M_0$	$1.07 \cdot 10^{-8} \text{ ml}^{-1}$	34 %
TOT	Recovery (5060 h)	0.62 ± 0.09	19 %

¹⁰¹Larger bulk sorption \rightarrow steep concentration gradients in the porous rock zone are maintained longer \rightarrow the flux into the porous rock zone is so large that practically the whole tracer inventory is delayed in the porous rock zone.

¹⁰²Calculated according to Eqs. (27) to (29) and accounting for dilution (division by β).

¹⁰³From the shape of the breakthrough curve it is already clear that a reasonable fit is not possible.

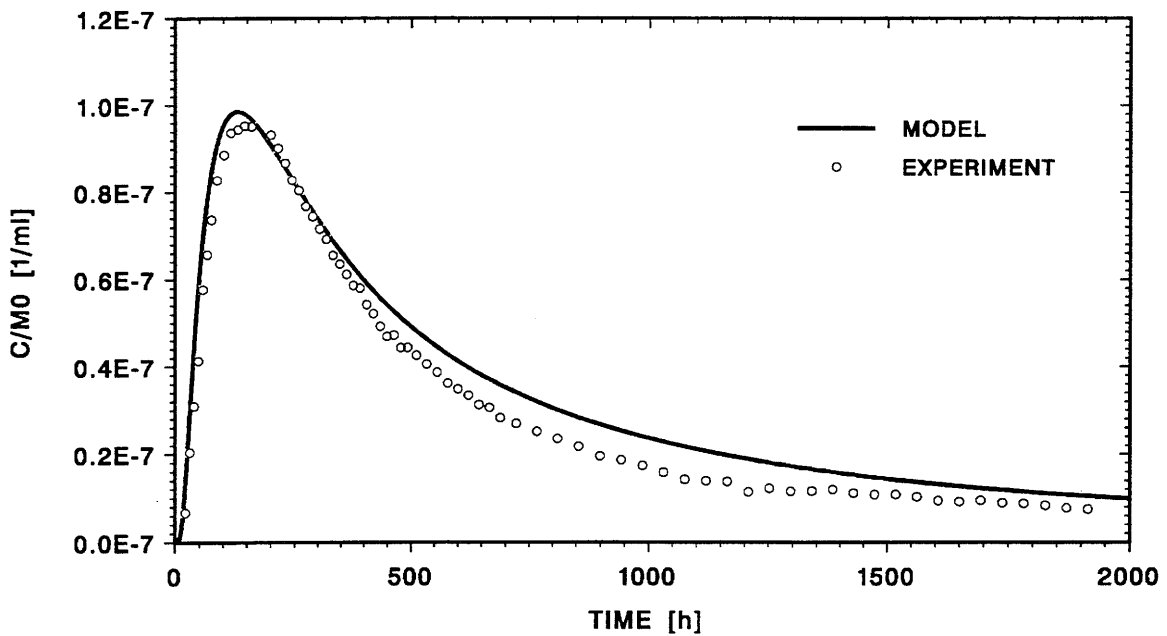
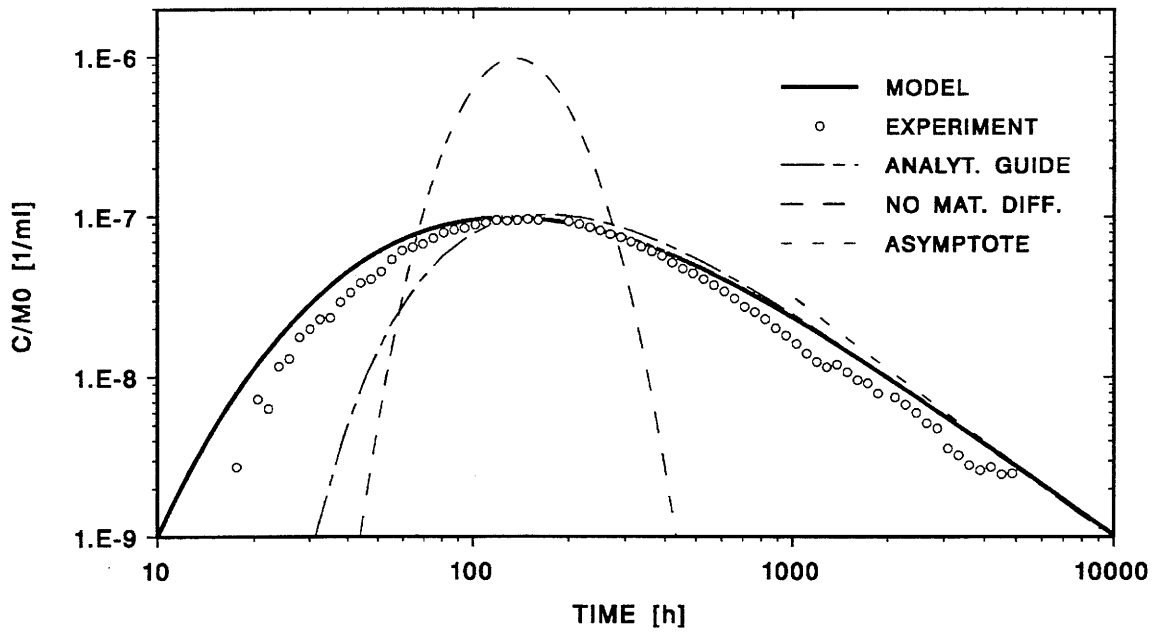


Figure 19 Breakthrough curves for strontium in the 4.9 m dipole flow field (TEST 50). Upper part: The model (solid line) produces a reasonable fit to the experiment (circles). A single porosity calculation matching the experimental peak position (dashed line) would lead to an unrealistically high peak amplitude (or an unrealistically large dispersion length). Lower part: The presentation on linear scales shows noticeable but still acceptable deviations.

This demonstrates the large effect of even a medium sorbing nuclide and confirms that, with respect to a non-sorbing nuclide, the peak height reduction is larger than the delay of peak position¹⁰⁴. The last column of Tab. 4 shows a good agreement of the peak values but substantial higher values for calculated tailing and recovery. The most probable explanation is the loss of some tracer in the experiment¹⁰⁵. Since the effect of hypothetical changes in the geometry of the water flow paths was not quantified, a possible inaccuracy of the model cannot be excluded. Nevertheless, the overall agreement of model and experiment is still reasonable.

Parameters: From the breakthrough curve the following fit parameters are obtained:

$$R_f = 1 \quad (\text{same value as for uranine}^{106}) \quad , \quad (47a)$$

$$a_L = 0.25 \text{ m} \quad (\text{same value as for uranine}^{106}) \quad , \quad (47b)$$

$$F_{ss} = (9.34_{-0.85}^{+0.93}) \cdot 10^{-6} \text{ ms}^{-1/2} \quad ; \quad \Sigma(F_{ss}) = 1.1 \quad . \quad (47c)$$

Retardation factor and sorption coefficient are derived from F_{ss} according to Eqs. (44) and the error estimates in App. 4. The required diffusion coefficient correction factor is assumed to be 1 but with an error covering possible nuclide dependent changes¹⁰⁷.

$$E_D = (1_{-0.5}^{+1}) \quad ; \quad \Sigma(E_D) = 2 \quad . \quad (48)$$

¹⁰⁴The main reason is that for uranine, t_m is determined to a large degree by the advection time \bar{t} and that the bulk sorption affects the quantity $(t_m - \bar{t})$, (cf. Eq. (28b)). Comparing $(t_m - \bar{t})$ instead of t_m , would increase the ratio of times from 45 to 210.

¹⁰⁵During the long measuring period determining the tail, some blockage problems occurred. If some parts of the water conducting channels are bypassed by the water, the tracer in the adjacent porous rock zone is trapped.

¹⁰⁶The error is deemed to be a few percent and, hence, neglected.

¹⁰⁷The reasons for assuming $E_D = 1$ (i.e. approximating D_{pss} (strontium) by D_{pc} (uranine) are: i) Relatively similar diffusion coefficients in water for strontium and uranine (cf. App. 5, section 2). ii) No correlation of D_{pc} (uranine) and D_{ps} (sodium) measured in the field to the corresponding values in the fluid continuum (cf. Eqs. (37c), (46a) and App. 5, section 2.)

We get:

$$R_{pss} = (9.08_{-5}^{+10}) \cdot 10^2 \quad , \quad (49a)$$

$$\Sigma_{tot}(R_{pss}[\delta F_D]) = 2.1 \quad ; \quad \Sigma_{fit}(R_{pss}) = 1.2 \quad , \quad (49b)$$

$$K_{dss} = (2.1_{-1.4}^{+3.8}) \cdot 10^{-2} \text{ m}^3/\text{kg} \quad , \quad (49c)$$

$$\Sigma_{tot}(K_{dss}[\delta a, \delta \tilde{\rho}, \delta E_D]) = 2.8 \quad ; \quad \Sigma_{fit}(K_{dss}) = 1.3 \quad . \quad (49d)$$

The following conclusion are drawn from these values:

1. As for sodium a negligible surface sorption is obtained, and it is confirmed that water conducting zones are without infill.
2. Again, the value of dispersivity does not deviate from that of uranine.
3. The effect of finite matrix depth on breakthrough is expected at times of $t_{dss} \approx 4 \cdot 10^5 \text{ h}^{108}$ or later, which is beyond the measuring interval of $5 \cdot 10^3 \text{ h}$.
4. A K_d extracted from a single porosity model by matching the retardation of the peak, would be about a factor of 130 smaller¹⁰⁹.

Parameter variations: To show the influence of the three fit parameters, breakthrough curves for varying single parameters are given:

Retardation factor: The influence of increasing R_f by a factor of 2 is exhibited in Fig. 20 (upper part). The effect is small since surface sorption delays only advection which is fast compared to the matrix diffusion dominated nuclide transport (due to the large bulk sorption in the porous rock zone).

¹⁰⁸ $t_{dss} \approx d^2 R_{pss}/D_{pss}$ (cf. Eqs. (A3.3d), (A3.4) and (37c), (37g), (49a)).

¹⁰⁹ $R_f = 57$, $\epsilon = 7.4 \cdot 10^{-3}$, $(1-\epsilon)\rho \approx 2670$, and hence, $K_{d,s} = 1.6 \cdot 10^{-4} \text{ m}^3/\text{kg}$ (cf. App. 2, Eq. (A2.2f)). This is unrealistically small.

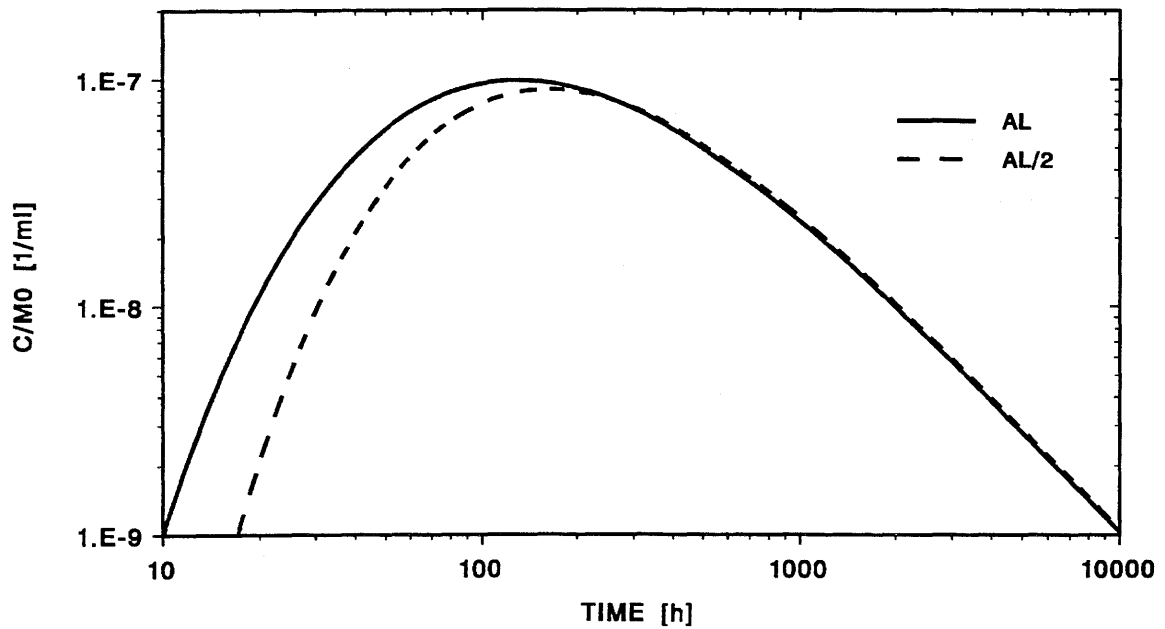
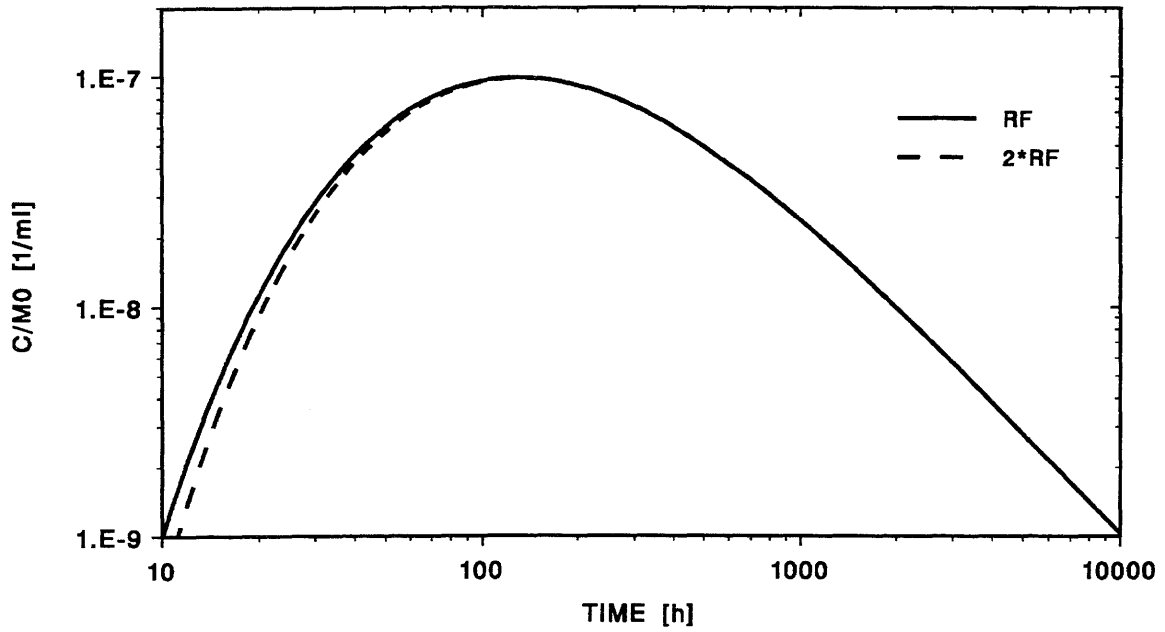


Figure 20 Influence of the retardation factor R_f and the dispersion length a_L on the breakthrough curve for strontium. Upper part: Doubling R_f generates only a small effect (dashed with respect to solid line). The reason is the dominant bulk sorption of the porous rock zone. Lower part: Halving a_L generates still a noticeable effect since the influence of dispersion is increased by matrix diffusion (dashed with respect to solid line).

Dispersion length: The influence of decreasing a_L by a factor of 2 is presented in Fig. 20 (lower part). Similarly to R_f , it affects the front edge of the breakthrough curve, but the effect is larger. The reason is that the velocities of the nuclides contributing to the front edge are reduced by a decrease of dispersion¹¹⁰. Consequently the delay due to matrix diffusion is increased¹¹¹.

It is instructive to compare the effects of changing R_f and a_L to those for sodium (Fig. 17) where the influence of matrix diffusion is considerably smaller. In the rising part of the breakthrough curve, the relative change of early arrival is small for a change in R_f for strontium and large for sodium, and vice versa for a change in a_L .

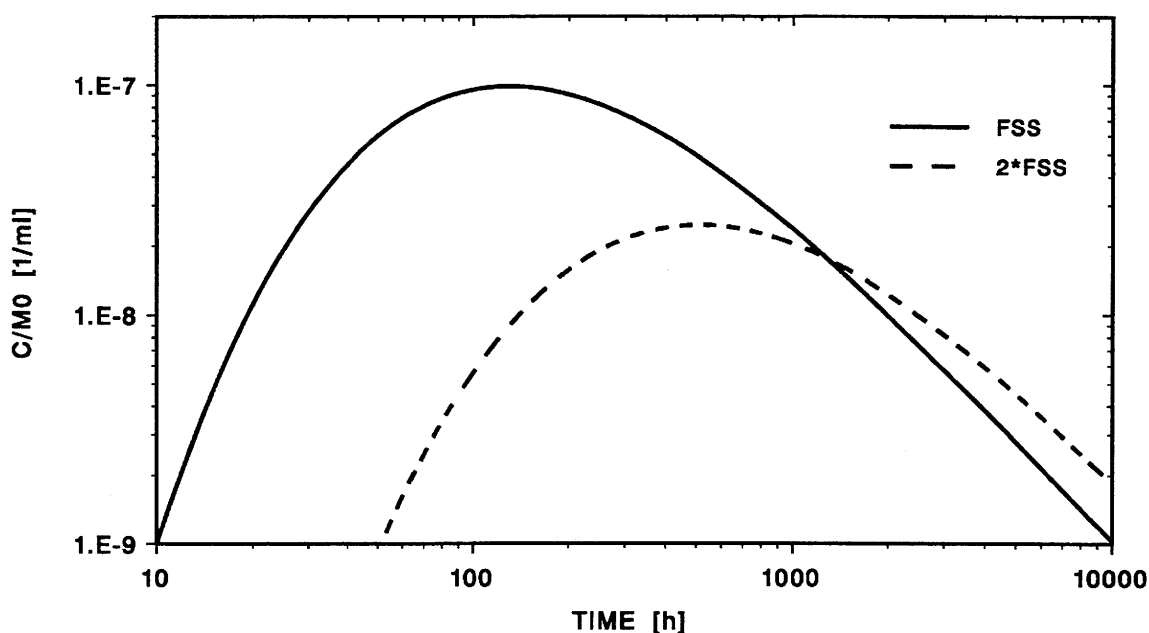


Figure 21 Influence of the interface flux parameter F_{ss} on the breakthrough curve for strontium. The large effect when doubling F_{ss} reflects the dominance of the bulk sorption in the porous rock zone.

¹¹⁰As described by Ficks's law.

¹¹¹Smaller nuclide velocities \rightarrow longer contact times of the nuclides in the water conducting zones to the pore surfaces of the porous rock zone \rightarrow larger matrix diffusion effects. This is different to an increase of R_f not increasing nuclide contact times with the pore surfaces.

Interface flux parameter: The influence of an increase of F_{ss} by a factor of 2 is shown in Fig. 21. For strontium, diffusion into the porous rock zone is dominant. Therefore, F_{ss} determines to a large extent the breakthrough curve. So, an increase of F_{ss} by a factor of 2 reduces peak height by a factor of 4, enlarges peak time by a factor of 4, and increases tail amplitude by a factor of 2. This behaviour can be fully explained by the changes in τ_0 (cf. Eqs. (27f), (28a), (28b) and (29)). In addition, the shape of the breakthrough curve is almost unchanged rendering predictions fairly easy. As for the other tracers, an increase of ϵ_{pss} (keeping D_{pss} and R_{pss} constant) would produce the same effect¹¹².

4.3.4 Comparison of Sorption Coefficients

The Grimsel migration field experiments have been complemented by a rather extensive laboratory programme (cf. Ref. [3], chapter 5 and section 7.2). Field experiments should be paralleled with laboratory investigations since information from the field is never sufficiently comprehensive for a clear discrimination between various models. In the field, boundary conditions are poorly known, and parameters cannot be freely varied; measurements are time consuming and expensive and, hence, in general only few point measurements are available. In the laboratory, geometrical structures on a small scale can be explored and important processes can be examined in well defined experiments. The second is especially true for the sorption mechanisms. From various experiments, sorption coefficients for the porous rock zone of the migration fracture were deduced. The complementary experiments can be characterised as follows:

1. In the **rock water interaction experiments** (cf. Ref. [18]), small samples of loosely disaggregated¹¹³ Grimsel mylonite were contacted with ground water and the time dependent changes of water composition measured. The measurements were performed for a whole series of different water chemistry parameters. The results showed that the dominant mechanism for sorption of sodium and strontium in the different water-mylonite systems is cation exchange. Based on a cation exchange model, selectivity coefficients for the exchange of Na^+ and Sr^{++} with the dominant cation Ca^{++}

¹¹²Pay attention - a change of ϵ_{pss} , keeping D_{pss} and K_{dss} instead of R_{pss} constant, would reduce the effect (for strontium $R_{pss} \sim K_{dss}/\epsilon_{pss}$ (cf. Eqs. (21b) and (27f)).

¹¹³“Loosely disaggregated” means gently crushed to particles < 2 mm.

were determined (which are insensitive in a large range of water chemistry data). Using these values and the compositions of natural Grimsel water, fractional cation occupancies for Na^+ and Sr^{++} on mylonite were calculated. The cation exchange capacity CEC for mylonite was measured applying the silver-thiourea (AgTU) method. Sorption coefficients $K_d(\text{tracer})$ for tracers in natural Grimsel water sorbing on mylonite were then derived from CEC and fractional occupancies. These sorption coefficients were extrapolated to the mineralogy in the migration zone according to App. 6.

2. In the **batch sorption experiments** (cf. Ref. [15]), small samples of crushed Grimsel mylonite ($< 63\mu\text{m}$ and $< 250\mu\text{m}$) were conditioned with natural Grimsel water and subsequently exposed to solutions of radiotracers (carrier free ^{22}Na and ^{85}Sr ; cf. Ref. [15], p. 10) in Grimsel water. The radiotracer activities in the solutions were measured until steady state conditions were reached, yielding also sorption coefficients $K_d(\text{radiotracer})$. They were also extrapolated to the mineralogy in the field, according to App.6. Crushing mylonite creates new surfaces, and such values might not be directly applicable to a field situation. Therefore a second extrapolation from the rock fraction $< 250\mu\text{m}$ to the sample “loosely disaggregated” was applied, using corresponding CEC values as described in App. 6.

The experiments were complemented by measurements of CEC and fractional occupancies (silver-thiourea method), from which the values of $K_d(\text{tracer})$ were derived according to a cation exchange model. These complementary K_d values agree in general with the direct batch measurements. It is worth noting that the agreement of the sorption coefficients, measured on the one hand with carrier free radiotracers at low concentrations¹¹⁴ and on the other hand by the silver-thiourea method¹¹⁵, is an indication for a negligible effect of isotopic exchange compared to cation exchange. The reason is, that the cation exchange reactions generate linear¹¹⁶ isotherms¹¹⁷.

3. In the **dynamic infiltration experiments** (cf. Ref. [19]), natural Grimsel water is forced by high pressure through small¹¹⁸ bore cores consisting of fractured granodiorite from the Grimsel Test Site. Breakthrough curves from nuclide tracer pulses

¹¹⁴ $C \ll C_{nat}$ and, therefore, the maximum influence of isotopic exchange.

¹¹⁵determining the effect of cation exchange.

¹¹⁶The reason for the linear isotherms are, according to the equations and numerical values in Ref. ([18], p. 50-59), constant selectivity coefficients, and sufficiently small concentrations of Sr^{++} and Na^+ with respect to Ca^{++} concentration in the natural Grimsel water (Sr^{++} concentration a factor 70 smaller and Na^+ concentration only a factor 5 larger).

¹¹⁷Fig. 7 shows directly that for small tracer concentrations isotopic exchange (represented by the vector S_{nat}/C_{nat}) and cation exchange (represented by the vector K) would lead to the same sorption coefficient if the isotherm would be linear.

¹¹⁸Diameter 4.6 cm and length ≈ 4 cm.

injected into the infiltration water were measured. A sorption coefficient for sodium was extracted from these dynamic experiments, in a similar approach to the present one.

4. The **hydrogeochemical equilibrium experiment** (cf. Ref. [20]) uses the same fracture and a similar dipole flow field as the migration field experiments. Instead of breakthrough curves from nuclide tracer pulses, the integral response to a step change in chemical composition¹¹⁹ of the injected water was analysed. From the changes in major constituents an in-situ cation exchange capacity (CEC) for the pore matrix (\approx fault gouge) was determined, using an ion exchange model and an estimate of total mass of pore matrix accessed by the injected water. The sorption coefficients for the different nuclides were derived from the cation exchange capacity using selectivity coefficients determined in the laboratory rock water interaction experiment.

The sorption coefficients from the complementary experiments and the migration field measurement (last line), are listed in Tab. 5. They show the following features:

1. The results of the rock water experiments agree with the migration field measurements within experimental errors and within a factor of 3. Such an agreement might not be expected in general. In our case, sorption in the field mainly takes place on fault gouge generated by natural friction during brittle deformation of mylonite. In the laboratory gently crushed mylonitic material was investigated. It appears quite plausible that the geological processes which have generated the fault gouge can be simulated by the laboratory procedures preparing the rock samples, and therefore leading to a similar average granulometry and mineralogy. This explains qualitatively the good agreement between the laboratory and the field measurements and demonstrates the possibility of reasonable extrapolations from laboratory to in-situ sorption coefficients in cases where geological processes have grinded the rock zones of interest.

¹¹⁹Groundwater from a different place with slightly different composition.

Tab. 5 Comparison of Sorption Coefficients from Different Experiments

EXPERIMENT		K_d [10^{-3} m ³ /kg]	
		Na	Sr
LABORATORY	ROCK WATER INTERACTION (loosely dis.) ^{a)}	$0.13^{+0.13}_{-0.02}$	$7.6^{+8.2}_{-1.7}$
	BATCH SORPTION (< 63 μm) ^{a)}	$1.3^{+1.5}_{-0.4}$	41^{+39}_{-4}
	BATCH SORPTION (< 250 μm) ^{a)}	$0.85^{+0.76}_{-0.04}$	25^{+22}_{-1}
	BATCH SORPTION (loosely disaggregated) ^{a)}	$0.43^{+0.60}_{-0.02}$	13^{+19}_{-1}
	DYNAMIC INFILTRATION	(0.1 - 0.3)	b)
FIELD	HYDROGEOCHEMICAL	$0.21^{+0.2}_{-0.1}$	7.8^{+8}_{-5}
	MIGRATION	$0.13^{+0.16}_{-0.07}$	21^{+38}_{-14}

a) compare App. 6, Tab. A6.1

b) not measured

2. The different K_d values from the batch sorption experiments quantify the effect of grinding the mylonite to smaller fractions. We observe $K_d(< 63 \mu\text{m})/K_d(< 250 \mu\text{m}) \approx 1.5$. This is considerably smaller than the factor of 4 calculated for the change of surface to volume ratio of small spheres. The reasons are fractions being defined by the upper bound of the diameter (imposed by the sieve mesh) and internal surfaces. The fraction dependence of K_d shows that sample preparation is important, but also that the influence of particle size is considerably smaller than calculated from pure geometrical considerations. This observation is confirmed by recent surface area measurements where preliminary results are indicating a maximum reduction factor of only 5 to 7 for the transfer of sorption values from crushed (< 63 μm) to intact (≈ 1 cm) Grimsel rock samples (cf. Ref. [21] p. 12). For the K_d comparison, the values corresponding to the loosely disaggregated rock samples are considered. As in the case of the rock water interaction experiments, we observe an almost similar good agreement, for Na, however, needing a factor of Σ^2 to cover the difference to the laboratory experiments¹²⁰.

¹²⁰The limits of a log-normal distribution defined by the factor Σ^2 correspond to the limits of a Gauss distribution defined by 2 standard deviations (cf. Eq. (A4.1d)).

3. In the dynamic infiltration experiments the paths of advective solute transport are largely unknown. Possibilities are parts of the grain boundary network of the granodiorite, the total grain boundary network, the small fracture or any combination. The large R_f values and the small effect of matrix diffusion for sodium in these experiments indicate a substantial contribution of advective network flow to the Na breakthrough¹²¹. This is different to the migration field experiments where advective nuclide transport mainly takes place in narrow water conducting channels within the fault gouge. The infiltration experiments represent nuclide transport through different flow paths but in a similar mineralogical environment. They do not necessarily approximate the situation of the field migration experiments sufficiently well, but on the other hand the results are surprisingly similar.
4. The results of the hydrogeochemical experiments confirm the general trend.
5. From the different categories of experiments, the following sorption coefficient ratios $K_d(\text{strontium})/K_d(\text{sodium})$ were obtained:
 - i) 60 for the rock water interaction experiments,
 - ii) 30 for the batch sorption experiments,
 - iii) 40 for the hydrogeochemical experiment,
 - iv) 160 for the migration field experiments.

The ratio from the migration field experiments is roughly a factor of Σ_{fit+E_D} ¹²² higher than the ratio from the rock water interaction experiments and a factor of $\Sigma_{fit+E_D}^2$ than that from the batch sorption experiments, showing a noticeable effect covered to a large extent by the experimental errors. The reason that the hydrogeochemical experiment, performed in the field, support the laboratory results is that the sorption coefficient ratio is governed by the selectivity coefficients taken over from the laboratory rock water interaction experiment¹²³. A qualitative explanation of the higher $K_d(\text{strontium})/K_d(\text{sodium})$ ratio from the migration field experiments is the smaller penetration depth of strontium with respect to sodium, locating the strontium sorption in the fault gouge nearer to the water channels¹²⁴. Somewhat different sorption prop-

¹²¹It was criticized that the results of one of the two bore cores were rejected according to a flat merit function (which was a consequence of the small matrix diffusion effect). Interpreting the corresponding R_f as a single porosity retardation factor (representing the network flow) would lead to a $K_d \approx 1 \cdot 10^{-4} \text{ m}^3/\text{kg}$ which is in line with the stated results. [According to private communication from P. Smith].

¹²²The geometric standard deviation of this ratio is estimated taking into account only fitting errors and the contribution from the E_D correction for strontium (cf. Eqs. (44b), (46f), (48) and (49d)). The numerical value reads $\Sigma_{fit+E_D}(K_d(\text{strontium})/K_d(\text{sodium})) = 2.3$.

¹²³The reason, that the ratio does not correspond exactly to the value of the rock water interaction experiments, are different rounding procedures.

¹²⁴and therefore to a region of potentially more intensive alterations.

erties of the fault gouge with respect to the mylonitic laboratory samples might also be a possible reason for the higher sorption of strontium in the field (e.g. higher smectite content). Considering the large errors, we should not overstress this difference.

6. Summarizing, we can say that the agreement of the complementary experiments with the migration field experiments is good (within a factor of 3 as well as within a factor of $< \Sigma_{tot}^2$ of the field results). It demonstrates that for nuclides sorbing rapidly¹²⁵, not too strongly, linearly, and exhibiting a reversible cation exchange process on fault gouge, laboratory experiments can reasonably well be extrapolated to field conditions, provided adequate care is taken in selecting and preparing the rock samples.

4.4 Summary of Physical Parameters

To facilitate the overview, physical parameters fixed in advance and derived from the migration experiments are summarized in Tab. 6. The reasonable magnitudes of the derived numerical values are an additional indication that we do see really matrix diffusion effects, as has been discussed in the previous sections.

¹²⁵i.e. rapid surface reaction kinetics (in addition to diffusion) with respect to the time scales of the field experiments.

Tab. 6 Physical Parameters

STRUCTURAL GEOLOGY	FIXED IN ADVANCE	$a = (5 \pm 2.5) \cdot 10^{-2} m$ $n = 4 \pm 1$ $\tilde{\rho}_p = (2670 \pm 200) kg / m^3$
BREAKTHROUGH OF CONSERVATIVE URANINE	CALIBRATION	$2b = (9.3 \pm 4.6 / 3.0) \cdot 10^{-5} m^*$ $\epsilon_p = (6.2 \pm 6.8 / 3.2) \cdot 10^{-2}$
	NUCLIDE SPECIFIC RESULTS	$a_L = (2.5 \pm 0.5 / 0.4) \cdot 10^{-1} m$ $D_p = (2.5 \pm 11 / 2) \cdot 10^{-11} m^2 / s$
BREAKTHROUGH OF WEAKLY SORBING SODIUM	NUCLIDE SPECIFIC RESULTS	$R_f = 1$ $a_L = \text{unchanged}$ $D_p = (3.3 \pm 14 / 2.7) \cdot 10^{-11} m^2 / s$ $K_d = (1.3 \pm 1.6 / 0.7) \cdot 10^{-4} m^3 / kg$
BREAKTHROUGH OF STRONGER SORBING STRONTIUM	NUCLIDE SPECIFIC RESULTS	$R_f = 1$ $a_L = \text{unchanged}$ $K_d = (2.1 \pm 3.8 / 1.4) \cdot 10^{-2} m^3 / kg$

*) The corresponding flow porosity (with respect to the migration zone width a)

reads: $\epsilon = 2bn/a = (\epsilon a)/a = (7.4^{+7.4}_{-3.7}) \cdot 10^{-3}$,

$\Sigma_{fit}(\epsilon) = \Sigma(\epsilon a) = 1.05, \Sigma_{tot}(\epsilon) \approx \Sigma(a) = 2.$

5 Predictions of Breakthrough Curves for a Smaller Dipole Flow Field

Having carried out and evaluated the 4.9 m dipole experiments, further tests with a 1.7 m dipole field were planned. This gave the possibility to make predictions in advance and to test them. These predictions were done using the data derived from the 4.9 m dipole experiments (section 4.4). The injection distributions measured in the small flow field experiments, as shown in Fig. 22 ¹²⁶, were used as up-stream boundary conditions. A noticeable change of uranine breakthrough was observed¹²⁷ for the different migration experiments in the 1.7 m dipole, which is interpreted as the consequences of washing out fault gouge, especially due to the high water velocities of the small dipole flow field. To minimize the influence of such fracture geometry changes, the very first experiments in the 1.7 m dipole were used for predictions.

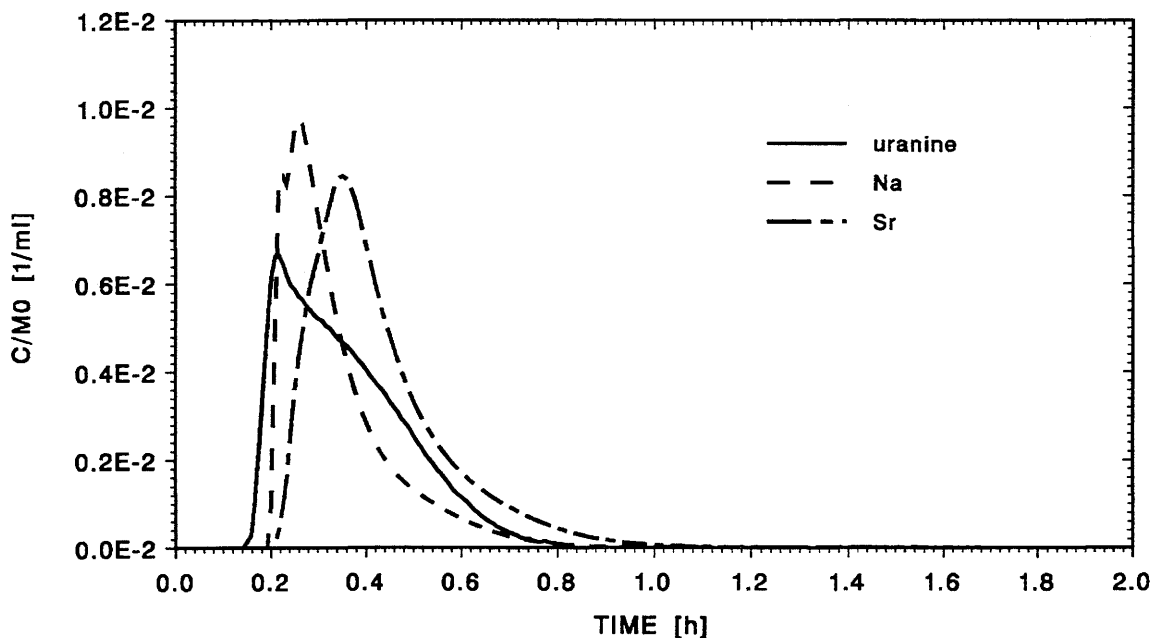


Figure 22 Injection distributions measured down hole for the different experiments in the 1.7 m dipole flow field.

¹²⁶The deviations from the injection distributions for the 4.9 m dipole experiments (cf. Fig. 9) are due to a shorter injection tubing, slightly different pumping rates and a changed injection procedure.

¹²⁷Reduction of tail amplitude and of the position in time of the tail end perturbation.

These are:

- i) Uranine: $Q_i = 9.3$ ml/min, $Q_w = 150$ ml/min, $\beta = 16.1$, (TEST 52).
- ii) Sodium: $Q_i = 10$ ml/min, $Q_w = 148$ ml/min, $\beta = 14.8$, (TEST 61).
- iii) Strontium: $Q_i = 8$ ml/min, $Q_w = 120$ ml/min, $\beta = 15.0$, (TEST 66).

The predictions without any parameter adjustments are compared to the new experiments in Fig. 23.

For the **non-sorbing uranine** we observe the following features:

- The overall agreement is excellent. The model describes the main processes adequately. Apparently, the parameters extracted from the large dipole region are also valid for the smaller dipole region¹²⁸. Since a possible variability of fracture parameters does not become noticeable, the comparison is a sensitive test of model response to a changed flow field.
- The shape of the breakthrough curve shows similar features as in the 4.9 m dipole experiment: an advection-dispersion dominated peak and a tail generated by matrix diffusion (cf. Fig. 10). Compared to the larger dipole, the peak exhibits an increased height as well as a decreased position in time and the tail a reduced amplitude, as expected.
- It is possible to estimate the main changes of the breakthrough curve generated by the reduction of the dipole length L_0 from 4.9 m to 1.7 m, taking into account the following proportionalities:

$L_k \sim L_0$ Stream tube length, (cf. Eq. (12e)),

$\bar{t}_k \sim L_0^2$ Advection time within stream tube, (cf. Eq. (13c)),

$\bar{v}_k \sim \frac{1}{L_0}$ Average velocity within stream tube, (cf. Eq. (14b)),

$B_k \sim L_0$ Average stream tube depth, (cf. Eq. (16c)),

$\tau_0 \sim L_0^4$ Matrix diffusion parameter, (cf. Eq. (27f), using $z/\bar{v} = \bar{t}_k$) !,

$\sigma \sim \sqrt{L_0}$ Width parameter of dispersion (cf. Eq. (A2.3e); $\bar{z}=L_k$),

and using:

$$\frac{L_0(1.7m \text{ dipole})}{L_0(4.9m \text{ dipole})} = 0.35 \quad .$$

¹²⁸The reasons why interpretation is not complicated by fracture heterogeneity are: i) overlapping flow fields (cf. App. 7, Fig. A7.1); ii) selection of the appropriate bore hole combinations by the experimenters; iii) a bit of luck.

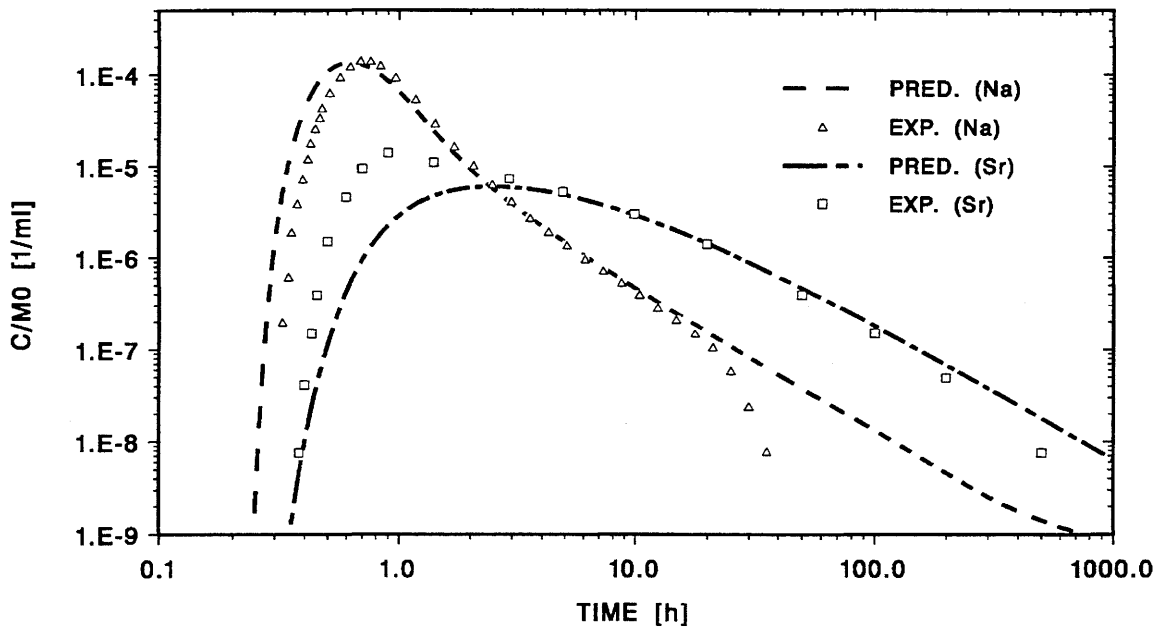
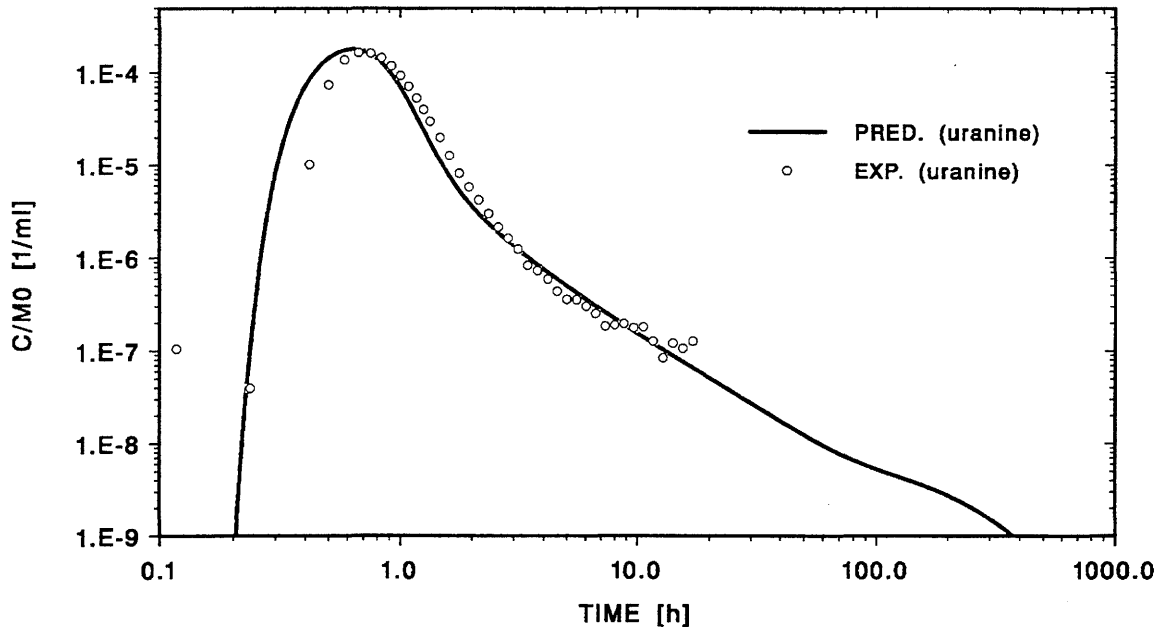


Figure 23 Model predictions and experiments for the 1.7 m flow field. Upper part: For uranine the agreement of the model (solid line) with the experiment (circles) is good. Lower part: The agreement for the sorbing sodium (Na, dashed line and triangles) and strontium (Sr, dot-dashed line and squares) indicates that the model describes the main transport processes adequately.

- The peak height, $C_{fm}/M_0 = 1.7 \cdot 10^{-4} \text{ ml}^{-1}$, is a factor of 7 larger than in the 4.9 m dipole. The large reduction of an already small¹²⁹ τ_0 demonstrates that, in the 1.7 m dipole field, the peak is not noticeably influenced by matrix diffusion¹³⁰. For the total peak height we obtain the following partial contributions:

i) Negligible influence of matrix diffusion \rightarrow factor ≈ 2.2 ,

ii) Smaller dilution due to the smaller depths B_k of the stream tubes:

$$C_{fm} \sim \frac{1}{B_k} \sim \frac{1}{L_0} \rightarrow \text{factor} \approx 2.8,$$

iii) Smaller dispersion due to the smaller lengths L_k of the stream tubes:

$$C_{fm} \sim \frac{1}{\sigma(L_k)} \sim \frac{1}{\sqrt{L_k}} \sim \frac{1}{\sqrt{L_0}} \rightarrow \text{factor} \approx 1.7 \quad .$$

These estimated contributions add up to a factor of 10, being only 30% larger than the exact calculation¹³¹.

- The peak width $s = 0.44 \text{ h}$ is a factor 4.5 smaller than in the 4.9 m dipole. This can directly be understood by the following proportionality:

$$s(L_k) \sim \frac{\sigma(L_k)}{\bar{v}_k} \sim L_0^{3/2} \rightarrow \text{factor} 4.7, \text{ being only 4\% larger than the exact calculation.}$$

- The peak position $t_m = 0.70 \text{ h}$, being considerably smaller than for the 4.9 m dipole, is mainly given by the smaller advection time \bar{t} ¹³².

$$\bar{t} \approx [t_m - t(\text{INJ})] \sim L_0^2 \quad .$$

With this relation we would estimate a value of $t_m = 0.6 \text{ h}$ for the 1.7 m dipole¹³³ which is only 14% smaller than the exact calculation (4.9 m dipole, $t_m = 3.3 \text{ h}$).

- The tail amplitude, $C_f(t=20 \text{ h}) = 5 \cdot 10^{-8} \text{ ml}^{-1}$, is a factor of 10 smaller than for the 4.9 m dipole experiment. This is attributed to the smaller τ_0 .

$$\frac{C_f(t=20h)}{M_0} \sim \sqrt{\tau_0} \sim L_0^2 \rightarrow \text{factor of 8, being 20\% smaller than the exact calculation.}$$

- The tail end perturbation is expected roughly for the same time as in the 4.9 m dipole experiment¹³⁴ as indicated by the model in Fig. 23 (upper part). It is clearly well below the detection limit.

¹²⁹ τ_0 (4.9 m dipole) = 0.28 h

¹³⁰Peak height C_{fm} , width s , and position t_m can therefore be approximated by the expressions in App. 2.

¹³¹An improved estimate would have to consider the injection distribution, the precise injection and withdrawal rates, and the influence of the boundaries (since the Peclet number is only 6.8 for the small dipole).

¹³²The influence of dispersion and matrix diffusion are of minor importance ($|\Delta t| \leq 0.2 \text{ h}$) and partially cancel each other.

¹³³The delays $t(\text{INJ})$ due to the injection distributions are approximated for the two dipole experiments as follows; $t(\text{INJ}, 4.9 \text{ m}) \approx 0.6 \text{ h}$ and $t(\text{INJ}, 1.7 \text{ m}) \approx 0.3 \text{ h}$.

¹³⁴Compare App.3 (comment 3).

For the **weakly sorbing sodium** a similar behaviour as for uranine was obtained; the agreement between prediction and experiment is excellent.

For the **stronger sorbing strontium**, exhibiting a very large difference of breakthrough between the 4.9 m and the 1.7 m dipole, the following observations can be noted:

- The overall agreement is reasonable. The experimental value of peak height, $C_{fm}/M_0 = 1.4 \cdot 10^{-5} \text{ ml}^{-1}$, is a factor 2.3 higher and that of peak position, $t_m = 0.9 \text{ h}$, a factor 2.7 smaller than the prediction. The tail agrees quite nicely. Noteworthy is the almost correct prediction of a dramatic change in numerical values (for the 4.9 m dipole: $C_{fm}/M_0 = 9.6 \cdot 10^{-8} \text{ ml}^{-1}$, $t_m = 150 \text{ h}$).
- The general shape of the breakthrough curve for times larger than 20 h is characteristic for matrix diffusion controlled transport (long $t^{-3/2}$ drop). In contrast to the 4.9 m dipole, however, we observe a noticeable steeper and higher experimental peak. Based on caesium experiments not yet fully evaluated, we feel that an influence of sorption kinetics (in addition to matrix diffusion) might turn up in the peak region (cf. Ref. [22], Fig. 6).
- The theoretical breakthrough curve data can reasonably be extrapolated from the 4.9 m dipole values with the analytical expressions for advection and matrix diffusion (section 3.2.5). We have to apply the following relations ¹³⁵:

$$\frac{C_{fm}}{M_0} \sim \frac{1}{\tau_0} \sim \frac{1}{L_0^4} \longrightarrow \text{factor } 63 \quad ,$$

$$t_m(1.7, \text{Sr}) \approx t_m(1.7, \text{uranine}) + t_m(4.9, \text{Sr}) \cdot \left(\frac{L_0(1.7)}{L_0(4.9)}\right)^4 = 3.1 \text{ h} \quad .$$

The corresponding values of the numerical calculations are $C_{fm}(1.7)/C_{fm}(4.9) = 60$ and $t_m = 2.3 \text{ h}$, demonstrating the validity of the analytical estimate.

¹³⁵The relation for $t_m(1.7, \text{Sr})$ is derived under the following assumptions:

$$t_m(4.9, \text{Sr}) = 150 \text{ h} \approx \frac{2}{3} \tau_0(4.9, \text{Sr})$$

$$t_m(1.7, \text{uranine}) = 0.7 \text{ h} \approx \bar{t} + t(\text{INJ}) \text{ (neglecting } \Delta t(\text{disp}) \text{ and } \Delta t(\text{matrix diffusion, uranine}).$$

6 Conclusions

A description of the conceptual and the mathematical model was presented. In addition simple analytical expressions to guide interpretation of the results were given. The model was applied to a few selected tracer migration experiments. The non-sorbing tracer uranine and the simple cation-exchanging radiotracers $^{22,24}\text{Na}^+$ (weakly sorbing) as well as $^{85}\text{Sr}^{++}$ (more strongly sorbing) were investigated. Physical parameters were extracted from best-fit breakthrough curves and compared to data from independent measurements. Predictions for breakthrough in a different flow field were made and compared to subsequent experiments. A summary of the work is reported in Ref. [24]. Comprehensive experimental information is given in Refs. [3] and [4]. The following conclusions can be drawn:

1. Modelling of different migration field experiments with various tracers yielded a coherent picture. Nuclide transport can be described by advective-dispersive flow within a few interconnected narrow but transmissive water conducting zones and matrix diffusion into stagnant water of adjacent porous rock zones. (The porous rock zones represent to a large extent fault gouge).
2. Although the model is a highly simplified representation of a rather complex natural system, it is able to describe the experimental breakthrough curves with a large degree of accuracy. No new process had to be invoked. Having only a small number of fit parameters leading to physical parameters (b , a_L , D_p , ϵ_p or K_d) to a large extent consistent with independently obtained values, this is a strong indication that the model contains the relevant mechanisms governing tracer transport.
3. Matrix diffusion not limited by a boundary is manifest through the tail of the breakthrough curve decreasing with $t^{-3/2}$. Such a tail is seen in all experimental breakthrough curves. The deviation from the $t^{-3/2}$ law at the end of the tail, also observed in the experiments (for uranine and sodium) shows that the diffusion process is restricted by the small depth of the porous rock zone.
4. In order to clearly discriminate, in the tail, the effects of matrix diffusion from those of the varying velocities in a dipole field, extraction rate should exceed injection rate by at least a factor of 3.
5. Separate determination of ϵ_p and D_p for a conservative tracer or D_p and K_d for a weakly sorbing tracer is possible only if the breakthrough curve is measured down to the dipping tail end. This requires unusual experimental effort - in our case breakthrough

curves measured accurately up to 3 orders of magnitude longer than the peak time and to concentrations, 4 orders of magnitude smaller than the peak concentration.

6. Our model, requiring water flow in narrow water conducting zones within the fault gouge to describe the experiments, complements the geological investigations. From these it is not clear whether nuclide transport takes place mainly homogeneously or heterogeneously within the fault gouge¹³⁶.
7. From the experiments with sorbing tracers, retardation factors $R_f=1$ are derived for the transport in the water conducting zones. It reflects negligible surface sorption and in addition confirms the result of the non-sorbing tracer, where the water conducting zones do not show the effect of an infill.
8. No tracer dependent dispersion lengths were observed (which is consistent with $R_f=1$).
9. The errors of physical parameters (ϵ_p , D_p , b , d , K_d) derived from the breakthrough curves are to a large extent determined by the assumptions on a , n and D_{pss} . The contributions of the fitting errors are much smaller.
10. The field experiments confirm that sodium and essentially also strontium undergo rapid and reversible linear¹³⁷ sorption as predicted from the laboratory measurements.
11. The sorption coefficients for sodium and strontium, determined in the migration field experiments, are consistent with the corresponding values determined in other experiments (within a factor 3 and covered to a large extent by the experimental errors¹³⁸). The reason for the agreement of the field measurements with the laboratory rock water interaction and the batch sorption experiments is mainly the similarity of the laboratory procedures preparing the rock samples to the geological processes which have generated the fault gouge. It can be concluded that for nuclides sorbing rapidly, not too strongly, linearly and exhibiting a reversible cation exchange process on fault gouge, the laboratory sorption coefficients can reasonably well be extrapolated to field conditions, provided adequate care is taken in selecting and preparing the rock samples.
12. The model was able to predict reasonably well the influence of a change in flow field from a 4.9 m dipole to a 1.7 m dipole. The prediction of the conservative tracer

¹³⁶It is interesting to note that new resin injection tests in the excavation project show also channelling in the fault gouge [private communication from R. Alexander].

¹³⁷ $C(\text{Na, rad. + carrier}) \ll C_{nat}(\text{Na})$ and $C(\text{Sr, rad. + carrier}) \ll C_{nat}(\text{Sr})$ according to Ref. ([4], p. 26).

¹³⁸For sodium as well as strontium $\Sigma_{tot} < 3 < \Sigma_{tot}^2$ was obtained (where Σ_{tot} is the geometric standard deviation of the corresponding field result).

uranine and the weakly sorbing sodium is good, that of the stronger sorbing strontium adequate.

13. The characteristic, relatively sharp strontium peak ($t_m = 0.9$ h) in the 1.7 m dipole field, not observed in the 4.9 m dipole and not described by the model, indicates an additional feature of the sorption process, possibly sorption kinetics. For safety assessments, such sorption kinetics is irrelevant.

The Grimsel migration field experiments, performed with an exceptional high precision, are a very useful test of model and data. The modelling results ¹³⁹ represent an important step in improving understanding of nuclide transport mechanisms and contribute to increase confidence to the transport calculations in the framework of safety assessments.

¹³⁹During preparation of this report a series of further field experiment has been performed, notably with the non-linearly sorbing tracer caesium. First results are included in Ref. [22] and [23]. Full modelling of these experiments is the subject of a forthcoming report.

7 Acknowledgements

Discussions on transport modelling with A. Jakob, P. Smith and C.F. Tsang are gratefully acknowledged. We have also profited from the exchange of ideas within the INTRAVAL community.

It would not have been possible, to reach the results of this report without the high quality of the field measurements and the detailed informations from the experimenters. We would like to thank especially T. Fierz and his crew, as well as U. Frick, but also E. Hoehn and J. Eikenberg. Useful suggestions were obtained in the meetings of the Technical Advisory Committee of the Grimsel migration experiment. In this context we want also to thank I. McKinley, N. Correa and R. Alexander. The comparison with laboratory data has greatly profited from discussions with B. Baeyens, M. Bradbury, R. Grauer and M. Mazurek.

Special thanks are due to C.F. Tsang for a careful review of the manuscript, as well as U. Frick, P. Zuidema, F. Neall and R. Alexander for helpful comments. The patient typing of the manuscript by E. Hochstrassser and the French translation of the abstract by C. Degueldre are also gratefully acknowledged.

Finally we thank Nagra for partial financial support.

8 Appendices

Appendix 1

The Width of the Breakthrough Curve Taking into Account Advection and Matrix Diffusion only

The width s is defined for the height $(1/\sqrt{e}) \cdot C_{f,m}(z)$ as

$$s = t_1 - t_2 \quad . \quad (\text{A1.1a})$$

t_i are the solutions of the equation:

$$C_f(z, t_i) = \frac{1}{\sqrt{e}} \cdot C_{f,m}(z) \quad . \quad (\text{A1.1b})$$

According to Eq. (27) and (28a) we get:

$$\sqrt{\zeta_i^3} \cdot e^{-\zeta_i} \approx \frac{\sqrt{\pi} \cdot 0.23}{\sqrt{e}} \quad , \quad (\text{A1.2a})$$

$$\zeta_i = \frac{\tau_0(z)}{t_i - \bar{t}(z)} \quad , \quad (\text{A1.2b})$$

$$s \approx \tau_0 \left(\frac{1}{\zeta_1} - \frac{1}{\zeta_2} \right) \quad . \quad (\text{A1.2c})$$

Eq. (A1.2a) has to be solved numerically. We obtain:

$$\zeta_1 \approx 0.58 \quad , \quad (\text{A1.3a})$$

$$\zeta_2 \approx 3.09 \quad , \quad (\text{A1.3b})$$

$$s \approx 1.4 \cdot \tau_0 \quad . \quad (\text{A1.3c})$$

Appendix 2

Influence of Dispersion

The analytical expressions for mass balance and concentration distribution, considering only advection and dispersion, are reproduced, here, in our notation (compare e.g. Ref. [25], p.628, 629). They illustrate the influence of dispersion in an equivalent porous medium model (similar to the considerations in chapter 3.2.5) but also the single porosity model, if ϵ is interpreted as a homogeneous flow porosity and R_f as a bulk sorption retardation factor.

In addition to section 3.2.2, the following assumptions are used:

1. No matrix diffusion into the porous rock zone.
2. 1D-flow field for one single stream tube (Fig. 5; $Q_k = Q_i$, $L_k = L$, $B_k = B$).
3. Infinite extension of the stream tube ($-\infty \leq z \leq L = \infty$)¹⁴⁰.
4. No radioactive decay.
5. Linear sorption.
6. Dirac delta injection as initial condition¹⁴¹.

In addition to section 3.2.2 we use the following **notation**:

$\sigma(t)$: Width parameter
$\bar{z}(t)$: Average tracer advection distance
$C_{fm,z}(t)$: Peak height of concentration space distribution
$z_m(t)$: Peak position of concentration space distribution
$s_z(t)$: $1(\sqrt{\epsilon})$ - width of concentration space distribution
$C_{fm}(z)$: Peak height of the breakthrough curve
$t_m(z)$: Peak position of the breakthrough curve

¹⁴⁰The breakthrough curve is not influenced by a boundary condition at the observation point z . To be as simple as possible it is also assumed that the breakthrough curve corresponds to the actual concentration (and not to an outflow concentration j_f/\bar{v} as in the model).

¹⁴¹The reason for using a source term instead of a boundary condition is the simplicity of the solution. In addition, the injection distribution has practically no influence on the breakthrough curve as long as dispersion has produced a breakthrough much wider than the injection distribution.

- $s(z)$: $(1\sqrt{\epsilon})$ - width of the breakthrough curve
 $\bar{t}(z)$: Average tracer advection time
 $K_{d,s}$: Sorption coefficient for single porosity model
 $(1-\epsilon)\rho$: Bulk density for single porosity model

According to the assumptions the equations of section 3.2.2 can be simplified.

The mass balance is expressed as

$$\frac{\partial C_f(z,t)}{\partial t} = -\frac{\bar{v}}{R_f} \frac{\partial C_f(z,t)}{\partial z} + a_L \frac{\bar{v}}{R_f} \frac{\partial^2 C_f(z,t)}{\partial z^2} , \quad (\text{A2.1})$$

with the boundary conditions

$$C_f(z = \pm\infty, t) = 0 , \quad (\text{A2.2a})$$

and the initial condition representing injection¹⁴²

$$C_f(z, t = 0) = \frac{M_0}{(\epsilon a)B \cdot R_f} \cdot \delta(z) , \quad (\text{A2.2b})$$

$$(\epsilon a)B = \frac{Q_i}{\bar{v}} ; \quad \text{for the equivalent porous medium model } (\epsilon a) = n \cdot 2b . \quad (\text{A2.2c})$$

The flux is given by

$$j_f(z, t) = \bar{v}C_f(z, t) - a_L \cdot \bar{v} \frac{\partial C_f(z, t)}{\partial z} , \quad (\text{A2.2d})$$

and the retardation factor by

$$R_f = 1 + \frac{1}{b}K_a ; \quad \text{for the equivalent porous medium model} , \quad (\text{A2.2e})$$

$$R_f = 1 + \frac{(1-\epsilon)\rho}{\epsilon}K_{d,s} ; \quad \text{for the single porosity model} . \quad (\text{A2.2f})$$

¹⁴²Eq. (A2.2b) implies sorption equilibrium at $t = 0$.

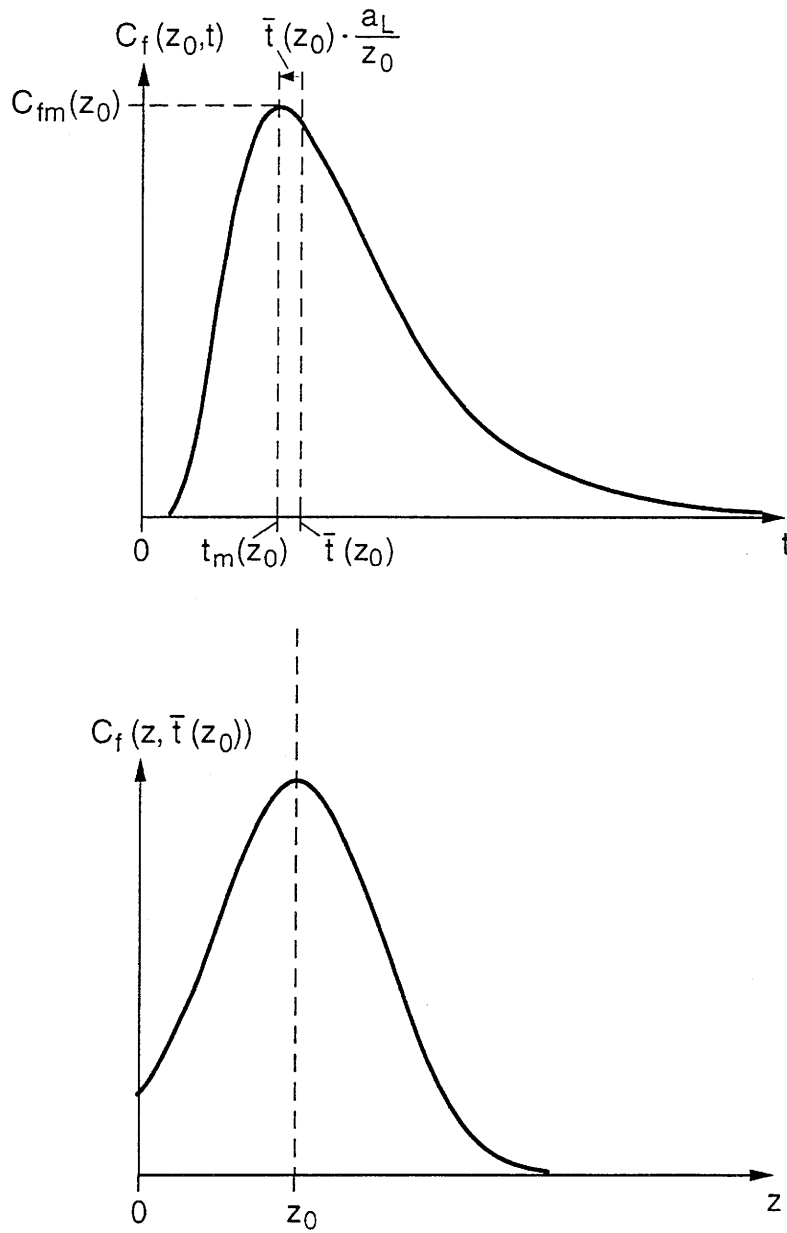


Figure A2.1 Concentration distributions for nuclide transport by advection and dispersion only. Upper part: The breakthrough curve at the observation point $z = z_0$ exhibits a moderate asymmetry and a peak positioned slightly earlier than the advection time $\bar{t}(z_0)$. Lower part: The spatial distribution at $t = \bar{t}(z_0)$ is symmetric with respect to the advection distance z_0 and similar to the breakthrough curve.

The tracer concentration is calculated as

$$C_f(z, t) = \frac{M_0}{(\epsilon a)B \cdot R_f} \cdot f(z, t) \quad , \quad (\text{A2.3a})$$

$$f(z, t) = \frac{1}{\sqrt{2\pi} \cdot \sigma(t)} \cdot \exp \left[-\frac{(z - \bar{z}(t))^2}{2\sigma^2(t)} \right] \quad , \quad (\text{A2.3b})$$

$$\int_{-\infty}^{+\infty} f(z, t) dz = 1 \quad , \quad (\text{A2.3c})$$

$$\bar{z}(t) = \frac{\bar{v}}{R_f} \cdot t \quad , \quad (\text{A2.3d})$$

$$\sigma(t) = \sqrt{2a_L \bar{z}(t)} \quad . \quad (\text{A2.3e})$$

Interpreting Eqs. (A2.3) as a spatial distribution (fixed t) we see a Gaussian curve. The width $2\sigma(t)$ is dependent only on peak position $\bar{z}(t)$ but not on velocity. Interpreting Eqs. (A2.3) as a breakthrough curve (distribution in time, fixed z), we see a shape with a slight asymmetry (due to the time dependence of $\sigma(t)$)¹⁴³.

Peak height $C_{f_{m,z}}(t)$, position $z_m(t)$ and width $s_z(t)$ of the **space distribution** at a fixed time $t > 0$ are:

$$C_{f_{m,z}}(t) = \frac{1}{\sqrt{2\pi}} \cdot \frac{\left(\frac{M_0}{(\epsilon a)B \cdot R_f}\right)}{\sigma(t)} \approx 0.40 \cdot \frac{\left(\frac{M_0}{(\epsilon a)B \cdot R_f}\right)}{\sigma(t)} \quad , \quad (\text{A2.4a})$$

$$z_m(t) = \bar{z}(t) \quad , \quad (\text{A2.4b})$$

$$s_z(t) = 2\sigma(t) \quad . \quad (\text{A2.4c})$$

¹⁴³In order to use the breakthrough curve as an approximation of nuclide concentration from a dipole flow field we have to take into account dilution by external fracture water; that is divide the concentration given by Eq. (A2.3) by the factor $\beta = Q_w/Q_i$.

Peak height $C_{fm}(z)$, position $t_m(z)$, and width $s(z)$ of the breakthrough curve at a fixed point $z > 0$ are:

$$C_{fm}(z) = \frac{1}{\sqrt{2\pi}} \cdot \frac{\left(\frac{M_0}{(\epsilon a) \bar{B} \cdot R_f}\right)}{\sigma(z)} \cdot \left[1 + \frac{1}{4} \left(\frac{a_L}{z}\right) + o\left\{\left(\frac{a_L}{z}\right)^2\right\}\right] \quad ; \quad \text{for} \quad \left(\frac{a_L}{z}\right) \ll 1 \quad , \quad (\text{A2.5a})$$

$$\sigma(z) = \sqrt{2a_L z} \quad , \quad (\text{A2.5b})$$

$$t_m(z) = \bar{t}(z) \cdot \left[1 - \left(\frac{a_L}{z}\right) + o\left\{\left(\frac{a_L}{z}\right)^2\right\}\right] \quad ; \quad \text{for} \quad \left(\frac{a_L}{z}\right) \ll 1 \quad , \quad (\text{A2.5c})$$

$$\bar{t}(z) = \frac{z}{\left(\frac{\bar{v}}{R_f}\right)} \quad , \quad (\text{A2.5d})$$

$$s(z) \approx \frac{2\sigma(z)}{\left(\frac{\bar{v}}{R_f}\right)} \quad . \quad (\text{A2.5e})$$

Appendix 3

Comments to the Parameters of the Porous Rock Zone

The following considerations support the discussion of breakthrough curves. Neglecting radioactive decay, assuming linear sorption, and applying the transformation

$$\zeta = \frac{(x - b)}{\sqrt{D_p/R_p}} \quad , \quad (\text{A3.1})$$

the mass balances, cf. Eqs. (18) and (19), can be simplified.

In the water conducting zone we obtain:

$$\frac{\partial C_f(z, t)}{\partial t} = \frac{1}{R_f} \left[-\bar{v} \frac{\partial C_f(z, t)}{\partial z} + a_L \bar{v} \frac{\partial^2 C_f(z, t)}{\partial z^2} + P_F \frac{\partial C_p(\zeta, z, t)}{\partial \zeta} \Big|_{\zeta=0, z, t} \right] \quad , \quad (\text{A3.2a})$$

$$P_F = \left(\frac{\epsilon_p}{b} \right) \cdot \sqrt{D_p R_p} \quad \text{combined interface flux parameter} \quad , \quad (\text{A3.2b})$$

$$-P_F \frac{\partial C_p(\zeta, z, t)}{\partial \zeta} \Big|_{\zeta=0} = \left(\frac{\epsilon_p}{b} \right) j_p(\zeta, z, t) \Big|_{\zeta=0} \quad \text{interface flux} \quad . \quad (\text{A3.2c})$$

In the porous rock zone we obtain:

$$\frac{\partial C_p(\zeta, z, t)}{\partial t} = \frac{\partial^2 C_p(\zeta, z, t)}{\partial \zeta^2} \quad , \quad (\text{A3.3a})$$

$$C_p(\zeta = 0, z, t) = C_f(z, t) \quad \text{interface BC} \quad , \quad (\text{A3.3b})$$

$$\frac{\partial C_p(\zeta, z, t)}{\partial \zeta} \Big|_{\zeta=P_B} = 0 \quad \text{porous rock zone BC} \quad , \quad (\text{A3.3c})$$

$$P_B = \frac{d}{\sqrt{D_p/R_p}} \quad \text{combined tail end parameter} \quad . \quad (\text{A3.3d})$$

The equations show:

1. The parameters of the porous rock zone appear in the combined values P_F and P_B . Any parameter variation which does not change these two values (and keeping a_L and \bar{v} constant) leaves the breakthrough curve unaltered.
2. As long as the porous rock zone boundary does not noticeably affect the concentration distribution near the interface, the breakthrough curve is fully defined by the parameter P_F (assuming a_L and \bar{v} are constant). The analytical expressions derived for simplified conditions and an infinite depth d of the porous rock zone, confirm this statement (cf. Eq. (27f)). For a sufficiently small time, P_F is proportional to the interface flux per unit volume of the water conducting zone. The reason why the interface flux is controlled by $\epsilon_p \sqrt{D_p}$, and not by $\epsilon_p D_p$ occurring in the basic mass balance equation, Eq. (18a), is the reduction of concentration gradient in the porous rock zone when D_p increases.
3. P_B^2 is equal to the penetration time t_p , Eq. (31e), for twice the width of the porous rock zone (forwards and backwards). It controls the time at which the breakthrough curve is affected by the porous rock zone boundary. According to the numerical results in chapter 4 we get:

$$P_B^2(\text{uranine}) = \left(\frac{a - \epsilon a}{2n} \right)^2 \cdot B_c^2 = 430 \text{ h} \quad ,$$

$$P_B^2(\text{sodium}) = \left(\frac{a - \epsilon a}{2n} \right)^2 \cdot B_s^2 = 2100 \text{ h} \quad .$$

These values suggest that P_B^2 can directly be used as a very rough guess of the position t_d of the tail end perturbation (cf. Figs. 10 and 16, upper parts).

$$P_B^2 = t_p(2d) \approx t_d \quad . \tag{A3.4}$$

This interpretation is valid only if the probability, that a nuclide diffuses more than once from the interface to the outer boundary of the porous rock zone and back to the water conducting zone, is small. In that case (requiring small sorption, not too long travelling distances or too slow water velocities) the time region of the tail end perturbation should practically be independent of the flow field. The calculations for the 4.9 m and 1.7 m dipole flow fields confirm this behaviour for uranine (cf. Fig. 10 (upper part) and Fig. 23 (upper part)) and indicate the same behaviour for sodium

(cf. Fig. 16 (upper part) and Fig. 23 (lower part)). For more strongly sorbing nuclides P_B^2 is rather a lower limit for the time of tail end perturbation.

Appendix 4

Error Estimate of the Physical Parameters Derived from the Fit

1. General Equations

The error estimate is based on a log-normal distribution (compare e.g. Ref. [26]). For the convenience of the reader, the definitions and relations relevant to our application are reproduced:

Stochastic variable	:	x
Distribution	:	$f(x) dx$
Geometric standard deviation of x	:	Σ
Standard deviation of $\ln(x)$:	$\tilde{\sigma} = \ln \Sigma$
Median	:	M

$$f(x)dx = \frac{1}{\sqrt{2\pi} \cdot \ln \Sigma} \cdot \exp \left[- \left(\frac{\ln \left(\frac{x}{M} \right)}{\sqrt{2} \cdot \ln \Sigma} \right)^2 \right] \cdot \frac{dx}{x} , \quad (\text{A4.1a})$$

$$\int_0^M f(x)dx = 0.5 , \quad (\text{A4.1b})$$

$$\int_{M/\Sigma}^{M \cdot \Sigma} f(x)dx \approx 0.68 , \quad (\text{A4.1c})$$

$$\int_{M/\Sigma^2}^{M \cdot \Sigma^2} f(x)dx \approx 0.95 , \quad (\text{A4.1d})$$

$$\tilde{\sigma}^2 \left(\prod_i x_i \right) = \sum_i \tilde{\sigma}^2(x_i) \quad \text{if the variables } x_i \text{ are independent} . \quad (\text{A4.1e})$$

2. Conservative Tracer Uranine

From the fit we get:

$$\tilde{\sigma}(\epsilon a) = \ln \Sigma(\epsilon a) \quad , \quad (\text{A4.2a})$$

$$\tilde{\sigma}(F_c) = \ln \Sigma(F_c) \quad , \quad (\text{A4.2b})$$

$$\tilde{\sigma}(B_c) = \ln \Sigma(B_c) \quad . \quad (\text{A4.2c})$$

For the **fitting errors**, we take the logarithm of the expressions for the physical parameters, (cf. Eqs. (34b), (34c), (36a) and (36b)) and calculate the variance neglecting errors in a and n :

$$\tilde{\sigma}_{fit}^2(\epsilon_{pc}) = \tilde{\sigma}^2(F_c) + \tilde{\sigma}^2(B_c) \quad , \quad (\text{A4.2d})$$

$$\tilde{\sigma}_{fit}^2(D_{pc}) = 4 \cdot \tilde{\sigma}^2(B_c) \quad , \quad (\text{A4.2e})$$

$$\tilde{\sigma}_{fit}^2(b) = \tilde{\sigma}^2(\epsilon a) \quad , \quad (\text{A4.2f})$$

$$\tilde{\sigma}_{fit}^2(d) \approx 0 \quad \text{since } (\epsilon a) \ll a \quad . \quad (\text{A4.2g})$$

Varying the fixed parameters a and n changes b and d , but the other parameters, especially a_L , (ϵa) and \bar{v} , are kept unaltered. Under these conditions we preserve the fit of the breakthrough curve by keeping the combined parameters P_{F_c} and P_{B_c} of Eqs. (A3.2b) and (A3.3d) constant and adapting F_c and B_c to the changed values of a and n .

The combined parameters read:

$$P_{F_c} = \left(\frac{2n}{\epsilon a} \right) \cdot F_c \quad , \quad (\text{A4.3a})$$

$$P_{B_c} = \left(\frac{a - \epsilon a}{2n} \right) \cdot B_c \quad . \quad (\text{A4.3b})$$

To calculate the **total errors** (of an unchanged fit), including the uncertainties of a and n , we have to express the physical parameters in terms of the combined parameters¹⁴⁴:

$$\epsilon_{pc} = \left(\frac{\epsilon a}{a - \epsilon a} \right) \cdot P_{F_c} \cdot P_{B_c} \quad , \quad (\text{A4.4a})$$

$$D_{pc} = \left(\frac{a - \epsilon a}{2n} \right)^2 \cdot \left(\frac{1}{P_{B_c}} \right)^2 \quad . \quad (\text{A4.4b})$$

Under the assumption of error-free fixed parameters, we obtain the variances of the relevant combinations of P_{F_c} , P_{B_c} and (ϵa) ¹⁴⁵:

$$\tilde{\sigma}^2(\epsilon a \cdot P_{F_c} \cdot P_{B_c}) \approx \tilde{\sigma}_{fit}^2(\epsilon_{pc}) \quad , \quad (\text{A4.5a})$$

$$\tilde{\sigma}^2 \left(\left[\frac{1}{P_{B_c}} \right]^2 \right) \approx \tilde{\sigma}_{fit}^2(D_{pc}) \quad . \quad (\text{A4.5b})$$

Assuming, now, that the fixed parameters are also medians of log-normal distributions, the total variances of the physical parameters can be calculated from Eqs. (A4.4), (A4.5), (34b) and (34c) and taking into account that (ϵa) , P_{F_c} and P_{B_c} are not altered by changes of a and n :

$$\tilde{\sigma}_{tot}^2(\epsilon_{pc}) \approx \tilde{\sigma}_{fit}^2(\epsilon_{pc}) + \tilde{\sigma}^2(a) \quad , \quad (\text{A4.6a})$$

$$\tilde{\sigma}_{tot}^2(D_{pc}) \approx \tilde{\sigma}_{fit}^2(D_{pc}) + 4 \cdot [\tilde{\sigma}^2(a) + \tilde{\sigma}^2(n)] \quad , \quad (\text{A4.6b})$$

$$\tilde{\sigma}_{tot}^2(b) = \tilde{\sigma}_{fit}^2(b) + \tilde{\sigma}^2(n) \quad , \quad (\text{A4.6c})$$

$$\tilde{\sigma}_{tot}^2(d) \approx \tilde{\sigma}^2(a) + \tilde{\sigma}^2(n) \quad . \quad (\text{A4.6d})$$

¹⁴⁴The expressions for b and d (cf. Eqs. (34b) and (34c)) are not altered since they do not contain F_c or B_c .

¹⁴⁵ $\tilde{\sigma}^2(a - \epsilon a) \approx \tilde{\sigma}^2(a)$ since $(\epsilon a/a) < 10^{-2}$ and $\Sigma(\epsilon a)/\Sigma(a) < 0.6$.

3. Weakly Sorbing Tracer Sodium

The same procedure as for the conservative tracer is applied.

The fitting errors are (cf. Eqs.(41))¹⁴⁶:

$$\tilde{\sigma}_{fit}^2(R_{ps}) = \tilde{\sigma}_{fit}^2(D_{ps}) = \tilde{\sigma}^2(F_s) + \tilde{\sigma}^2(B_s) + \tilde{\sigma}^2(F_c) + \tilde{\sigma}^2(B_c) \quad , \quad (\text{A4.7a})$$

$$\tilde{\sigma}_{fit}^2(K_{ds}) \approx \tilde{\sigma}^2(F_s) + \tilde{\sigma}^2(B_s) \quad . \quad (\text{A4.7b})$$

Combined parameters:

$$P_{F_s} = \left(\frac{2n}{\epsilon a} \right) \cdot F_s \quad , \quad (\text{A4.8a})$$

$$P_{B_s} = \left(\frac{a - \epsilon a}{2n} \right) \cdot B_s \quad . \quad (\text{A4.8b})$$

Physical parameters of Eqs. (41), expressed by the combined parameters of Eqs. (A4.8) and (A4.3):

$$D_{ps} = \left(\frac{a - \epsilon a}{2n} \right)^2 \cdot \frac{P_{F_s}}{P_{B_s} \cdot P_{F_c} \cdot P_{B_c}} \quad , \quad (\text{A4.9a})$$

$$R_{ps} = \frac{P_{F_s} \cdot P_{B_s}}{P_{F_c} \cdot P_{B_c}} \quad , \quad (\text{A4.9b})$$

$$K_{ds} = \frac{1}{\tilde{\rho}_p} \cdot \frac{(\epsilon a)}{(a - \epsilon a)} \cdot P_{F_s} \cdot P_{B_s} \cdot \left[1 - \frac{P_{F_c} \cdot P_{B_c}}{P_{F_s} \cdot P_{B_s}} \right] \quad . \quad (\text{A4.9c})$$

The total errors are:

$$\tilde{\sigma}_{tot}^2(D_{ps}) \approx \tilde{\sigma}_{fit}^2(D_{ps}) + 4 \cdot \left[\tilde{\sigma}^2(a) + \tilde{\sigma}^2(n) \right] \quad , \quad (\text{A4.10a})$$

$$\tilde{\sigma}_{tot}^2(R_{ps}) = \tilde{\sigma}_{fit}^2(R_{ps}) \quad [\text{no influence from } a, n, \tilde{\rho}] \quad , \quad (\text{A4.10b})$$

¹⁴⁶The square bracket in Eq. (41c) is almost 1 and, therefore, the corresponding contribution to the error of K_d neglected.

$$\tilde{\sigma}_{tot}^2(K_{ds}) \approx \tilde{\sigma}_{fit}^2(K_{ds}) + \tilde{\sigma}^2(a) + \tilde{\sigma}^2(\tilde{\rho}) \quad . \quad (\text{A4.10c})$$

4. Stronger Sorbing Tracer Strontium

The same procedure as for the conservative tracer is applied, again (treating the factor E_D analogously to the fixed parameters).

The fitting errors are (cf. Eqs. (44)):

$$\tilde{\sigma}_{fit}^2(R_{pss}) = 4 \cdot [\tilde{\sigma}^2(F_{ss}) + \tilde{\sigma}^2(F_c)] \quad , \quad (\text{A4.11a})$$

$$\tilde{\sigma}_{fit}^2(K_{dss}) \approx 4 \cdot \tilde{\sigma}^2(F_{ss}) + \tilde{\sigma}^2(F_c) + \tilde{\sigma}^2(B_c) \quad . \quad (\text{A4.11b})$$

Combined parameter:

$$P_{F_{ss}} = \left(\frac{2n}{\epsilon a} \right) \cdot F_{ss} \quad . \quad (\text{A4.12})$$

Physical parameters of Eqs. (43) and (44), expressed by the combined parameters of Eqs. (A4.12) and (A4.3):

$$R_{pss} = \left(\frac{P_{F_{ss}}}{P_{F_c}} \right)^2 \cdot \frac{1}{E_D} \quad , \quad (\text{A4.13a})$$

$$K_{dss} = \frac{(\epsilon a)}{\tilde{\rho}_p(a - \epsilon a)} \cdot \frac{P_{F_{ss}}^2 \cdot P_{B_c}}{P_{F_c} \cdot E_D} \cdot \left[1 - \left(\frac{P_{F_c}}{P_{F_{ss}}} \right)^2 \cdot E_D \right] \quad . \quad (\text{A4.13b})$$

The total errors are:

$$\tilde{\sigma}_{tot}^2(R_{pss}) = \tilde{\sigma}_{fit}^2(R_{pss}) + \tilde{\sigma}^2(E_D) \quad , \quad (\text{A4.14a})$$

$$\tilde{\sigma}_{tot}^2(K_{dss}) \approx \tilde{\sigma}_{fit}^2(K_{dss}) + \tilde{\sigma}^2(a) + \tilde{\sigma}^2(E_D) + \tilde{\sigma}^2(\tilde{\rho}) \quad . \quad (\text{A4.14b})$$

Appendix 5

Parameters of the Migration Zone as Deduced from Geological Investigations

From geological investigations the porosity ϵ_{pF} and the pore diffusion coefficients D_{pF} for the fault gouge regions adjacent to the water channels¹⁴⁷ are deduced. They are compared to ϵ_p and D_p as determined in the migration experiments (since the analysis showed that matrix diffusion mainly takes place in the fault gouge)¹⁴⁸.

1. Notation

- b [m] : Half width of a water conducting zone
- n : Number of water conducting zones in the migration zone
- a_{TF} [m] : Sum of the widths of all fault gouges across the migration zone (including the water channels)
- d_F [m] : Fault gouge depth corresponding to 1 water conducting zone surface
- $\epsilon_{pTF,min/max}$: Limits of total fault gouge porosity (including the water channels)
- ϵ_{pTF} : Total fault gouge porosity (including the water channels)
- ϵ_{pF} : Fault gouge porosity

¹⁴⁷Water channels = narrow regions of flowing water corresponding to the water conducting zones of the model.

¹⁴⁸The physical values for porosity and the pore diffusion coefficients reported in Ref. [24] are averaged over the fault gouge and the adjacent rock. They are therefore considerably smaller than the results given here.

Σ	:	Estimate of 1 geometric standard deviation
D_w [m ² /s]	:	Diffusion coefficient in unconfined water
$G(\epsilon_{pF})$:	Formation factor for the fault gouge regions
$G_{max/min}(\epsilon_{pF})$:	Limits of the formation factor for the fault gouge regions
D_{pF} [m ² /s]	:	Pore diffusion coefficient for the fault gouge regions

2. Basic Data

The estimate relies on the following data:

$\epsilon_{pTF,min}$	= 0.1	(cf. Ref. [10], p. 20)
$\epsilon_{pTF,max}$	= 0.3	(")
a_{TF}	= $7 \cdot 10^{-3}$ m	(cf. Ref. [10], p. 25, Fig. 12)
D_w (uranine)	= $0.5 \cdot 10^{-9}$ m ² /s	(cf. Ref. [27], p. 14)
D_w (sodium)	= $1.5 \cdot 10^{-9}$ m ² /s	(cf. Ref. [27], p. 20)
D_w (strontium)	= $(0.7-1) \cdot 10^{-9}$ m ² /s	(") .

In addition, the estimate has to be consistent with the model assumptions on geometry, and therefore with:

$$n = 4 \text{ (cf. Eq. (33b))}$$

$$b = 4.6 \cdot 10^{-5} \text{ m (cf. Eq. (37e))}$$

3. Average Porosity of the Fault Gouge Regions

The guess ϵ_{pTF} and the error Σ for the fault gouge porosity is obtained directly from the limits¹⁴⁹:

$$\epsilon_{pTF} = \sqrt{\epsilon_{pTF,min} \cdot \epsilon_{pTF,max}} \quad , \quad (\text{A5.1a})$$

$$\Sigma(\epsilon_{pTF}) = \left(\frac{\epsilon_{pTF,max}}{\epsilon_{pTF,min}} \right)^{\frac{1}{2}} \quad , \quad (\text{A5.1b})$$

¹⁴⁹ Assuming the guess is the median of a log-normal distribution and the limits correspond to 1 geometric standard deviation.

$$\epsilon_{pTF} = 0.17 ; \Sigma(\epsilon_{pTF}) = 1.7 \quad . \quad (\text{A5.1c})$$

According to a volume weighted correction for the porosity of the water channels we obtain:

$$d_F = \frac{a_{TF}}{2n} - b \quad , \quad (\text{A5.2a})$$

$$\epsilon_{pF} = \left(1 + \frac{b}{d_F}\right) \cdot \epsilon_{pTF} - \frac{b}{d_F} \quad , \quad (\text{A5.2b})$$

$$\Sigma(\epsilon_{pF}) \approx \Sigma(\epsilon_{pTF}) \quad . \quad (\text{A5.2c})$$

Introducing the numerical values leads to:

$$d_F = 8.3 \cdot 10^{-4} \text{ m} \quad , \quad (\text{A5.2d})$$

$$\epsilon_{pF} = (0.12^{+0.08}_{-0.05}) ; \Sigma(\epsilon_{pF}) \approx 1.7 \quad . \quad (\text{A5.2e})$$

4. Average Pore Diffusion Coefficient of the Fault Gouge Regions

The concept of a nuclide independent formation factor taking into account pore geometry reads (cf. Ref. [27], p. 27):

$$D_{pF} = D_w \cdot G(\epsilon_{pF}) \quad . \quad (\text{A5.3a})$$

The porosity dependent formation factor G is defined according to a nomogram in Ref. ([27], p. 73)¹⁵⁰:

$$G \approx G(\epsilon_{pF} = 0.12, \text{ curves 2+3}) = 0.15,$$

$$G_{min} \approx G(\epsilon_{pF} = 0.07, \text{ curve 3}) = 0.066,$$

$$G_{max} \approx G(\epsilon_{pF} = 0.20, \text{ curve 2}) = 0.31 \quad .$$

¹⁵⁰Following discussions with U. Frick, curve 2 (frische Granite, Klufthekzie) of the nomogram was taken as upper limit and curve 3 (tonig umgewandelte Granite, frische Gneise) as lower limit. Our estimate was calculated as geometric mean of the upper and lower limit.

The corresponding pore diffusion coefficients according to Eq. (A5.3a) are¹⁵¹:

$$D_{pF}(\textit{uranine}) = (7.5_{-4.2}^{+8.0}) \cdot 10^{-11} \text{m}^2/\text{s} \quad , \quad (\text{A5.4a})$$

$$D_{pF}(\textit{sodium}) = (2.3_{-1.3}^{+2.4}) \cdot 10^{-10} \text{m}^2/\text{s} \quad , \quad (\text{A5.4b})$$

$$D_{pF}(\textit{strontium}) = (1.3_{-0.8}^{+1.8}) \cdot 10^{-10} \text{m}^2/\text{s} \quad . \quad (\text{A5.4c})$$

¹⁵¹For strontium the diffusion coefficient is based on the arithmetic mean of the D_w limits, and the errors include the uncertainty of D_w .

Appendix 6

Extrapolation of Laboratory Results to the Conditions of the Migration Field Experiments

The following extrapolations have to be understood as an attempt to compare as closely as possible the same quantities at the expense of introducing large extrapolation errors for values measured with relatively high precision.

1. Extrapolation to a Different Mineralogical Composition

The batch sorption experiments as well as the rock water interaction experiments were performed on mylonite samples from the shear-zone AU126 (cf. Ref. [15], p. 3 and Ref. [18] p. 55), genetically similar to the migration fracture AU96. Sorption in the migration shear-zone mainly takes place in the fault gouge (mylonite of AU96, crushed by brittle rock deformation). Since no mineralogical data on this fault gouge were available, the laboratory experiments were extrapolated (as a first step) from mylonite AU126 to mylonite AU96 using the respective cation exchange capacities (CEC), determined and applied to the same extrapolation as in Ref. ([20], p. 44 and 45):

$$K_d(AU96) = \frac{K_d(AU126)}{w_1} , \quad (A6.1a)$$

$$w_1 = \frac{CEC(AU126)}{CEC(AU96)} = \frac{14.5 \text{ meq/kg}}{5.3 \text{ meq/kg}} = 2.7 . \quad (A6.1b)$$

The higher CEC value of the shear-zone AU126 is due to a higher muscovite/sericite content. To allow for the uncertainty of the extrapolation, half of the change is covered by an additional extrapolation error (applied in the opposite direction of the correction). The relative error of the extrapolated K_d can therefore be written as:

$$\frac{+\delta K_d(AU96)}{K_d(AU96)} = \frac{+\delta K_d(AU126)}{K_d(AU126)} + \frac{w_1 - 1}{2} , \quad (A6.2a)$$

$$\frac{-\delta K_d(AU96)}{K_d(AU96)} = \frac{-\delta K_d(AU126)}{K_d(AU126)} . \quad (A6.2b)$$

2. Extrapolation to Different Rock Samples

The extrapolation of the laboratory results for the fraction $< 250 \mu\text{m}$ to the samples “loosely disaggregated” was performed using corresponding CEC values, given in Ref. ([20], p. 43):

$$K_d(\textit{loosely dis.}) = \frac{K_d(< 250 \mu\text{m})}{w_2} , \quad (A6.3a)$$

$$w_2 = \frac{CEC(< 250 \mu\text{m})}{CEC(\textit{loosely dis.})} = \frac{6 \text{ meq/kg}}{3 \text{ meq/kg}} = 2 . \quad (A6.3b)$$

As before, an extrapolation error covering half of the change is added, so that the relative error of the extrapolated K_d reads:

$$\frac{+\delta K_d(\textit{loosely dis.})}{K_d(\textit{loosely dis.})} = \frac{+\delta K_d(< 250 \mu\text{m})}{K_d(< 250 \mu\text{m})} + \frac{w_2 - 1}{2} , \quad (A6.4a)$$

$$\frac{-\delta K_d(\textit{loosely dis.})}{K_d(\textit{loosely dis.})} = \frac{-\delta K_d(< 250 \mu\text{m})}{K_d(< 250 \mu\text{m})} . \quad (A6.4b)$$

3. Numerical Results

The original experimental sorption coefficients and the corresponding extrapolated values are listed in the following table:

Tab. A6.1 Measured and Extrapolated Sorption Coefficients K_d [10^{-3} m³/kg]

Type of Experiment	Measurement AU 126		Extrapolation AU 96	
	Na	Sr	Na	Sr
Rock water interaction	0.3 - 0.4 ¹⁾	16 - 25 ¹⁾	$0.13 \pm \begin{matrix} 0.13 \\ 0.02 \end{matrix}$ ²⁾	$7.6 \pm \begin{matrix} 8.2 \\ 1.7 \end{matrix}$ ²⁾
Sorption (< 63 μ m)	3.5 ± 1 ³⁾	110 ± 10 ³⁾	$1.3 \pm \begin{matrix} 1.5 \\ 0.4 \end{matrix}$	$41 \pm \begin{matrix} 39 \\ 4 \end{matrix}$
Sorption (< 250 μ m)	2.3 ± 0.1 ³⁾	66.9 ± 3.8 ³⁾	$0.85 \pm \begin{matrix} 0.76 \\ 0.04 \end{matrix}$	$25 \pm \begin{matrix} 22 \\ 1 \end{matrix}$
Sorption (loosely dis.) ⁴⁾	--	--	$0.43 \pm \begin{matrix} 0.60 \\ 0.02 \end{matrix}$	$13 \pm \begin{matrix} 19 \\ 1 \end{matrix}$

1) Ref. ([18], p. 58 Tab. 17) and Ref. ([3], p. 5-8, Tab. 5-4)

2) Prior to extrapolation, the experimental range is changed into a representative value and an error (using the arithmetic mean of the range limits).

3) Ref. ([15], p. 40) and Ref. ([3], p. 5-11 and 5-12)

4) Approximate grain size < 2 mm

Appendix 7

Selected Dipole Positions and Flow Fields for Tracer Experiments

Before starting with the dipole experiments, the hydraulic conditions in the migration shear-zone was investigated. The intersections of the corresponding bore holes with the zone are depicted in Fig. A7.1. The bore hole pairs selected for tracer dipole experiments are:

- a) Injection at BOMI 86.004, Extraction at BOMI 87.006, distance 4.9 m
- b) Injection at BOMI 87.009, Extraction at BOMI 87.006, distance 1.7 m
- c) Injection at BOMI 86.004, Extraction at BOMI 87.010, distance 14 m

Experiments in dipole c) are not described in this paper. The migration shear-zone was not sufficiently transmissive around boreholes BOMI 86.005 and BOMI 87.007 to establish practicable dipole flow fields. Typical experimental dipole fields are schematically presented in the figure. A certain curved nature of the fields was indicated when monitoring tracer concentrations in BOMI 87.009 during the 4.9 m experiments. The natural background flow direction is from the right to the left.

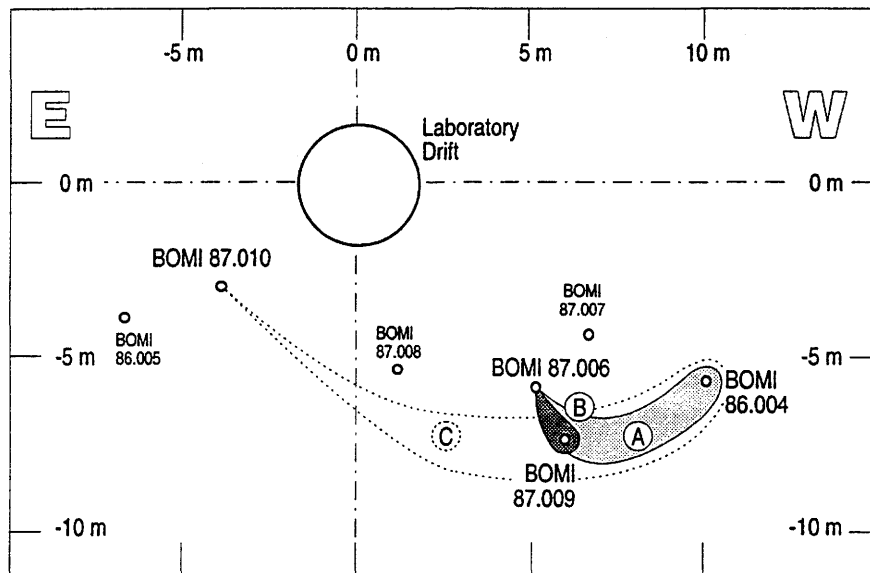


Figure A7.1 Locations of bore hole intersections with the migration shear-zone and schematic presentation of flow fields for selected dipole positions (courtesy U. Frick).

Appendix 8

Influence of the Dipole Flow Field Geometry to the Breakthrough Curve

In the present report, nuclide migration in a narrow dipole field ($\beta=16$) has been investigated. The question arises to what extent nuclide migration properties, especially the impact of matrix diffusion, could be unambiguously extracted for wider dipole field¹⁵². To get indications on the influence of widening the dipole field, breakthrough curves for $\beta = 16, 3$ and 1.5 were calculated using the conservative uranium and the sorbing strontium as tracers. For these calculations the extraction rate Q_w and the injection distribution $C_0(t)$ were kept unchanged¹⁵³. Streamline pictures for similar β s are shown in Fig. 4.

The breakthrough curves for nuclide transport without matrix diffusion in different flow fields are represented in Fig. A8.1 (upper part). They show the following behaviour when decreasing β :

- Shift of peak position to earlier times, mainly due to enhanced water velocities in the stream tubes near the dipole axis. Near the axis the effect of widening the stream tubes is overcompensated by the increase of Q_i ¹⁵⁴.
- Reduction of peak concentration due to larger stream tube widths, a reduced overlapping¹⁵⁵ of individual stream tube breakthrough curves, and a noticeable influence of the injection distribution for higher water velocities¹⁵⁶. These effects are to a large extent compensated by the smaller dilution with external fracture water.

¹⁵²Such experiments have indeed been performed at the Grimsel Test Site (Ref. [4], section 4.2.3). The wider dipole field also means that heterogeneities in the fracture might play a larger role and breakthrough curves become more complex (cf. Refs. [28] and [29]). In fact, this is seen with the experimentally measured double-humped breakthrough curves for $\beta = 3$. In this appendix we assume that the dipole region shows negligible heterogeneity (which is **not** the case at GTS for wide dipole fields).

¹⁵³A change of Q_w (and Q_i), keeping β fixed at the desired value, would only lead to a proportional change of the water velocities (cf. Eqs. (5)). Cases without matrix diffusion would therefore show breakthrough curves which are shifted on a logarithmic time scale, provided $C_0(t)$ is narrow enough (cf. Eqs. (A2.3)).

¹⁵⁴The corresponding advection times can be estimated using the water transit times \bar{t}_0 for the dipole axis (cf. Eqs. 15). The numerical values are: $\bar{t}_0(\beta=16) = 2.5$ h, $\bar{t}_0(\beta=3) = 1.7$ h, $\bar{t}_0(\beta=1.5) = 1.3$ h.

¹⁵⁵Reduced overlapping is caused by delay and widening of the breakthrough curves.

¹⁵⁶Widening a narrow nuclide pulse (in z -direction of a stream tube) by advective-dispersive transport is independent of the water velocity (under the assumptions of section 3.2.2). The width of the injected pulse (in z -direction), however, increases proportional to the water velocity. The injection distribution (not being narrow enough for the increased water velocity) decreases the peak height of the breakthrough curve.

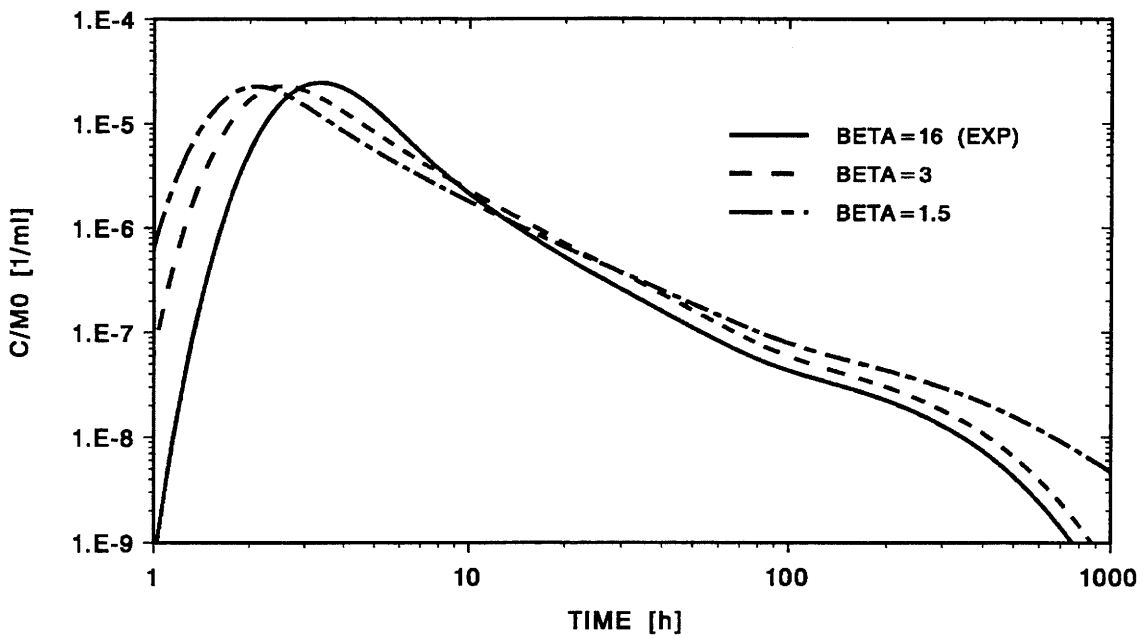
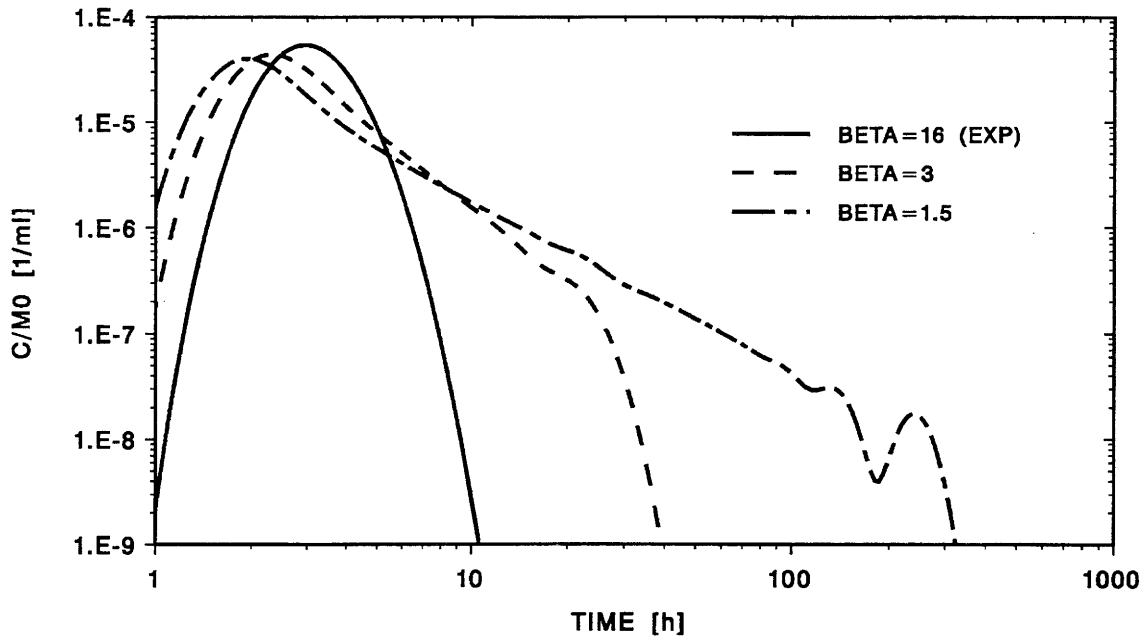


Figure A8.1 Influence of widening the flow field on the breakthrough curve for the conservative uranium. Upper part: Without matrix diffusion, the flow field deforms the breakthrough curve from the solid to the dashed and the dot-dashed line. With decreasing β a tail is generated which gets longer and flatter. Lower part: Taking matrix diffusion into account, the flow fields for $\beta = 16$ and 3 generate similar tails.

- Marked tailing due to increased water transit times¹⁵⁷ in the outer stream tubes. When decreasing β the tailing becomes flatter reaching for $\beta = 1.5$ almost the slope characteristic for matrix diffusion. The oscillation at the tail end (especially for $\beta = 1.5$) is a consequence of the flow field discretisation not being fine enough¹⁵⁸.

The breakthrough curves for nuclide transport including matrix diffusion are represented in Fig. A8.1 (lower part). They show the following features when decreasing β :

- Peak concentrations exhibiting a similar behaviour as the breakthrough curves without matrix diffusion, being typical for the flow field changes near the dipole axis.
- In the tailing part, the curve for $\beta = 3$ follows the shape of the base case with a slightly higher amplitude. The larger matrix diffusion and the longer advection times in the outer stream tubes do not yet influence the shape of the tail, but overcompensate the effect of smaller matrix diffusion in the stream tubes near the dipole axis. (Grimsel experiments for $\beta = 3$ show practically the same tail as for $\beta = 16$ confirming that the shape of the tail is not altered by a reduction of β from ≈ 16 to 3 (cf. Ref. [4], section 4.2.3). For $\beta = 1.5$ the tail is somewhat flatter and has a delayed tail end perturbation due to the enhanced matrix diffusion effects in the outer stream tubes.

The breakthrough curves for the sorbing strontium are represented in Fig. A8.2. They are dominated by matrix diffusion and bulk sorption and show the following main features when decreasing β :

- Shift of peak position in time due to the smaller matrix diffusion in the stream tubes near the dipole axis (cf. Eq. (28b))¹⁵⁹. This shift is substantially larger than for the conservative uranine.
- Increased peak concentration (cf. Eq. (28a)). The increase, due to the smaller dilution by external fracture water is compensated by the $1/Q_i$ proportionality. An additional increasing effect is the reduced matrix diffusion in the stream tubes near the dipole

¹⁵⁷Longer stream tubes as well as lower water velocities than in the base case ($\beta = 16$).

¹⁵⁸The last bump on the tail for $\beta = 1.5$ corresponds to a stream tube representing a tracer mass of only $M_0/84$.

¹⁵⁹ $\tau_0 \sim (L_k/\bar{v}_k)^2$.

axis. It is partially compensated by the individual stream tube breakthrough curves not overlapping as closely as in the base case ($\beta = 16$).

- Decreased drop of the tail due to the substantial delays¹⁶⁰ of the contributions from the outer stream tubes.

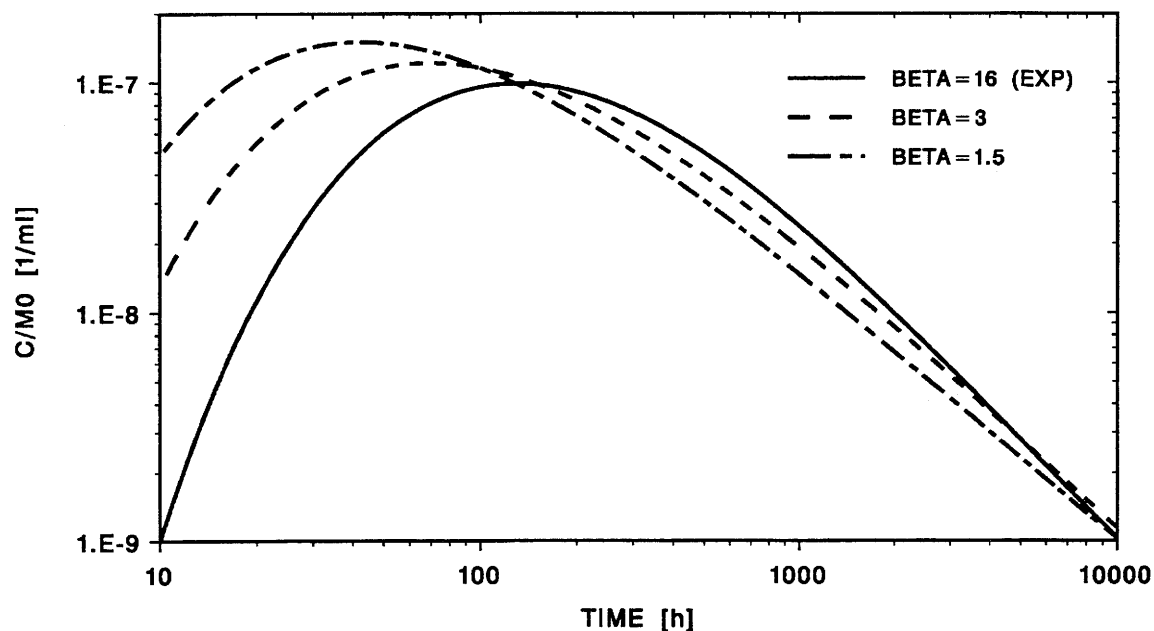


Figure A8.2 Influence of widening the flow field on the breakthrough curve for the sorbing strontium. The peak is dominated by the flow field near the dipole axis leading to a reduced influence of matrix diffusion with decreasing β (generated by an increasing injection rate).

The influence of the flow field on breakthrough curves is strongly dependent on the properties of the migration fracture and of the tracer nuclides. From the results, based on model assumptions and parameters described in chapter 4, the following conclusions can be drawn:

- Flow fields corresponding to $\beta \ll 16$ can complicate investigation of nuclide transport:

¹⁶⁰Delay means in this context a greater τ_0 (cf. Eqs. 27) or a shift on a log scale, similar to Fig. 21 but much larger.

- i) Salient features of breakthrough curves for single stream tubes may get averaged out by very different nuclide transport times in individual stream tubes (e.g. the tail end perturbation).
 - ii) The increased flow field areas with low water velocities are more sensitive to perturbations by the external flow.
 - iii) A substantial increased time is necessary for the numerical calculations.
- A flow field corresponding to $\beta = 1.5$ can produce similar breakthrough tails as matrix diffusion.
 - By restricting the migration experiments for conservative tracers to $\beta \geq 3$, the characteristic shape of the breakthrough tail can be maintained. This enables adequate determination of the porous rock zone parameters.
 - The peak of the breakthrough curves is determined by a relatively narrow area of the flow field near the dipole axis. This is especially true for sorbing nuclides (matrix diffusion and bulk sorption). To avoid large areas of the flow field, contributing only to small changes of the tail, β should not be too small.

9 References

- [1] NEA and SKI, "The International Intraval Project; Phase 1 Test Cases", OECD/NEA, Paris (1992).
- [2] NEA and SKI, "The International Intraval Project; Phase 1 Summary Report", OECD/NEA, Paris (1993).
- [3] U. Frick, W.R. Alexander, B. Baeyens, P. Bossart, M.H. Bradbury, Ch. Buehler, J. Eikenberg, Th. Fierz, W. Heer, E. Hoehn, I.G. McKinley and P.A. Smith, "Grimsel Test Site, The Radionuclide Migration Experiment- Overview of Investigations 1985 - 1990", PSI-Bericht Nr. 120, Würenlingen (1992) and NTB 91-04, Nagra, Wettingen (1992).
- [4] J. Eikenberg, E. Hoehn, T. Fierz and U. Frick, "Grimsel Test Site - Preparation and Performance of Migration Experiments with Radioisotopes of Sodium, Strontium and Iodine", PSI-Bericht Nr. 94-11, Würenlingen (1994) and NTB 94-17, Nagra, Wettingen (1994).
- [5] F. Herzog, "A Simple Transport Model for the Grimsel Migration Experiments", PSI-Bericht Nr. 106, Würenlingen (1991) and NTB 91-31, Nagra, Wettingen (1991).
- [6] A. Jakob, J. Hadermann, F. Roesel, "Radionuclide chain transport with matrix diffusion and non-linear sorption", PSI-Bericht Nr. 54, Würenlingen (1989) and NTB 90-13, Nagra, Baden (1990).
- [7] J. Bear and A. Verruijt, "Modelling Groundwater Flow and Pollution", D. Reidel, Dordrecht (1987).
- [8] G. de Marsily, "Quantitative Hydrology - Groundwaterhydrology for Engineers", Academic Press, San Diego (1986).
- [9] J. Bear and Y. Bachmat, "Introduction to Modeling of Transport Phenomena in Porous Media", Kluwer, Dordrecht (1991).
- [10] P. Bossart and M. Mazurek, "Grimsel Test Site: Structural Geology and Water Flow-Paths in the Migration Shear-Zone", NTB 91-12, Nagra, Wettingen (1991).
- [11] E. Hoehn, Th. Fierz and P. Thorne, "Hydrogeological Characterisation of the Migration Experimental Area at the Grimsel Test Site", PSI-Bericht Nr. 60, Würenlingen (1990) and NTB 89-15, Nagra, Baden (1990).
- [12] F. Herzog, "Hydrologic Modelling of the Migration Site in the Grimsel Rock Laboratory - The Steady State", PSI-Bericht No. 35, Würenlingen (1989) and NTB 89-16, Nagra, Baden (1989).
- [13] S. Vomvoris, "Some results unequal dipole tests", Nagra Internal Note (1988).

- [14] L.W. Gelhar, "Applications of stochastic models to solute transport in fractured rocks", SKB Technical Report 87-05, SKB, Stockholm, Sweden, (1987).
- [15] S. Aksoyoglu, C. Bajo and M. Mantovani, "Batch sorption experiments with iodine, bromine, strontium, sodium and cesium on Grimsel mylonite", PSI-Bericht Nr. 83, Würenlingen (1990) and NTB 91-06, Nagra, Wettingen (1991).
- [16] A. Jakob and J. Hadermann, "INTRAVAL Finnsjön test - modelling results for some tracer experiments", PSI-Bericht Nr. 94-12, Würenlingen (1994) and NTB 94-21, Nagra, Wettingen (1994).
- [17] J. Hadermann, "Radionuklidtransport durch Rissysteme und Matrixdiffusion", internal PSI-Report, TM-45-81-42, Würenlingen (1981).
- [18] M.H. Bradbury, S. Aksoyoglu, W.R. Alexander, B. Baeyens, E. Hoehn, R. Keil, M. Mantovani, J. Meyer, M. Mazurek and C. Bajo, "Laboratory Investigations in Support of the Migration Experiment at the Grimsel Test Site", PSI-Bericht Nr. 28 (1989) and NTB 88-23, Nagra, Baden (1989).
- [19] P. Smith, "Modelling of Laboratory High-Pressure Infiltration Experiments", PSI-Bericht Nr. 116 (1992) and NTB 91-33, Nagra, Wettingen (1992).
- [20] J. Eikenberg, B. Baeyens and M.H. Bradbury, "The Grimsel Migration Experiment: A Hydrogeochemical Equilibrium Test", PSI-Bericht Nr. 100, Würenlingen (1991) and NTB 90-39, Nagra, Wettingen (1991).
- [21] M.H. Bradbury, "Nuclide Rock Interaction Sub-Programme", Annual Report 1993. Internal PSI report AN-44-94-04, Würenlingen (1994).
- [22] W. Heer, J. Hadermann and A. Jakob, "Modelling the radionuclide migration experiments at the Grimsel Test Site", Proc. IAHR Symposium on TRANSPORT AND REACTIVE PROCESSES IN AQUIFERS, Zürich, April 11-15, A.A. Balkema, Rotterdam (1994).
- [23] E. Hoehn, J. Eikenberg, T. Fierz and U. Frick, "Field experiments of radionuclide migration at the Grimsel Test Site (Swiss Alps)", Proc. IAHR Symposium on TRANSPORT AND REACTIVE PROCESSES IN AQUIFERS, Zürich, April 11-15, A.A. Balkema, Rotterdam (1994).
- [24] J. Hadermann and W. Heer, "The Grimsel Migration Experiment: Integrating Field Experiments, Laboratory Investigations and Modelling", to be published in J. Cont. Hydr. (1995).
- [25] J. Bear, "Dynamics of Fluids in Porous Media", Dover, New York (1988).
- [26] J. Atchison and J.A.C. Brown, "The Lognormal Distribution", Cambridge Univ. Press (1957).

- [27] U. Frick, "Beurteilung der Diffusion im Grundwasser von Kristallingesteinen" Nagra, internal report NIB, Wettingen (1993).
- [28] L. Moreno, Y.W. Tsang, C.F. Tsang, F.V. Hale, and I. Neretnieks, "Flow and Tracer Transport in a Single Fracture: A Stochastic Model and its Relation to Some Field Observations", *Water Resources Research* **24** (1988) 2033.
- [29] Y.W. Tsang, C.F. Tsang, I. Neretnieks and L. Moreno, "Flow and Tracer Transport in Fractured Media: A Variable Aperture Channel Model and its Properties", *Water Resources Research* **24** (1988) 2049.